

5-2012

Design of Meta-Materials Outside the Homogenization Limit Using Multiscale Analysis and Topology Optimization

Christopher Czech

Clemson University, christopher.d.czech@gmail.com

Follow this and additional works at: https://tigerprints.clemson.edu/all_dissertations



Part of the [Mechanical Engineering Commons](#)

Recommended Citation

Czech, Christopher, "Design of Meta-Materials Outside the Homogenization Limit Using Multiscale Analysis and Topology Optimization" (2012). *All Dissertations*. 900.

https://tigerprints.clemson.edu/all_dissertations/900

This Dissertation is brought to you for free and open access by the Dissertations at TigerPrints. It has been accepted for inclusion in All Dissertations by an authorized administrator of TigerPrints. For more information, please contact kokeefe@clemson.edu.

DESIGN OF META-MATERIALS OUTSIDE THE HOMOGENIZATION
LIMIT USING MULTISCALE ANALYSIS AND TOPOLOGY
OPTIMIZATION

A Dissertation
Presented to
the Graduate School of
Clemson University

In Partial Fulfillment
of the Requirements for the Degree
Doctor of Philosophy
Mechanical Engineering

by
Christopher Czech
May 2012

Accepted by:
Dr. Georges Fadel, Committee Chair
Dr. Paolo Guarneri
Dr. Lonny Thompson
Dr. Gang Li
Dr. Margaret Wiecek
Dr. James Gibert

Abstract

The field of meta-materials engineering has largely expanded mechanical design possibilities over the last two decades; some notable design advances include the systematic engineering of negative Poisson's ratio materials and functionally graded materials, materials designed for optimal electronic and thermo-mechanical performances, and the design of materials under uncertainty. With these innovations, the systematic engineering of materials for design-specific uses is becoming more common in industrial and military uses. The motivation for this body of research is the design of the shear beam for a non-pneumatic wheel. Previously, a design optimization of a finite element model of the non-pneumatic wheel was completed, where a linear elastic material was simulated in the shear beam to reduce hysteretic energy losses. As part of the optimization, a set of optimal orthotropic material properties and other geometric properties were identified for the shear beam. Given that no such natural linear elastic material exists, a meta-material can be engineered that meets these properties using the aforementioned tools. However, manufacturing constraints prevent the use of standard homogenization analysis and optimization tools in the engineering of the shear beam due to limitations in the accuracy of the homogenization process for thin materials.

In this research, the more general volume averaging analysis is shown to be an accurate tool for meta-material analysis for engineering thin-layered materials. Given an accurate analysis method, several optimization formulations are proposed, and optimality conditions are derived to determine the most mathematically feasible and numerically reliable formulation for topology optimization of a material design problem using a continuous

material interpolation over the design domain. This formulation is implemented to engineer meta-materials for problems using the volume averaging analysis, which includes the use of variable linking and the derivation of first-order design sensitivities to increase computational efficiency. Inspired by honeycomb materials, a new method of discretizing the material design domain into unit cells with non-simple connectivity is proposed as a way of increasing the solution space of the topology optimization problem. Finally, these methods are used in the meta-material design process to identify several candidate meta-material geometries from a polycarbonate base material for the shear layer of the non-pneumatic wheel; notable geometries include an ‘x’-like geometry, a bent column-like geometry identified previously as a bristle, and, remarkably, an auxetic honeycomb geometry. This is the first reported result demonstrating the auxetic honeycomb geometry to be a minimum weight structure in shear loading where a general topology optimization method was used.

Dedication

To my family and friends. Without your support, this would not have been possible.

Acknowledgments

I would like to thank my family for their unconditional love and support from the beginning of my journey. I would like to thank my parents, Jane and Dave, for providing me with the drive and support to continue working for the many achievements and experiences I desire from life. I would like to thank my siblings, Nick and Natalie, for inspiring me every day to be a better person and to share my experiences with others. Despite our differences, I miss our daily conversations and social engagements.

I would like to thank the members of my committee for lending their knowledge and support throughout the research process. Special thanks to my advisor, Dr. Georges Fadel, for his support and guidance and for offering me the opportunity to approach the research in an interdisciplinary manner. Special thanks to Dr. James Gibert and Dr. Paolo Guarneri for acting as co-advisors and collaborators at different stages in my research; their care and attention to detail have tremendously improved my work. Thanks to Dr. Margaret Wiecek for her expertise in optimization theory and for the pleasure of collaborating with such a strong and honest researcher. Thanks to Dr. Lonny Thompson and Dr. Gang Li for their input and critical thinking.

Finally, I would like to thank my friends for providing companionship and laughter. Special thanks to my friends Ben Carter and Michelle Greene for their daily conversation and support; without them, I would have never been able to accomplish this undertaking. Thanks to the members of the Clemson University Rowing Association, both new and old, for being my family away from home. I have and will continue to appreciate and cherish the friendships we have made. And thanks to the many other friends I have made through

my years here at Clemson. I am truly blessed for having the opportunity to know them, and their genuine interest and support have been an integral part of my professional and personal development.

Table of Contents

Title Page	i
Abstract	ii
Dedication	iv
Acknowledgments	v
List of Tables	ix
List of Figures	x
1 Introduction	1
1.1 Overview of Meta-Materials Design by Topology Optimization	1
1.2 Motivation	4
1.3 Hypotheses and Research Questions	10
1.4 Dissertation Outline	16
2 Literature Review	18
2.1 Meta-Materials Analysis	18
2.2 Topology Optimization	28
3 Analytical Issues in Meta-Materials Analysis	44
3.1 Comparison of Homogenization and Volume Averaging	45
3.2 Design Examples	58
3.3 Summary	62
4 Optimality Conditions For Meta-Materials Topology Design Problems 65	
4.1 Considered Optimization Problems	67
4.2 Optimality Conditions	68
4.3 Design Examples Using Homogenization	83
4.4 Discussion	88
4.5 Summary	91
5 Topology Optimization Using Volume Averaging	92
5.1 Optimization Methods	93
5.2 Optimization Parameters and Results	102

5.3	Summary	110
6	Non-Simple Connectivity In Meta-Materials Analysis and Optimization	111
6.1	Mathematical Framework for Analysis	112
6.2	Comparison of Homogenization and Volume Averaging for Non-Simply Connected Structures	117
6.3	Comparison of Meta-Material Properties to Analytical Formulae	120
6.4	Topology Optimization of Non-Simply Connected Structures	125
6.5	Summary	129
7	Meta-Material Design of the Shear Beam of a Non-Pneumatic Wheel	130
7.1	Design Study Parametrization	130
7.2	Topology Optimization of the Shear Layer	133
7.3	Discussion	150
7.4	Summary	152
8	Concluding Remarks	154
8.1	Contributions	157
8.2	Discussion	157
8.3	Future Work	158
Appendices		161
A	Comparison of Homogenization and Volume Averaging Analysis Methods	162
B	Single Layer Optimization Results	168
C	Non-Simple Connectivity Analysis Comparisons	178
D	Non-Simple Connectivity Optimization Results	186
Bibliography		195

List of Tables

2.1	Displacement boundary conditions for volume averaging analysis	29
2.2	Traction boundary conditions for volume averaging analysis	29
4.1	Numerical Results For Optimizations Targeting E_{22}^*	85
4.2	Numerical Results For Optimizations Targeting E_{22}^*	86
4.3	Summary of Mathematical Analysis of Optimality Conditions	89
5.1	Numerical Results For Optimization Using Different Initial Design Points .	104
5.2	Numerical Results For Optimization of a Single Layer Material	108
6.1	Parameters used for the analytical comparison of honeycombs	124
6.2	Numerical Results For Optimization of a Non-Simply Periodic Structure Using Homogenization	126
6.3	Numerical Results For Optimization of a 12x2 Non-Simply Periodic Structure Using Volume Averaging	126
7.1	Design variables and bounds used in the non-pneumatic wheel optimization	133
7.2	Low-resolution optimization results	136
7.3	Selected visual results for optimizations using 30x30 unit cell discretizations	137

List of Figures

1.1	Commercial software example of minimum compliance topology optimization	2
1.2	Example of topology optimization for compliance	2
1.3	System optimization to meta-material optimization loop	3
1.4	Components of the non-pneumatic wheel	5
1.5	Non-pneumatic wheel and shear beam under deflecting load	6
1.6	Hysteretic loss in elastic and elastomeric materials	6
1.7	Ashby selection chart: loss coefficient versus Young’s modulus	7
1.8	Shear beam model with a bristle geometry	8
1.9	Non-pneumatic wheel parameters and design variables for global analysis and optimization	9
1.10	Set of optimal designs resulting from optimization of non-pneumatic wheel .	10
1.11	Example of a meta-material that violates the homogenization limits	11
1.12	Non-square unit cell	12
1.13	Simply-connected and non-simply connected topologies	13
1.14	Non-simply connected and simply connected lattices that produce honeycomb designs	13
1.15	Optimal topologies to the tension and shear optimization problems	14
2.1	Examples of a square, simply-connected periodicity	20
2.2	Global to local coordinates of the meta-material design process	20
2.3	Monohedral, periodic tilings of a planar space	21
2.4	Fundamental domains of a lattice for a periodic, monohedral tiling	22
2.5	Homogenization analysis examples	25
2.6	Unit cell parameters for the volume averaging analysis	30
2.7	Unit cell under homogeneous displacement tension and shear boundary conditions	30
2.8	Unit cell under homogeneous traction tension and shear boundary conditions	31
2.9	Examples of two analytical volumes for the volume averaging analysis . . .	31
2.10	Ratios of homogenized to averaged moduli versus number of cells	32
2.11	Schematic of the asymptotic homogenization process	36
2.12	Element density versus normalized SIMP-interpolated Young’s modulus . .	38
2.13	Ground structure topology design problem	39
2.14	Checkerboard pattern solution to a topology optimization problem	40
2.15	One-node connected hinge solution to a topology optimization problem . .	40
3.1	Three modes of deformation used in volume averaging and homogenization.	47

3.2	$N \times N$ analysis domain examples	47
3.3	$N \times N$ analysis for meta-material Young's moduli of 'x' geometry	48
3.4	$N \times N$ analysis for meta-material shear moduli of 'x' geometry	48
3.5	$N \times N$ analysis for meta-material Young's moduli of '+' geometry	49
3.6	$N \times N$ analysis for meta-material shear moduli of '+' geometry	49
3.7	Finite Element Convergence Analysis of 'x' geometry	50
3.8	Finite Element Convergence Analysis of '+' geometry	50
3.9	Similar unit cell geometries with different W/L scaling ratios	51
3.10	Meta-material properties as a function of W/L for Single Cell Thin 'x' Geometry	52
3.11	Meta-material properties as a function of W/L for Single Cell Thick 'x' Ge- ometry	52
3.12	Meta-material properties as a function of W/L for Single Cell Thin 'x' Geometry	53
3.13	Meta-material properties as a function of W/L for Single Cell Thick 'x' Ge- ometry	53
3.14	Single-layer materials with different W/L scaling ratios	55
3.15	Single layer meta-material properties for 'x' geometry with W/L equal to one	56
3.16	Single layer meta-material properties for 'x' geometry with W/L equal to five	56
3.17	Single layer meta-material properties for '+' geometry with W/L equal to one	57
3.18	Single layer meta-material properties for '+' geometry with W/L equal to five	57
3.19	Loading conditions for the simple shear test design problem	58
3.20	Depiction of the accuracy analysis of the meta-material design process . . .	59
3.21	Relative errors of material displacements for square materials consisting of $N \times N$ unit cells 'x' geometry	60
3.22	Relative errors of material displacements for square materials consisting of $N \times N$ unit cells '+' geometry	60
3.23	Relative errors of single-layer material displacements for 'x' geometry with W/L equal to one	61
3.24	Relative errors of single-layer material displacements for 'x' geometry with W/L equal to five	61
3.25	Relative errors of single-layer material displacements for '+' geometry with W/L equal to one	62
3.26	Relative errors of single-layer material displacements for '+' geometry with W/L equal to five	62
4.1	Initial point used for optimization	83
4.2	Visual results for optimizations targeting different Young's moduli E_{22}^* . . .	84
4.3	Visual results for optimizations targeting different Young's moduli G_{23}^* . . .	87
5.1	Depiction of periodicity and variable linking for optimization	96
5.2	Depiction of periodicity and variable linking for optimization	100
5.3	Initial points used for topology optimization	103
5.4	Initial point study results with target modulus $E_{22} = 3$ GPa	105
5.5	Initial point study results with target modulus $E_{22} = 15$ GPa	105
5.6	Initial point study results with target modulus $E_{33} = 3$ GPa	105
5.7	Initial point study results with target modulus $E_{33} = 15$ GPa	105

5.8	Initial point study results with target modulus $G_{23} = 2$ GPa	106
5.9	Initial point study results with target modulus $G_{23} = 6$ GPa	106
5.10	Single Layer Optimization Targeting E_{22} moduli	109
5.11	Single Layer Optimization Targeting E_{33} moduli	109
5.12	Single Layer Optimization Targeting G_{23} moduli	109
6.1	Honeycomb structure with simple connectivity	112
6.2	Honeycomb structure with non-simple connectivity	112
6.3	Simply-connected and non-simply connected topologies	114
6.4	Enforcement of periodic boundary conditions for homogenization when analyzing using non-simply connected structures. (The coordinates z_i indicate the analysis domain is the UC only.)	115
6.5	Three modes of deformation used in volume averaging.	115
6.6	Example analysis domain of a two-layer material analyzed using the volume averaging method.	116
6.7	NxN analysis for meta-material moduli of thin honeycomb geometry	118
6.8	NxN analysis for meta-material moduli of thick honeycomb geometry	118
6.9	12xN layer analysis for meta-material moduli of thin honeycomb geometry .	119
6.10	12xN layer analysis for meta-material moduli of thick honeycomb geometry	119
6.11	Relative errors of material displacements consisting of NxN unit cells with thin honeycomb geometry	120
6.12	Relative errors of material displacements consisting of NxN unit cells with thick honeycomb geometry	120
6.13	Relative errors of material displacements consisting of 12xN layers of unit cells with thin honeycomb geometry	121
6.14	Relative errors of material displacements consisting of 12xN layers of unit cells with thick honeycomb geometry	121
6.15	Parameters for analytical equations meta-material moduli of honeycombs .	122
6.16	Plot of analytical and numerical E_{22}^M moduli as a function of member thickness in honeycombs	123
6.17	Plot of analytical and numerical E_{33}^M moduli as a function of member thickness in honeycombs	123
6.18	Plot of analytical and numerical G_{23}^M moduli as a function of member thickness in honeycombs	123
6.19	Homogenization Optimization with Non-simple Connectivity	127
6.20	Volume Averaging of a 12x2 Structure Optimization with Non-simple Periodicity	128
7.1	Depiction of non-pneumatic wheel optimization variables	131
7.2	Two-level optimization process used for meta-material design of the shear beam of the non-pneumatic wheel.	132
7.3	Set of optimal solutions potentially targeted for the design of the meta-material shear layer.	133
7.4	Meta-material tie requirements for the non-pneumatic wheel design. The tie exists only if the displacements z_m and z_h are equal.	134

7.5	Initial points used for the high-resolution design of the meta-material shear layer.	138
7.6	Simply connected meta-materials generated from initial point A.	139
7.7	Simply connected meta-materials generated from initial point B.	140
7.8	Simply connected meta-materials generated from initial point C.	141
7.9	Simply connected meta-materials generated from initial point D.	142
7.10	Feasible design results from high-resolution optimization study	144
7.11	Non-simply connected meta-materials generated from initial point A.	145
7.12	Non-simply connected meta-materials generated from initial point B.	146
7.13	Non-simply connected meta-materials generated from initial point C.	147
7.14	Non-simply connected meta-materials generated from initial point D.	148
7.15	Unit cell of an auxetic honeycomb structure generated from topology optimization using volume averaging	149
7.16	Feasible design results from high-resolution optimization study using non-simple connectivity	150

Chapter 1

Introduction

1.1 Overview of Meta-Materials Design by Topology Optimization

Topology optimization, a field of structural optimization, has become a useful tool in recent years with the increase in usage of optimization in design. Topology optimization is concerned with the optimal distribution of material in an object that will be subjected to an external excitation (mechanical, electric, magnetic, etc.) to have a desired response.

Topology optimization in the mechanical field is commonly divided into several sub-fields, including, but not limited to minimum compliance (stiffness design) topology optimization, compliant (flexibility design) topology optimization, and design of meta-materials (targeting desired design properties). Figure 1.1 depicts the minimum compliance design of a control arm subjected to several independent loads [1]. A finite element solver is used as to analyze the stresses and strains on the control arm, which iterates with the topology optimization program to determine the optimal distribution of material for the final design.

Figure 1.2 depicts a two-dimensional model of a half of a compliant gripper designed using compliant topology optimization [2]. Here the structure is purposely built to deform in a flexible manner to meet some target displacement given a set of specified input loads and boundary conditions.

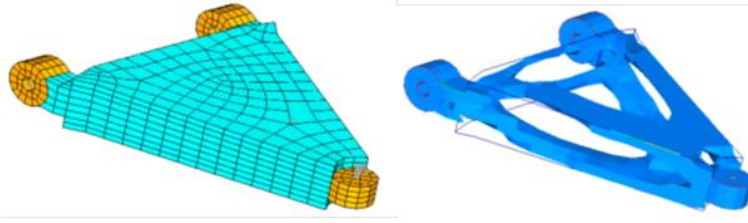


Figure 1.1: A control arm (right) developed using Altair Optistruct from the input finite element design (left). [1]

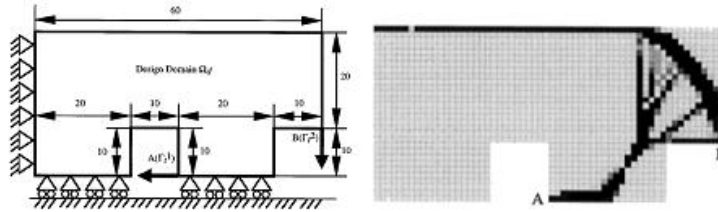


Figure 1.2: The optimal distribution of material for half of a compliant gripper designed using compliant topology optimization (right), given the design domain subject to loading and boundary conditions (left). [2]

The subfield of meta-material optimization is concerned with local optimization of a material to have mechanical (or other properties) required by a global design. Typically, the global material is part of a larger assembly, and this larger assembly has one or more design goals (i.e., maximum displacement, constraints on a traction profile, minimum energy loss) to be achieved. The global design is optimized with a homogeneous material in place of the meta-material, and the material properties are treated as optimization design variables of the global optimization. These optimal properties are then passed to a meta-material optimization method that will determine the optimal material distribution to achieve the desired material properties via topology optimization. This process is depicted in Figure 1.3. Meta-material topology optimization has been the most actively researched of the aforementioned subfields in recent years, as the design methodology has been used in the design of lightweight composites and periodic structures. The analytical workhorse of meta-material optimization, asymptotic (or inverse) homogenization, is built from a mathematical theory that requires global scaling and local sizing constraints be met. In particular, the unit cell (UC), which is the fundamental building block of a periodic material, must be much smaller

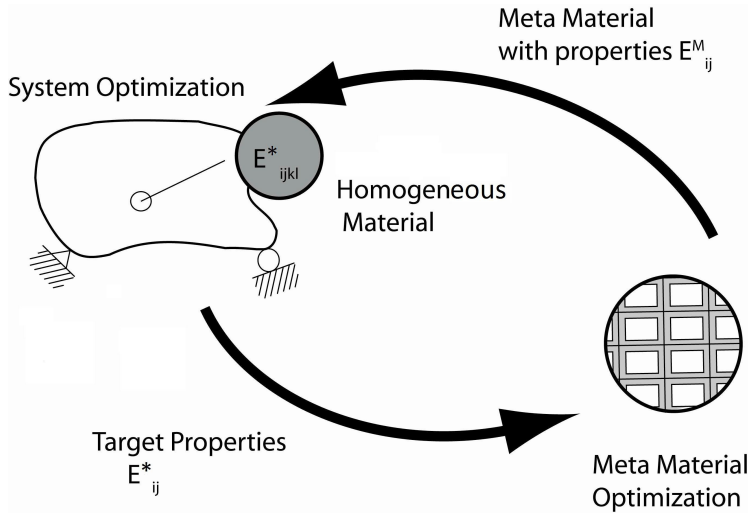


Figure 1.3: System optimization to meta-material optimization loop. [3]

than the scaling lengths of the material comprised of the UC structure. Currently, this assumption inherently limits meta-material optimization methods to those design problems that meet the assumptions of homogenization theory, while there is a knowledge gap for those meta-material problems that do not meet the limiting criteria.

This research focuses on extending the meta-material topology algorithm to materials that do not meet the constraining assumptions of asymptotic homogenization. In particular, the design of meta-materials for use in layered composites serves as good example. By also stretching and shrinking the aspect ratios of the periodic cells constituting the meta-material composites, basic homogenization assumptions are violated [4], [5]. However, a less traditional, but theoretically simpler, analytical method based on averaging properties of heterogeneous materials places no constraining assumptions on the meta-material design. This methodology has the disadvantage of being much more computationally expensive than homogenization, but it has been shown to be accurate in cases in which homogenization is inaccurate. By comparing asymptotic homogenization results to this averaging analysis, the fidelity of asymptotic homogenization outside of its assumptions can be directly evaluated.

In validating any multi-level optimization method, the consistency of the global and local must also be evaluated: the performance of the global design, not the stand-alone

meta-material, is the chief concern of the design engineer [6]. Given this, the homogenization and averaging analyses can be evaluated to see which methods lead to meta-materials that perform as expected when placed in global assemblies. The demonstrated achievement or failure to achieve global design goals of these meta-material analyses are viewed as the primary evidence substantiating or disproving the validity of a particular method for specific design uses.

Given analytical methods with fidelity both inside and outside of asymptotic homogenization limits, several other important questions about analysis and optimization can be asked. Questions about the periodicity and connectivity of the individual cells constituting the meta-material lattice arise from considering different regular structures that appear in nature. For example, it is not obvious that structures with different connectivity can be analyzed using the same analytical methods. Also, a careful review of the literature indicates a difficulty in obtaining multiple meta-material properties via multi-criteria topology optimization methods; however, it is not unexpected to have a meta-material design problem highly sensitive to more than one meta-material property.

1.2 Motivation

The original wheel for the passenger car was invented at a time when rough roads and road obstacles were a norm. This meant a wheel had to be able to roll over larger obstacles (e.g., large stones) while providing adequate comfort for passengers. However, now that smoother roads are a norm, energy losses due to the resistance in rolling (collective cyclic losses of a loaded wheel) have become a more important design consideration. The motivating case for this body of research, the non-pneumatic wheel has two major advantages over its pneumatic counterparts: the elimination of tire inflation issues in daily operation equates to less energy loss due to under-inflation of the wheel, and eliminating the pneumatic aspect allows decoupling of key performance characteristics, possibly increasing the available design space for the wheel [7].

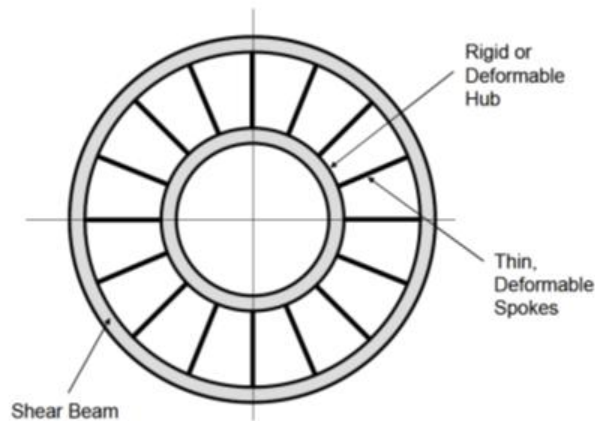


Figure 1.4: The major components of the non-pneumatic wheel. A rigid hub has been chosen since the publication of the preliminary design depicted here. The geometric design of the shear beam is the primary motivation for this research. [7]

1.2.1 The Non-Pneumatic Wheel Concept

The non-pneumatic wheel (Figure 1.4) presents a difficult optimization problem: design a shear beam that is capable of transmitting torque from inner radius to outer radius that will deform under cyclic loading to minimize total energy loss while maintaining an acceptable pressure distribution at the contact patch between the ground surface and the wheel. When an elastomeric material is used in the shear beam, approximately 50% of the energy input into driving the non-pneumatic wheel is lost internally as the shear beam deforms while passing through the contact patch (Figure 1.5). This energy loss is primarily a result of the hysteretic loss of the elastomer in cyclic loading [8], [9]. One way to reduce this rolling resistance is to use a linear elastic material in the shear beam in place of the elastomer. The theoretical hysteric energy losses in the shear beam, depicted in Figure 1.6, are reduced to zero by using the elastic material over the elastomeric material [9].

While it is clear that using a linear elastic material in the shear beam would reduce the rolling resistance of the non-pneumatic wheel, what is not clear is whether the performance characteristics of the viscoelastic shear beam can be met using a linear elastic material. The Ashby material selection chart (Figure 1.7) gives a more realistic depiction of material choices that can be made to meet the design needs [10]. The loss coefficient η

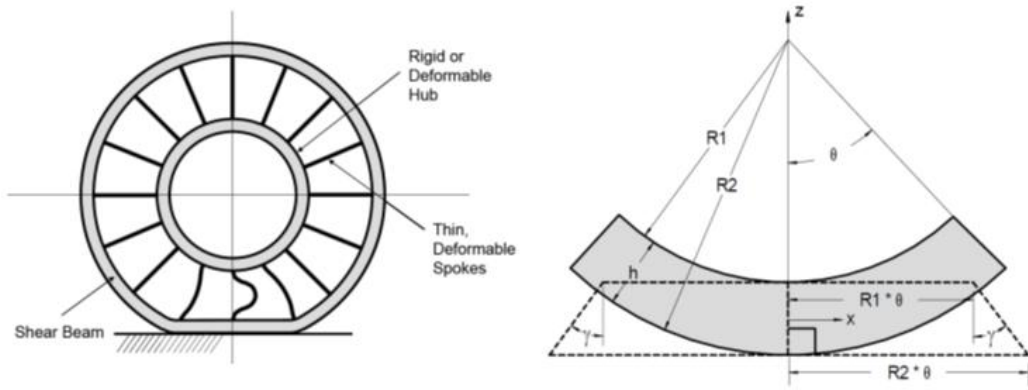


Figure 1.5: (Left) Non-pneumatic wheel model in deflection. (Right) Portion of continuous shear beam at contact patch. The solid gray portion is the beam under no loading, while the dashed lines show the contact portion under deflection. [7]

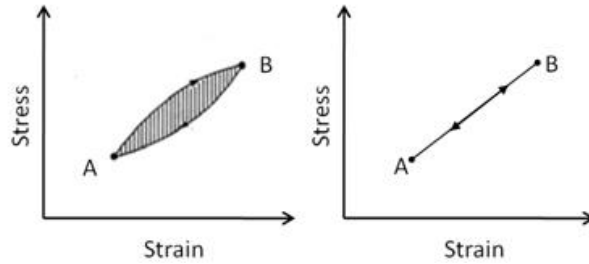


Figure 1.6: (Left) Theoretical, hysteretic stress-strain curve of an elastomeric material. The energy loss is the area between the two lines. (Right) Theoretical, hysteretic stress-strain curve of a linear elastic material. There is no theoretical energy loss. [11]

is plotted against the Young's modulus E for different classes of materials. An elastomeric material such as the one used initially in the shear beam has a very low Young's modulus but also a high loss coefficient. A linear elastic material (such as metals and some polymers) has a loss coefficient one to two orders of magnitude lower than elastomers.

However, the Young's moduli for these materials are two to three orders of magnitude too large to meet the elastomer values. Given that the polymer and metal properties shown in this chart are for homogeneous materials, it is reasonable to expect that, by designing a non-homogeneous meta-material out of a metal or polymer using topology optimization, the Young's moduli and shear modulus of the meta-material can be reduced the several orders of magnitude necessary to meet design needs without a large compromise in loss coefficient.

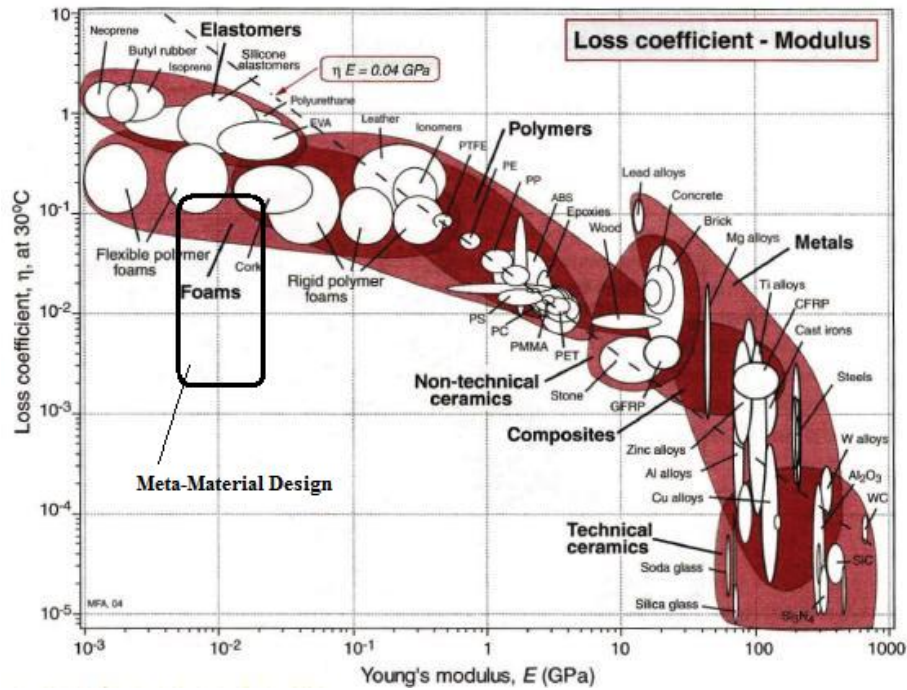


Figure 1.7: Ashby material selection chart depicting loss coefficient versus Young's modulus. [10] The meta-material design goal for the non-pneumatic wheel is the area shown within the box.

One example of a non-homogeneous shear beam termed the bristle geometry is shown in (Figure 1.8). Lowe et al. [12] show that a shear beam containing material continuously throughout exhibits a greater energy loss than a shear beam with bristle geometry. While this design is not necessarily the optimal design, the authors show the benefit in reduction of energy loss in the beam for non-continuous material geometries.

1.2.2 Global Optimization Model and Results

Thyagaraja [11] and Thyagaraja et al. [13] present the two-dimensional, global finite element analysis (FEA) and optimization model for the non-pneumatic wheel (Figure 1.9). The non-pneumatic wheel undergoes a static, linear deflection in which the central hub is displaced by a specified distance. In the shear beam, a homogenous, linear, orthotropic material is modeled as a substitute for the meta-material shear beam. The global model is optimized by minimizing the difference between a targeted shear strain of the shear beam

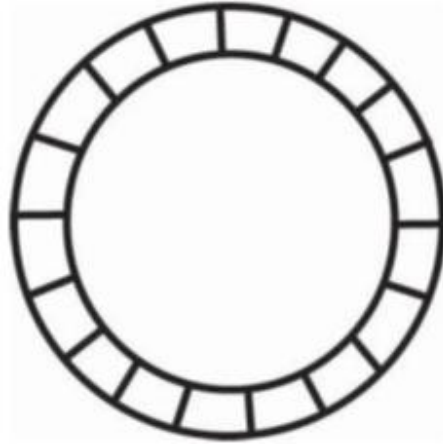


Figure 1.8: Shear beam model with a bristle geometry. [12]

and the maximum shear strain subject to contact pressure and material constraints. This is done because the goal is to replace the elastomeric shear beam, which has a high loss coefficient but also large shear strain before yield, with a polymer or metallic shear beam of equivalent maximum shear strain and much lower loss coefficient. The contact pressure and material constraints are included to account for ride comfort, road noise and road wear requirements.

Design variables of the optimization include the material parameters of the orthotropic shear beam material, material properties of inner and outer inextensible membranes, the in-plane thickness of the shear beam $slThk$ and the thicknesses of the inner and outer inextensible membranes $iiemThk$ and $oiemThk$, as indicated in Figure 1.9.

The in-plane, orthotropic material properties (which can be found in composites materials texts [14], [15]) of the homogenous shear beam follow the constitutive relation

$$\begin{pmatrix} \sigma_{22} \\ \sigma_{33} \\ \sigma_{23} \end{pmatrix} = \begin{bmatrix} Q_{22} & Q_{23} & 0 \\ Q_{23} & Q_{33} & 0 \\ 0 & 0 & Q_{66} \end{bmatrix} \begin{pmatrix} \varepsilon_{22} \\ \varepsilon_{33} \\ \varepsilon_{23} \end{pmatrix} \quad (1.1)$$

where σ_{ij} represent the tensile and shear stresses, respectively, ε_{ij} represents the tensile and shear strains, and Q_{ij} are the components of the linear constitutive tensor. (Tensor

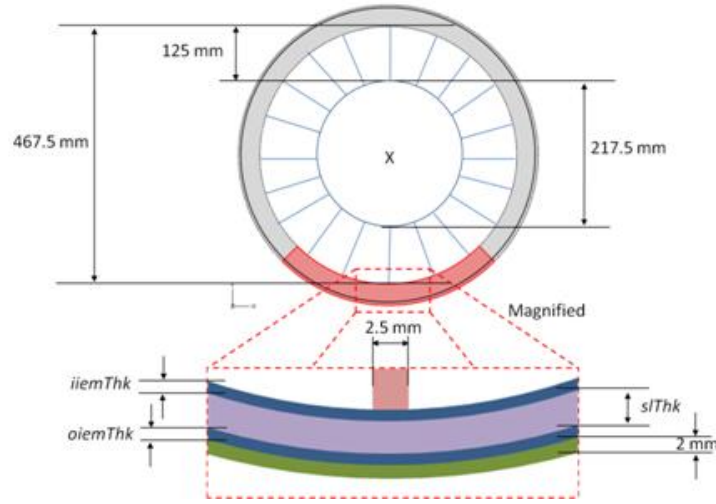


Figure 1.9: Non-pneumatic wheel parameters and design variables for global analysis and optimization. [11]

symmetries have been assumed in the Eq. 1.1.) The components Q_{ij} have the form

$$Q_{22} = \frac{E_{22}}{1 - \nu_{23}\nu_{32}} \quad (1.2)$$

$$Q_{33} = \frac{E_{33}}{1 - \nu_{23}\nu_{32}} \quad (1.3)$$

$$Q_{23} = \frac{\nu_{32}E_{22}}{1 - \nu_{23}\nu_{32}} = \frac{\nu_{23}E_{33}}{1 - \nu_{23}\nu_{32}} \quad (1.4)$$

$$Q_{66} = G_{23} \quad (1.5)$$

Only the in-plane Young's moduli E_{22} and E_{33} shear modulus G_{23} and Poisson's ratios ν_{23} and ν_{32} are considered in the two-dimensional optimization model.

Results from the optimization of the non-pneumatic wheel are shown in Figure 1.10 [11]. The results indicate that there are an infinite number of optimal solutions. A curve was fit to the optimal solutions to show how the shear beam thickness and the shear modulus of the shear beam can be changed. Given the set of optimal designs along with the additional

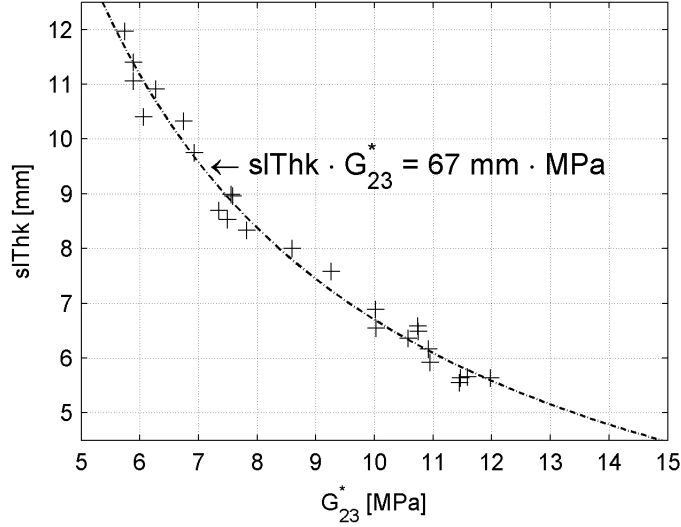


Figure 1.10: Set of optimal designs resulting from optimization of non-pneumatic wheel. [11]

information that the non-pneumatic wheel model is most sensitive to changes in the shear modulus of the shear layer (for more detail, see [11]), a meta-material design can be targeted by selecting a shear beam thickness and targeting the corresponding shear modulus using one of the meta-material topology design processes described in the previous section (Figure 1.3).

1.3 Hypotheses and Research Questions

The current body of literature demonstrates the utility of the asymptotic homogenization analysis and subsequent optimization in the design of meta-materials. However, relatively little work has been done on understanding the modeling and convergence properties for meta-materials that do not satisfy either the homogenization scaling or representative volume element (RVE) limits. (A representative volume for a material is defined as an amount of volume required for the properties analysis to accurately represent the properties of the entire material. The limit in which enough material is analyzed to obtain a representative volume is called the RVE limit. For periodic materials, this limit may



Figure 1.11: Example of a meta-material that violates the homogenization limit in the vertical direction (and likely the horizontal direction).

be reached by one or a collection of UCs.) These meta-materials remain candidates for meta-material design. For example, it is possible a set of meta-material properties may be achievable in the homogenization scaling limit in theory, but the scale of the UC will not be physically manufacturable. For thin layers of material, as is the case of the shear beam in the non-pneumatic wheel, it may still be possible to obtain the desired material properties with one or a few layers of UCs and have a much easier-to-manufacture UC geometry. These materials clearly violate the homogenization scaling limit in one dimension, and whether or not they reach the RVE limit is unknown.

An example of a meta-material domain in which the homogenization limit is not met is shown in Figure 1.11. In this material, the scaling in the vertical direction and the height of the UC clearly violate the small parameter expansion of homogenization theory. In the horizontal direction, at six UCs long, the meta-material may or may not achieve the RVE and homogenization limits. However, even if there is an infinite number of cells in the horizontal direction, the homogenized parameters involving the vertical dimension, namely E_{33}^H and G_{23}^H , should not necessarily be expected to be numerically accurate.

It is also possible that the material design targets for the meta-material optimization fall outside the range of feasibility for known materials in square UC domains. The single, small-parameter expansion of homogenization is also violated in this case, so extending meta-material analytical methods to non-square, rectangular UCs opens up the range of design possibilities. However, it is unclear the effect this has on the accuracy of homogenized parameters. Figure 1.12 depicts a simple parametrization of a non-square UC.

To date, no literature has been found that investigates the idea of non-simple connectivity of UCs (see Figure 1.13). The general notion of topology of an object is rooted

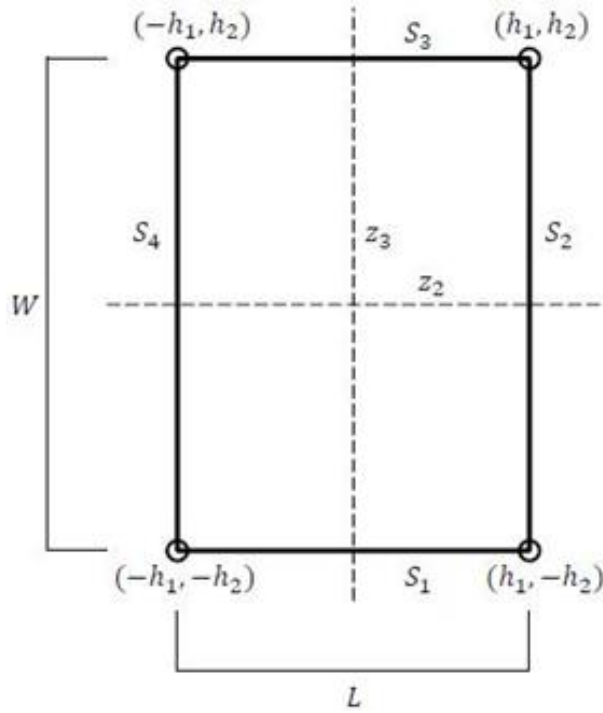


Figure 1.12: Non-square unit cell. The unit cell depicted violates the single small-parameter expansion of homogenization theory.

in domain connectivity. Topology optimization does, by definition, change the topological geometry of a material structure by introducing holes in the material in a way that benefits the design goal. Thus, it is suggestive that the topological connectivity of the design domain may directly affect the final design topology.

The primary benefit in investigating different topological connectivity is that it opens up the same capabilities to design a broader class of meta-materials without necessarily complicating the analytical methods used. For example, see the works in Diaz and Bénard [16] and more clearly in Lipperman et al. [17] in which honeycomb meta-materials were designed by changing angles of unit cells (Figure 1.14). The square cells have the benefit of having much simpler analysis and optimization without the added complication of more parameters, and they are already well-investigated in meta-material analysis methods. The square-cell method is also the only one reported across both ground structure and continuum material interpolation schemes. Honeycomb structures, whose UCs can be

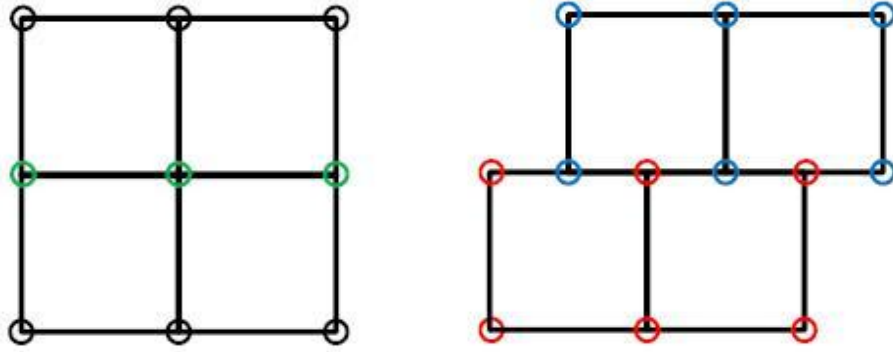


Figure 1.13: (Left) Simply-connected topology. Corners nodes are jointly shared a single adjoining edge. (Right) A topology in which the unit cells are not simply connected. The bottom layer joins to the top layer in a way in which each edge contacts two others.

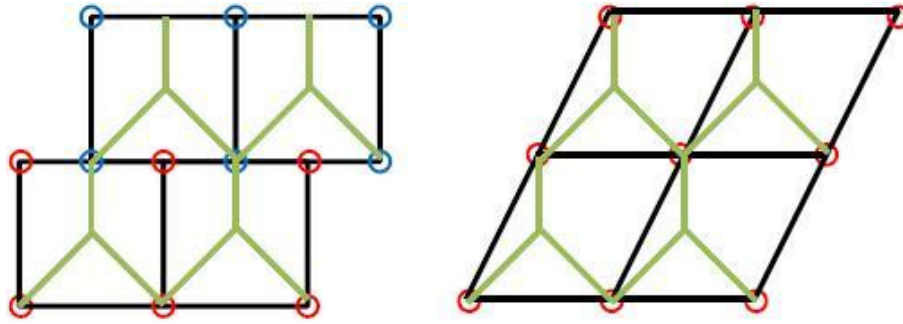


Figure 1.14: (Left) Non-simply connected, square UC lattice (black lines) that leads to the honeycomb meta-material design (green). (Right) Simply-connected, parallelogram UC lattice that leads to the same honeycomb meta-material design.

given only by parallelogram or non-simply connected lattices, have been investigated as candidates for meta-material geometries in the non-pneumatic wheel [18]. Using this non-simple connectivity in the meta-materials design process could also open up the topological possibilities of optimal solutions.

In the discussion of meta-material topology optimization on the UC, upon closely reviewing the literature, single criteria optimization methods (i.e., those targeting a single meta-material property value), are widely reported. The two geometries, or their superpositions, shown in Figure 1.15 were reported by Zhang et al. [19] to be optimal topological designs when extremizing Young's moduli or shear moduli. The '+' design in Figure 1.15 is optimal when designing on one of the two Young's moduli E_{22}^* or E_{33}^* , as this geometry

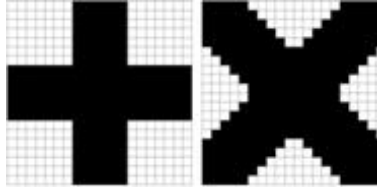


Figure 1.15: Optimal topologies, or theirs superpositions, when optimizing on Young's moduli (left) or shear modulus (right), as reported in Zhang et al. [19]

minimizes the shear stresses in the internal beams, leaving primarily compressive stresses. Similarly, when designing only on the shear modulus G_{23}^* , the 'x' design is optimal. Internal studies on topology optimization of meta-materials using asymptotic homogenization and composites analysis methods confirm these findings.

1.3.1 Primary Hypotheses

The primary hypothesis is that the asymptotic homogenization process, while accurate when the limiting theoretical assumptions are met, is not accurate for meta-material design below some scaling limit of the global meta-material. Asymptotic homogenization is derived from a single, small-parameter expansion that assumes the length-scale of the UC that makes up the meta-material is much smaller than the length scale of the meta-material itself. When this relative length scaling is not achieved, asymptotic homogenization may not produce accurate meta-material moduli. In the meta-material design process, this may lead to an inconsistent link between global and local meta-material properties, resulting in a design that does not perform as intended in the global system.

The asymptotic homogenization process is not accurate for meta-material design when poorly-scaled unit cells are utilized. Because only a single parameter is used in the asymptotic expansion, very long or very wide UCs may also create inaccuracies in the homogenization analysis and the subsequent application to meta-material design.

The volume averaging analysis is capable of producing accurate meta-material moduli for some situations in which asymptotic homogenization cannot. Volume averaging analyses have no limiting assumptions of UC scaling with the global meta-material. While RVE limits

may still apply, thin-layered meta-materials (e.g., the shear beam of the non-pneumatic wheel) can be designed provided enough UCs are included along the length of the layer.

1.3.2 Secondary Hypotheses

Given an accurate meta-material analysis method using volume averaging, a topology optimization method can be devised to design meta-materials in a manner similar to that of asymptotic homogenization. Functionally, asymptotic homogenization and volume averaging both produce meta-material moduli. Thus, the topology optimization process for homogenization can be employed using the volume averaging method provided that element sensitivities can be derived.

Either analysis and optimization method can be extended to non-simply connected UC lattices. The motivation to do so is to simplify the analysis of honeycomb structures using rectangular, non-simply connected UCs (as opposed to a more complicated analysis employed by parallelogram-shaped UCs), and, perhaps, produce different structures in topology optimization with a broader range of achievable meta-material moduli.

1.3.3 Research Questions

The research hypotheses are quantified by the following questions to be answered in this body of work:

1. Are there applications in which homogenization theory is not capable of predicting accurate meta-material moduli? If so, can the volume averaging method be used?
2. Can a well-posed meta-material topology optimization problem be constructed to target meta-material properties?
3. Is it possible to topology optimize with respect to the parameters of the volume averaging model?
 - Can a single unit cell be optimized in tension and in shear?

- Can multiple unit cells be optimized in tension and in shear?
4. How does unit cell connectivity affect the physical modeling methods (asymptotic homogenization and volume averaging) presented?
 5. Can the non-pneumatic wheel assembly design problem be solved using the volume averaging method with topology optimization?

1.4 Dissertation Outline

The remainder of the dissertation is organized as follows.

Chapter 2 provides an overview of the pertinent literature, including meta-materials analysis methods and topology optimization of materials.

Chapter 3 demonstrates the limits of asymptotic homogenization in the design thin-layered materials and materials containing poorly-scaled rectangular unit cells. The volume averaging analysis is also tested under the same conditions, and a simple design problem is posed to demonstrate accuracies and inaccuracies for each of the two analysis methods.

Chapter 4 addresses the optimality conditions of several meta-material optimization problems.

Chapter 5 provides optimization setup, element sensitivities and results for optimization of single and multiple cell problems analyzed using volume averaging.

Chapter 6 addresses the question of unit cell connectness through the analysis of honeycomb structures, and the same design problem in Chapter 2 is used to demonstrate accurate and inaccurate methods. Then the optimization methods for volume averaging proposed in Chapter 4 are extended to the design of materials with non-simple periodicity.

Chapter 7 describes the solutions of the design of the meta-material optimization of the non-pneumatic wheel.

Chapter 8 provides concluding remarks and the suggested direction of future work.

Chapter 2

Literature Review

To create a successful computational design method using optimization, an accurate analysis of the problem must be used to determine the design variables, design constraints and objective function. After the problem is formulated, a method must be used to update the design variables. In this chapter, a literature review of the prevalent meta-material analysis methods is presented. Then, a review of the relevant literature about topology optimization is given, with the scope of the review being placed on methods used to solve the meta-material design problem.

2.1 Meta-Materials Analysis

The design of meta-materials in a systematic manner requires decoupling the global design problem from the meta-material problem, as shown in Figure 1.3. The meta-material is discretized into unit cells (UCs), the basic building blocks that contain the simplest and smallest possible structures that can be repeated to generate the entire meta-material. In the UC discretization process, the periodicity of the meta-material is defined, typically a priori. Then an appropriate meta-material analysis is applied to the system to determine effective meta-material properties E_{ij}^M . These properties are passed to the optimizer for design variable updating to determine the UC topology. A key aspect is that the meta-

material perform as predicted in the global assembly. While it is not obvious, equality of the meta-material properties E_{ij}^M and those of the homogeneous material E_{ij}^* substituted in the global level does not necessarily guarantee proper performance of the meta-material in the assembly. These issues, as understood from the literature, are addressed below.

2.1.1 Discretization Into Unit Cells and Establishing Periodicity

In meta-material design, the domain is discretized into a set of periodic UCs (Figure 2.1), with the same geometry being repeated in every UC. But the choice of how the UCs connect, their shape and their size relative to the global scale of the material dictate the choice of analysis to be applied.

The shape and connectivity are described by the periodicity of a lattice on which the UCs lie. Hassani and Hinton [5] discuss the idea of periodicity in the meta-material design problem: a material with position vector $z = (z_1, z_2, z_3)$ is Y-periodic if, for all material characteristics described by function F ,

$$F(z + NY) = F(z) \quad (2.1)$$

where

$$N = \begin{bmatrix} n_1 & 0 & 0 \\ 0 & n_2 & 0 \\ 0 & 0 & n_3 \end{bmatrix} \quad (2.2)$$

and n_i are integers. $Y = \{Y_1, Y_2, Y_3\}$ is some vector that contains the periodicity of the structure, and F is any scalar, vector or tensor function of vector z (see Figure 2.2). Using the constitutive law for a linear elastic material

$$\sigma_i = E_{ij}\varepsilon_j \quad (2.3)$$

in the linear meta-material optimization scheme, the material properties E_{ij} , by virtue of

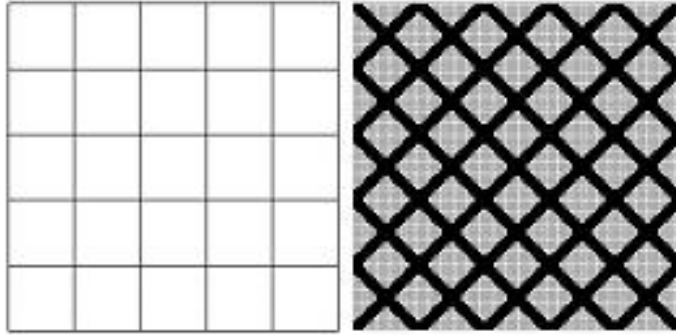


Figure 2.1: (Left) Depiction of UCs with square, simply-connected periodicity. (Right) A meta-material structure with the periodicity depicted on the left.

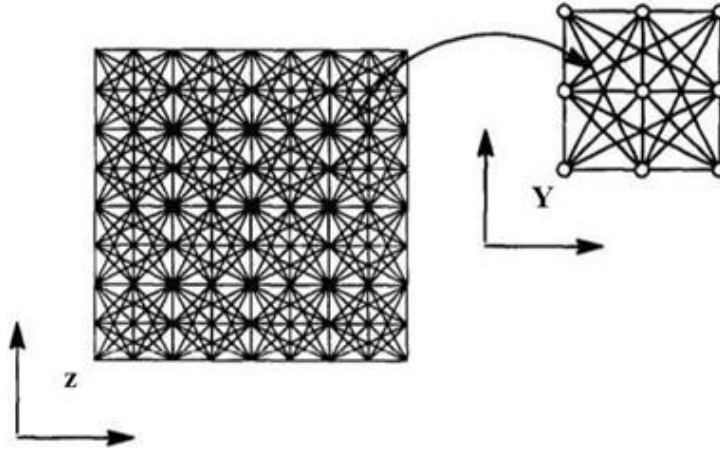


Figure 2.2: Material structure with global material coordinates z on the left, discretized into ground structure cells to be optimized with base cell coordinates Y on the right. [20]

periodicity of the lattice, are Y -periodic if

$$E_{ij}(z + NY) = E_{ij}(z) \quad (2.4)$$

The periodicity vector Y directly depends on the choice of the UC geometry and the orientation of one UC with respect to the surrounding UCs comprising the meta-material structure. The design domains described in the original works by Sigmund [20], [21] are composed of simply-connected, square UCs (as shown in Figure 2.1). (By simple connectivity, each edge is juxtaposed with only one edge of a different UC.) Bénard and Diaz [22] assert that choosing a UC geometry directly limits the set of achievable meta-material

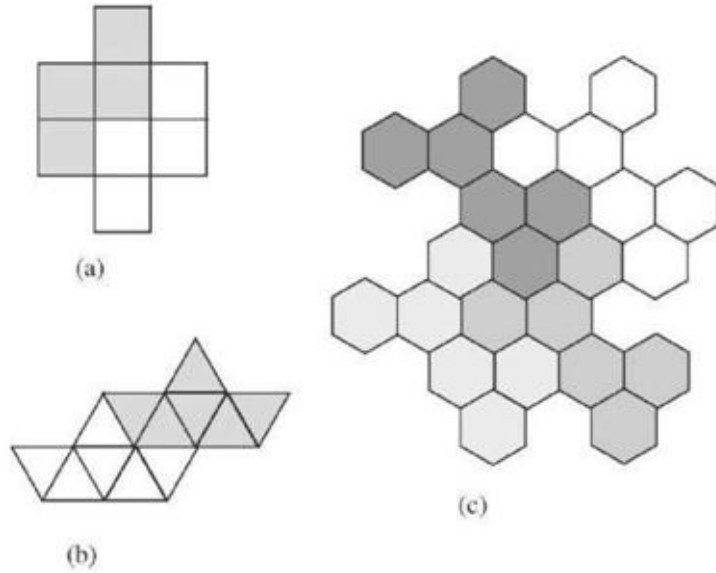


Figure 2.3: Three different monohedral, periodic tilings of a planar space. Each prototile is made out of tiles of the same color. For example, in (a), each prototile is constructed from four square tiles. [22]

designs, and they provide a systematic, mathematical framework with which to describe the engineering design problem. The authors first define a tiling as a countable family of closed sets that covers a plane without gaps or overlaps. They only consider monohedral, periodic tilings, those tilings that consist of a single prototile repeated by translation only throughout the plane (Figure 2.3):

$$T = P + n_1y_1 + n_2y_2 \quad (2.5)$$

where P is the prototile, n_i are integers, and y_i are the tiling vectors that describe the translation of the prototile.

A lattice is defined as a collection of translates of a single point $p \in P$, where P is used to create the periodic tiling T . Mathematically, lattice L is written

$$L_p(p, y_1, y_2) = \{q : q = p + n_1y_1 + n_2y_2\} \quad (2.6)$$

Then the area formed by the lattice vectors y_i form a fundamental domain F associated

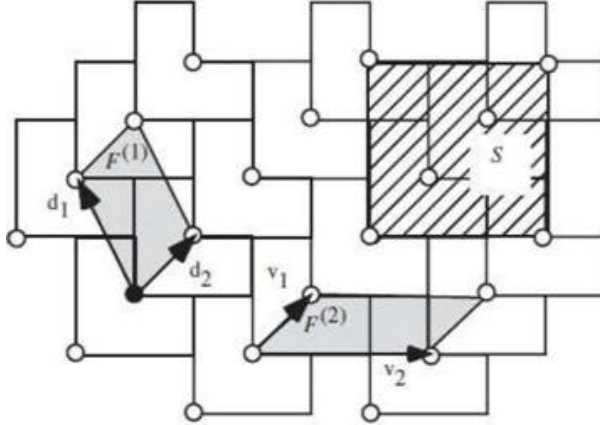


Figure 2.4: Lattice points (circles) associated with a periodic, monohedral tiling, tiling vectors and corresponding fundamental domains F . Note that, though domain S is periodic, it does not form a fundamental domain because lattice points contained within domain S are not used in domain tiling. (No tiling vectors connect the lattice points contained within S . [16])

with lattice L_p . A fundamental domain is defined as any parallelogram with corners on the lattice $L_p(p, y_1, y_2)$ that tiles the plane with tiling vectors v_1 and v_2 and generates a lattice $L_p(p, v_1, v_2)$ equal to $L_p(p, y_1, y_2)$. Note that more than one fundamental domain may exist for a lattice. Figure 2.4 shows a lattice for a monohedral, periodic tiling with lattice points (circles), tiling vectors, and associated tiling vectors and fundamental domains.

In a later work, Diaz and Bénard [16] show that periodic homogenization on a generic tiling can be replaced by an equivalent problem using simple parallelograms, the fundamental domains, as UCs, making the homogenization problem more computationally efficient. The authors point out that this, in turn, increases the efficiency of obtaining possible solutions of meta-material geometries that can only be reached by considering non-rectangular UCs.

Systematic meta-material design processes by topology optimization have become much more advanced by loosening constraints from the basic optimization problem. (For example, see the work of Paulino et al. [23].) In Figure 2.1, the design domain is discretized into a set of simply-connected, square UCs (the discretization process is independent of the local optimization objective function). In the paper by Diaz and Bénard [16], the equality

constraints on the side lengths and internal angles are lifted. This opened up the ability to formulate a meta-material design problem in which honeycomb designs could be obtained, as reported briefly in the original work by Diaz and B enard [16] by directly targeting material properties subject to material volume constraints. Lipperman et al. [17] obtained honeycomb geometries by maximizing material strength (minimizing the maximum local von Mises stress) subject to material volume constraints.

2.1.2 Asymptotic Homogenization

Many different material design problems have been solved using the asymptotic homogenization approach, including elastic design of structures with extremal properties [24], [25], multi-material problems [26], [27], [28], functionally graded materials [23], piezoelectric problems [29], [30], [31], electromagnetic composites [32], and multidisciplinary problems involving elasticity and permeability [33], [34] and fluid permeability and structure [35]. Asymptotic homogenization approaches have also been developed for multiload scenarios [36] and for robust design under manufacturing uncertainty [37], [38], [6]. Another method directly utilizing the strain energy function [19] has been developed since Sigmund’s original publications.

Hassani and Hinton offer a thorough review of homogenization theory, implementation, and topology optimization using homogenization [5], [39], [40]. The key assumption for material homogenization is that the individual dimensions of the UC are very small when compared to the dimensions of the overall domain of the global material for which the homogenized material properties are desired. Given this assumption, the governing physical equations of the UC are expanded in terms of a small parameter, and periodicity constraints are enforced on the UC to achieve equivalent displacements on the boundaries of the UC. When these periodicity constraints are enforced directly on the boundaries of the UC, it is called a representative unit cell (RUC).

The implementation of the material homogenization procedure requires solving three problems that simulate three different modes of deformation, two in uniaxial tension and

one in shear, subject to the necessary periodicity constraints. Due to the complicated microstructures that are often present in UCs, these problems are typically solved using FEA. In this case, the stiffness matrix K that contains the linear material properties for the square UC is assembled, and the equations

$$f_i = B^T d_i \quad (2.7)$$

are used to obtain the load vectors applied to each of three FEAs, denoted by subscript i . Here, B is the strain-displacement matrix, and the vectors d_i are those obtained by applying unit strains

$$\varepsilon_1^0 = \{1 \ 0 \ 0\}^T, \varepsilon_2^0 = \{0 \ 1 \ 0\}^T, \varepsilon_3^0 = \{0 \ 0 \ 1\}^T \quad (2.8)$$

to the UC according to

$$d_i = D\varepsilon_i^0 \quad (2.9)$$

D is the material elasticity matrix relating material stress and strain of the base material (where the stress and strain matrices have been converted to vectors in the traditional manner by taking advantage of the tensor symmetries). Thus, the d_i is simply the i -th column of the material linear constitutive matrix D .

Given the loads f_i from Eq. 2.7 and the assembled stiffness matrix K , the solutions displacement fields of the FEAs, Φ_i , are found using the finite element equation

$$K\Phi_i = f_i \quad (2.10)$$

subject to periodicity constraints

$$\chi_i(y_1, y_2) = \chi_i(y_1 + L, y_2) = \chi_i(y_1, y_2 + W) = \chi_i(y_1 + L, y_2 + W) \quad (2.11)$$

(where $\chi_i \subseteq \Phi_i$ denotes the boundary displacements). The enforcement of periodicity constraints (Eqs. 2.11) distinguishes the RUC from the UC (no periodicity constraints

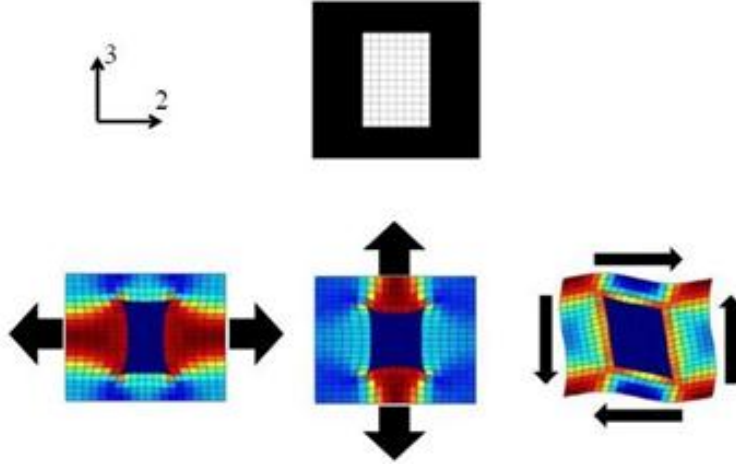


Figure 2.5: Homogenization analysis examples. The top figure is the meta-material found in [18], and the bottom figures are the displaced meta-materials with von Mises stresses represented by different the variance in shading. From left to right are the E_{22}^H , E_{33}^H and G_{23}^H analyses.

enforced). Finally, the homogenized meta-material properties E_{ij}^H are given by integrating over the RUC with domain $Y = LW$, where L and W are the individual lengths of the RUC:

$$E_{ij}^H = \frac{1}{Y} \int_Y (D_{ij} - d_i^T \varepsilon_i^0(\Phi_i)) dY \quad (2.12)$$

An example meta-material geometry taken from Bendsøe and Kikuchi [41] is shown in Figure 2.5, along with results of the homogenization analysis for the three meta-material properties E_{22}^H , E_{33}^H and G_{23}^H , which are the two Young's moduli and the shear modulus of the meta-material. The arrows do not represent physical boundary conditions, but they, instead, depict directions in which the homogenization analysis is applied. This example serves as a validation point for homogenization analysis code.

2.1.3 Volume Averaging Analysis

The volume averaging analysis method uses the average strain and average stress theorems to integrate over the UC with domain $Y = LW$:

$$\bar{\varepsilon}_i = \frac{1}{Y} \int_Y \varepsilon_i dY \quad (2.13)$$

$$\bar{\sigma}_i = \frac{1}{Y} \int_Y \sigma_i dY \quad (2.14)$$

respectively. By simulating modes of deformation, two in tension and one in shear, on the boundaries of the UC and determining the average strains $\bar{\varepsilon}_i$ and average stresses $\bar{\sigma}_i$, the effective meta-material parameters E_{ij}^* can be determined as a solution of

$$\bar{\sigma}_i = E_{ij}^* \bar{\varepsilon}_i \quad (2.15)$$

Like homogenization analysis, the composites analysis problem has also been extensively studied. Hollister and Kikuchi [42] were the first to report a comparison between these two analytical methods. Through FEA, the authors quantitatively investigated the convergence of the direct analyses to homogenization by comparing estimates of the local strain energy densities for each method. They concluded that homogenization theory was preferable over composite analysis methods due to a knowledge gap at that time about uniqueness of stress and strain in boundary condition application. This work was followed up by Pecullan et al. [43]; here, the authors investigated the effects of using homogeneous displacement versus homogeneous traction boundary conditions for composites analysis. They concluded that, for material domains with lower volume fraction (ratio of material volume to total unit cell volume), traction boundary conditions were more accurate for predicting meta-material properties, whereas displacement boundary conditions were more accurate for high volume fraction material domains. Further numerical studies were performed to see the effect that differing types of boundary conditions has on predicted effective moduli for heterogeneous materials [44], [45].

These issues were clarified by careful consideration of the distinguishing characteristics of the UC, the RUC and a representative volume element (RVE). Pindera et al. [46] describe in detail the difference between these. A RUC is obtained by applying unit strains of Eqs. 2.8 in the FEA scheme subject to periodic boundary conditions from Eqs. 2.11 to a UC, whereas the RVE idea is derived from consequences of modeling using traction or

displacement boundary conditions.

To understand the meaning of the RVE, consider a system modeled using either homogeneous strain or homogeneous stress boundary conditions; then Eqs. 2.13 and 2.14 will produce prescribed average strains ε_i^0 or prescribed average stresses σ_i^0 , respectively. The average strain energy of the system using the averaging theorems is

$$U_e = \frac{1}{2} \bar{\sigma} \bar{\varepsilon} \quad (2.16)$$

An RVE is defined as the necessary representative volume such that the strain energy of the system is equivalent whether displacement or traction boundary conditions are applied, or

$$\frac{1}{2} \bar{\sigma}_i \bar{\varepsilon}_i = \frac{1}{2} \sigma_i^0 \bar{\varepsilon}_i = \frac{1}{2} \bar{\sigma}_i \varepsilon_i^0 \quad (2.17)$$

Clearly, for a homogeneous material, this is always true. For a non-homogeneous material, one that satisfies Eq. 2.17 is called statistically homogeneous when the total volume averaged over becomes large enough to satisfy the RVE requirement. In the case of periodic meta-materials analysis, this corresponds to choosing a volume to include a large enough number of UCs to satisfy Eq. 2.17.

For fiber-composites materials (with orthotropic material properties), Drago and Pindera [47] show that the predicted effective moduli of the composites, the components of the tensor from the linear constitutive law relating average stress and average strain, do not necessarily coincide with each other or with those predictions given by asymptotic homogenization analysis: different effective moduli for displacement boundary conditions E_{ij}^U and traction boundary conditions E_{ij}^T are obtained. However, the individual components of these tensors satisfy Eq. ?? in the limit that enough UCs are included such that the scale of UCs within the RVE become small enough to meet the scaling assumptions of the asymptotic homogenization theory, and the individual components of E_{ij}^U and E_{ij}^T converge to E_{ij}^H .

Given the convergence to homogenization analysis, the body of work in [46] and [47]

also serves to clarify the proper boundary conditions needed on the unit cell for composites analysis (using either the traction or displacement method). Depictions of a single unit cell in tensile and shear deformation using displacement boundary conditions are shown in Figure 2.7, while depictions of a single unit cell in tensile and shear deformation using traction boundary conditions are shown in Figure 2.8.

The convergence of the two analytical methods in the RVE limit is nicely depicted in a representative example from Drago and Pindera [47]. The meta-material shear modulus is evaluated using the displacement and traction boundary conditions in Table 2.1 and Table 2.2 (yielding G_{23}^U and G_{23}^T , respectively), as well as the more widely-reported homogenization analysis described in the previous section (yielding G_{23}^H). To do this, the analytical methods are applied as intended: on a single cell for homogenization, and on a grid of $N \times N$ cells using the volume averaging methods (N is a positive integer). The total analysis domain volume is held constant in the composites analysis case, and the sizes of the UCs are reduced to fit into the domain at every step (Figure 2.9). According to homogenization theory, enough UCs must be included in the design domain to achieve the scaling limit at which the small-parameter expansion is applicable. And according to Eq. 2.17, the RVE limit is obtained when the moduli obtained by the displacement and traction boundary conditions coincide. In Figure 2.10, for the particular design example, the composite shear moduli converge asymptotically to the homogenized shear modulus. The authors demonstrate that, when homogenization scaling limits are applicable, the RVE limit is simultaneously obtained; however, the two are ideas not necessarily equivalent.

2.2 Topology Optimization

While topology optimization (TO) subfields are all intended for very different purposes, they share a common set of numerical methodologies. It is the choice of a particular physical analysis, not numerical methodology, that separates the different subfields. Yin and Ananthasuresh [48] provide a good overview of the development of a TO algorithm by

Table 2.1: Displacement Boundary Conditions for Volume Averaging Analysis [47]

<i>Transverse Normal Loading - E_{22}^U (E_{33}^U is similar)</i>		
S_1	$u_2(z_2, -h) = \varepsilon_{22}^0 z_2$	$u_3(z_2, -h) = -\varepsilon_{33}^0 h$
S_2	$u_2(h, z_3) = \varepsilon_{22}^0 h$	$u_3(h, z_3) = \varepsilon_{33}^0 z_3$
S_3	$u_2(z_2, h) = \varepsilon_{22}^0 z_2$	$u_3(z_2, h) = \varepsilon_{33}^0 h$
S_4	$u_2(-h, z_3) = -\varepsilon_{22}^0 h$	$u_3(-h, z_3) = \varepsilon_{33}^0 z_3$
z_2 -axis	$u_2(0, z_3) = 0$	$\sigma_{23}(0, z_3) = 0$
z_3 -axis	$u_3(z_2, 0) = 0$	$\sigma_{23}(z_2, 0) = 0$
<i>The average strain ε_{33}^0 is determined subject to the integral constraint $\bar{\sigma}_{33} = 0$ on S_1 and S_3.</i>		

<i>Transverse Shear Loading - G_{23}^U</i>		
S_1	$u_2(z_2, -h) = -\varepsilon_{23}^0 h$	$u_3(z_2, -h) = \varepsilon_{23}^0 z_2$
S_2	$u_2(h, z_3) = \varepsilon_{23}^0 z_3$	$u_3(h, z_3) = \varepsilon_{23}^0 h$
S_3	$u_2(z_2, h) = \varepsilon_{23}^0 h$	$u_3(z_2, h) = \varepsilon_{23}^0 z_2$
S_4	$u_2(-h, z_3) = \varepsilon_{23}^0 z_3$	$u_3(-h, z_3) = -\varepsilon_{23}^0 h$
z_2 -axis	$u_3(0, z_3) = 0$	$\sigma_{22}(0, z_3) = 0$
z_3 -axis	$u_2(z_2, 0) = 0$	$\sigma_{33}(z_2, 0) = 0$

Table 2.2: Traction Boundary Conditions for Volume Averaging Analysis [47]

<i>Transverse Normal Loading - E_{22}^T (E_{33}^T is similar)</i>		
S_1	$\sigma_{22}(z_2, -h) = 0$	$\sigma_{33}(z_2, -h) = 0$
S_2	$\sigma_{22}(h, z_3) = \sigma_{22}^0$	$\sigma_{33}(h, z_3) = 0$
S_3	$\sigma_{22}(z_2, h) = 0$	$\sigma_{33}(z_2, h) = 0$
S_4	$\sigma_{22}(-h, z_3) = -\sigma_{22}^0$	$\sigma_{33}(-h, z_3) = 0$
z_2 -axis	$u_2(0, z_3) = 0$	$\sigma_{23}(0, z_3) = 0$
z_3 -axis	$u_3(z_2, 0) = 0$	$\sigma_{23}(z_2, 0) = 0$
<i>Transverse Shear Loading - G_{23}^T</i>		
S_1	$\sigma_{23}(z_2, -h) = -\sigma_{23}^0$	$\sigma_{33}(z_2, -h) = 0$
S_2	$\sigma_{23}(h, z_3) = \sigma_{23}^0$	$\sigma_{22}(h, z_3) = 0$
S_3	$\sigma_{23}(z_2, h) = \sigma_{23}^0$	$\sigma_{33}(z_2, h) = 0$
S_4	$\sigma_{23}(-h, z_3) = -\sigma_{23}^0$	$\sigma_{22}(-h, z_3) = 0$
z_2 -axis	$u_3(0, z_3) = 0$	$\sigma_{22}(0, z_3) = 0$
z_3 -axis	$u_2(z_2, 0) = 0$	$\sigma_{33}(z_2, 0) = 0$

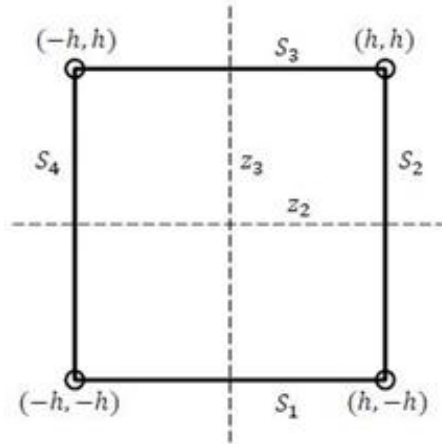


Figure 2.6: Unit cell parameters for the volume averaging analysis given in Table 2.1 and Table 2.2.

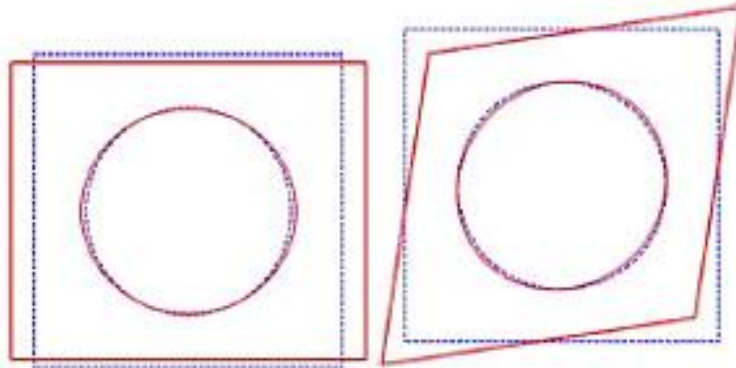


Figure 2.7: Unit cell of a meta-material under homogeneous displacement tension (left) and shear (right) boundary conditions as listed in Table 2.1. The material of circular inclusion has ten times the Young's modulus of the matrix surrounding it. [47]

breaking it into four distinct parts: designing a well-posed objective function, determining and implementing an appropriate material interpolation function, applying appropriate constraints to the problem for efficient analysis, and choosing an efficient optimization algorithm to produce the most valid results. A discussion of each issue follows.

2.2.1 Choosing an Appropriate Objective Function

In TO of elastic structures, the primary concern of the designer is to minimize the chance of failure of the structure given a specified set design loading or displacement

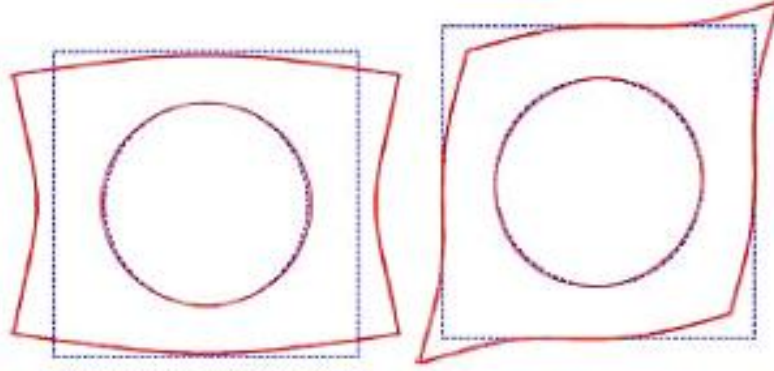


Figure 2.8: Unit cell of a meta-material under homogeneous traction tension (left) and shear (right) boundary conditions as listed in Table 2.2. The material of circular inclusion has ten times the Young's modulus of the matrix surrounding it. [47]

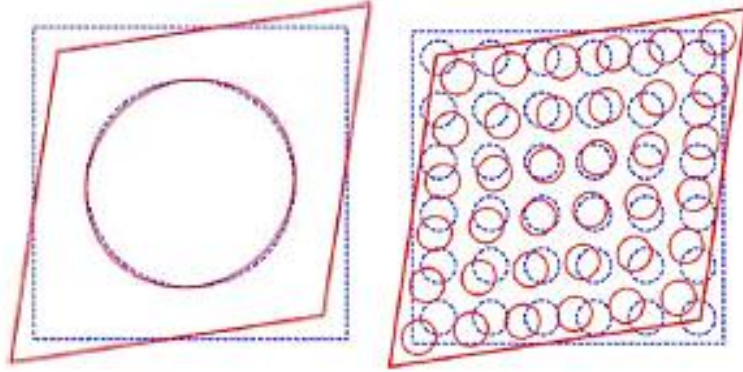


Figure 2.9: (Left) Single unit cell ($N \times N$ analysis with $N = 1$). (Right) 6×6 unit cell analysis ($N \times N$ analysis with $N = 6$). The two analytical volumes are the same. [47]

boundary conditions. From material failure theory, the most commonly-used and often most accurate theory of failure is the maximum-distortion-energy theory, developed initially by Huber and refined independently by von Mises and Hencky [49]. This theory posits that it is the distortion energy, and specifically not the hydrostatic energy, that dictates the failure of an elastic material under deformation. This distortion energy is quantified by the elastic strain energy density u_e :

$$u_e = \sum_i \frac{1}{2} \sigma_i \varepsilon_i \quad (2.18)$$

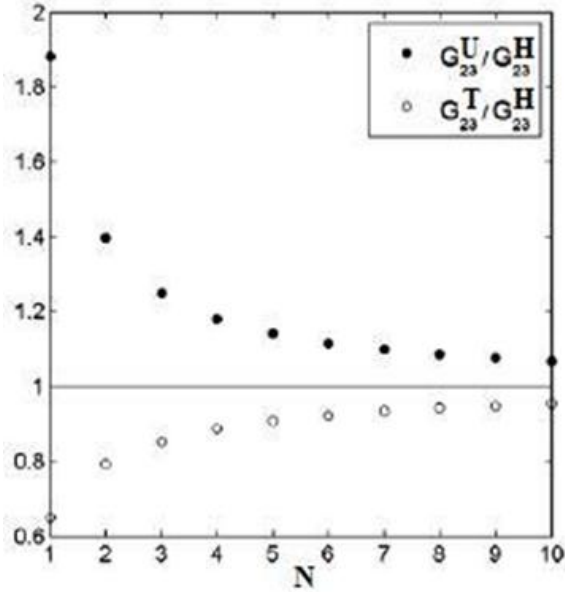


Figure 2.10: $N \times N$ unit cell analysis for shear moduli of cell depicted in Figure 2.9 as analyzed by Drago and Pindera [47]. The traction and displacement moduli (denoted by 'T' and 'U' superscripts) are divided by the homogeneous modulus for the single cell (denoted by 'H' superscript).

where σ_i and ε_i are the principal stresses and strains on a piece of material in principal direction i , respectively [49]. Given this, it makes physical sense to choose an objective function that somehow encapsulates the strain energy U_e (total strain energy of the system) if optimal performance from failure is desired. Employing Hooke's law for linear elastic materials, the total strain energy can be found by summing the strain energy density over the total material volume Y :

$$U_e = \frac{1}{2} \int_Y \varepsilon_i E_{ij} \varepsilon_j dY \quad (2.19)$$

where E_{ij} is the constitutive tensor relating stress and strain in Hooke's Law.

For TO of lightweight structures for optimal performance from failure, the most common physical function used in research and commercial software packages is the compliance. The minimum compliance formulation is found in a number of sources, including Bendsøe and Sigmund [50] and Eschenauer and Olhoff [51]. The external loading L_{ex} on a

structure, given in terms of body forces f and tractions t , is given by

$$L_{ex} = \int_Y \mathbf{f} \cdot \mathbf{u} dY + \int_{\Gamma_t} \mathbf{t} \cdot \mathbf{u} d\Gamma_t \quad (2.20)$$

Γ_t is the boundary of the design domain on which tractions are applied, and \mathbf{u} is the linear material displacement field. By minimizing L_{ex} , the strain energy of the design domain is also minimized by virtue of the equilibrium requirement that the external loading is equal to twice the internal strain energy:

$$L_{ex} = 2U_e \quad (2.21)$$

(The minimum compliance formulation is sometimes referred to as the minimum strain energy formulation, due to the equilibrium condition given in Eq. 2.21). At equilibrium, the compliance C is defined as the work done by the loads on the structure against the internal displacements of the structure [51]:

$$C := L_{ex} \quad (2.22)$$

Thus, the minimum compliance problem, for TO is commonly written

$$\begin{aligned} & \min_{\mathbf{v}} C(\mathbf{v}) \\ & \text{s.t. } C(\mathbf{v}) = 2U_e(\mathbf{u}, \mathbf{v}) \end{aligned} \quad (2.23)$$

where \mathbf{u} and \mathbf{v} represent the set of admissible equilibrium displacement fields. Because the continuum problem is very difficult to solve with the exception of only very simple examples, FEA is applied to discretize the equations of Problem 2.23:

$$\begin{aligned} & \min_{\mathbf{x}} C(\mathbf{x}) \\ & \text{s.t. } \mathbf{K}(\mathbf{x})\mathbf{u} = \mathbf{f} \\ & V(\mathbf{x}) \leq V_0 \end{aligned} \quad (2.24)$$

$\mathbf{K}(\mathbf{x})$ is the stiffness matrix, C is the compliance function and \mathbf{x} is the vector of finite-element densities that serve as optimization variables. (The finite-element meshing, called material interpolation when discussed in the context of topology optimization, is a non-trivial matter; it is discussed in more detail in section 2.2.2.) This formulation is particularly convenient, as the constraint equation in Problem 2.24 is that used by the finite element solver to determine displacements \mathbf{u} at equilibrium (for elastic materials exhibiting linear deformation). Thus, system equilibrium is implicitly enforced in the FEA of the problem; it is stated in Problem 2.24 only as a mathematical formality.

The other constraint enforced in Problem 2.24 is an engineering constraint on the material volume V , directly enforcing the engineering desire to use less material. Other than bounds on the optimization variables \mathbf{x} , most often, this constraint is the only explicitly enforced constraint in TO. The total volume is a simple constraint to enforce, as V is easily parameterized by element density. (Depending on the choice of material interpolation, this constraint takes the form of structural weight instead of material volume when beam elements are used; the effective implementation of the constraint is the same.) It is common for the volume constraint to be active upon successful termination of the optimization routine, implying the choice volume constraint bound V_0 is crucial. While this effect is seen throughout the literature, it is not an important talking point, as this constraint can be tuned to the designer's purpose without loss of fidelity in the physical modeling or optimization.

While both TO and compliant topology optimization (CTO) utilize some form of the compliance objective directly, meta-material optimization (MMO) requires a particular material property E_{ij}^* be achieved by the system (the subscripts denote the components of the effective linear material constitutive tensor). While strain energy (or compliance) is not minimized in MMO, an optimal value is achieved as part of optimization. This can be seen by rewriting Eq. 2.19 in terms of the meta-material property E_{ij}^M .

$$U_e = \frac{1}{2} \bar{\varepsilon}_i E_{ij}^M \bar{\varepsilon}_j \quad (2.25)$$

(The meta-material property is essentially just some sort of volume average or homogenized value, obtained from applying some type of averaged strain $\bar{\epsilon}_i$ or corresponding averaged stress $\bar{\sigma}_i$ to the system. These methods are a key piece of this body of research, and will be discussed in a proceeding section.) Then, the target property is obtained by constraining the difference between the meta-material property E_{ij}^M and the target property in an optimization method or by directly minimizing this difference. For example, the optimization can be formulated

$$\begin{aligned} \min_{\mathbf{x}} \quad & V(\mathbf{x}) \\ \text{s.t.} \quad & \mathbf{K}(\mathbf{x})\mathbf{u} = \mathbf{f} \\ & E_{ij}^* - E_{ij}^M = 0 \end{aligned} \tag{2.26}$$

In Problem 2.26, the material volume is minimized, while the material property to be achieved is constrained ([20], [21] and sources therein). Currently, the only meta-material optimization procedure reported in the literature uses asymptotic homogenization analysis to compute meta-material properties and corresponding design variable sensitivities for targeting meta-material properties (as given in Problem 2.26) or extremizing a particular meta-material property (by making the meta-material property the objective function subject to the volume fraction constraint).

2.2.2 Material Interpolation Schemes

Three types of material interpolation schemes for single-material optimization are commonly found in the literature: homogenization, penalization methods, and ground structure. The first two interpolation schemes listed are continuum material approaches.

The ultimate goal of the continuum approaches, realized through finite element modeling (most often with 4-node, square, shell elements), is to achieve a 1-0, or "black-and-white", value for the density of each finite element, corresponding to the presence or absence of material in that element. However, the numerical implementation of a strictly

1-0 integer interpolation leads to optimal designs that are dependent on the discretization, making the 1-0 interpolation ill-posed in the sense that finer microstructures appear with the inclusion of more finite elements in the analysis. By instead continuously approximating the 1-0 space by admitting intermediate densities, this dependency may be eliminated [52]. (Bendsøe and Sigmund [52] offer a more thorough review of the difficulties of 1-0 topology optimization.)

The older of the two continuum approaches, homogenization, was first implemented numerically by Bendsøe and Kikuchi [41]. In this scheme, the microstructure of an elastic material (isotropic, orthotropic, or otherwise) is averaged over for each finite element, resulting, for example, in three geometric parameters in two dimensions (Figure 2.11). The density $x_e \in (0, 1]$ of the finite element and the elasticity tensor of the material are parameterized by α , β , density control variables and θ , an orientation variable. These then serve as variables for the topology optimization problem. (For a more detailed discussion of homogenization see Bendsøe [53] and sources therein.) A finite element is then filled with material if the density of the element is greater than a certain value, usually 0.3.

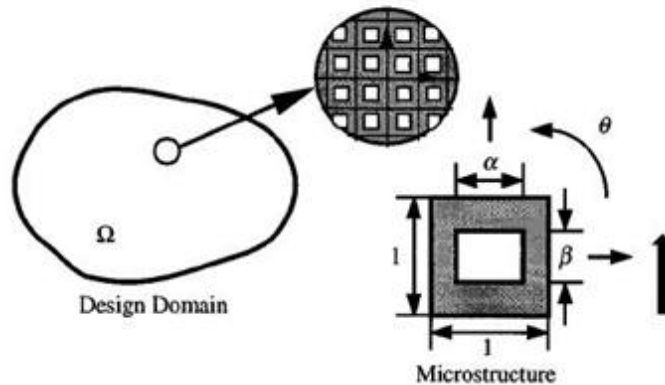


Figure 2.11: Schematic of the asymptotic homogenization process. The microstructure of a unit cell (corresponds to a finite element) is parameterized by geometric variables α , β , and θ . [2]

Although homogenization has commonly been used for the design of stiff structures, it has been used less frequently in the past decade, replaced by the most popular of the

continuum approaches, Solid Isotropic Material with Penalization (SIMP) interpolation scheme. This scheme was built to push toward a more 1-0 density distribution by penalizing intermediate material densities according to

$$x_e \rightarrow x_e^s \tag{2.27}$$

where x_e denotes the density of material in element e , and $s > 1$ is a parameter that pushes material densities toward one or zero. This method was first proposed as the power law method by Bendsøe [54], and it was first numerically implemented by Rozvany et al. [55]. The Young's modulus for element e is interpolated as

$$E_e = x_e^s E_0 \tag{2.28}$$

(E_0 is the Young's modulus of the material chosen for manufacturing.) The penalization parameter s is usually chosen as 3 based on experience [28], as it needs to be large enough to penalize intermediate densities to obtain a distribution of material close to a 1-0 distribution. The topology optimization software Optistruct built by Altair Engineering, Inc. utilizes the SIMP interpolation model [1]. A depiction of the effect of penalization on the element density using the SIMP model as given in Eq. 2.28 is show in Figure 2.12.

Because of its wide-spread use in TO, the convergence of the SIMP method in optimization has gained some attention. Rietz proved that, assuming a discrete 1-0 solution exists for the TO Problem 2.24, the SIMP method also has a discrete solution for finite values of the penalization parameter s , assuming the derivatives with respect to element densities $\partial C/\partial x_e$ of the objective function are bounded [56]. In a paper by Martinez [57], these limiting assumptions were shown to be weaker than reported by Rietz. Martinez proved that, given a sufficiently large value of the penalization parameter s , any solution to the SIMP problem approaches the solution to the discrete 1-0 problem. Further, the solution to the SIMP problem can be rounded to a discrete 1-0 problem solution if the penalization parameter s is finite.

The SIMP method has been extended beyond single material, linear elastic problems. Bendsøe and Sigmund [52] extended the SIMP approach to include multiple elastic, isotropic materials. Pederson et al. [58] used SIMP to create optimal solutions for large-displacement compliant mechanisms. A SIMP-like material interpolation that uses highly-peaked continuous functions (series that converge to delta functions) was developed by Yin and Ananthasuresh [48], and was easily extended to multiple materials. Bruns [59] developed SINH, a method that utilizes the hyperbolic sine function to penalize intermediate densities. Stolpe and Svanberg [60] created an interpolation similar to SIMP that eliminates the discontinuity of the derivative of the density at $x_e = 0$.

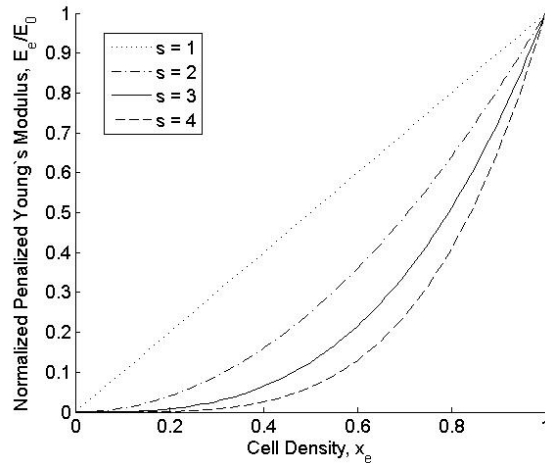


Figure 2.12: Element density versus normalized SIMP-interpolated Young's modulus. $s = 3$ (the solid line) is the generally preferred penalization factor, based off of experience and literature review.

The simplest of the three common approaches, ground structure interpolation, utilizes a set of beams to connect nodes throughout a structure (Figure 2.13). Each beam is parameterized by a set of material properties and cross-section. The cross-sections of the beams are then used as optimization variables to obtain a specified objective.

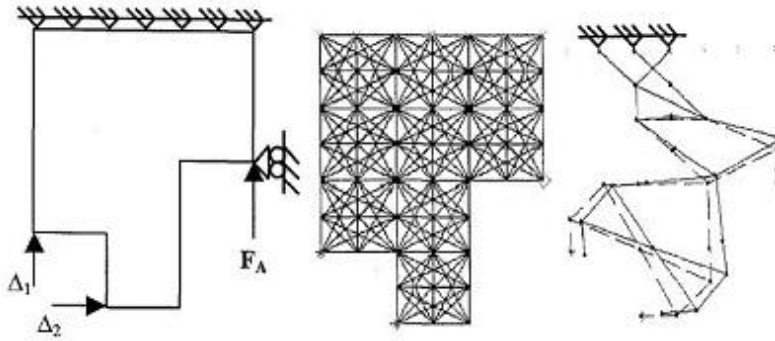


Figure 2.13: Ground structure topology design problem (left), starting point (center), and optimum (right). [61]

2.2.3 Constraining the Topology Optimization Problem

There is a standard set of constraints applied in a finite-element TO algorithm. As previously mentioned, standard equilibrium constraints are imposed implicitly in the system analysis, and a constraint on the lower bound of the density of each finite element is imposed to maintain non-singularity of the stiffness matrix [28]. The other traditional constraints are grouped into those with physical meaning and those used to eliminate numerical issues associated with the finite element discretization.

The most frequently used physical constraint in TO is the volume fraction V_0 that can serve as a lower or upper bound to the allowed physical volume in the overall problem (e.g., Problems 2.24 and 2.26). When using the ground structure interpolation, the volume constraint is often written in terms of either a weight constraint on the structure [21] or a constraint on volume [61]. It is the driver of the optimization Problem 2.24, as minimum compliance without the constraint corresponds to a fully-filled domain; however, enforcing the volume constraint requires a reduction of allowed material while achieving minimum compliance. (The volume fraction can be used as an objective function, as done in Problem 2.26. Here, in meta-material topology optimization, the difference between meta-material property and the targeted property can be used as a constraint.)

Three common numerical problems exist in TO methods that utilize finite element modeling: checkerboard patterns that correspond to an artificially high stiffness but are

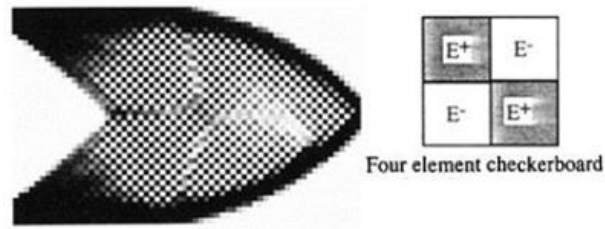


Figure 2.14: Example of a checkerboard pattern solution for a cantilever beam topology optimization problem. Elements in areas in which less material is needed "checkerboard" out, reducing overall stiffness of the structure in a way that is not physically meaningful due to connection only at the hinges of the elements. [64]

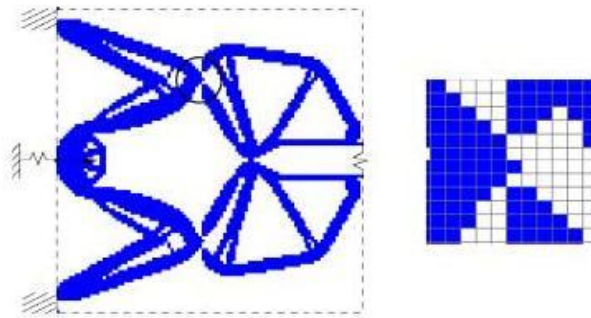


Figure 2.15: Example of a one-node connected hinge that can occur as a result of topology optimization. [62]

not physically realizable in a mechanism, one-node connected hinges that occur due to similar reasons as checkerboard patterns, and mesh-dependency of solution algorithms. Checkerboard patterns (Figure 2.14) and one-node connected hinges (Figure 2.15) are well-understood, resulting from modeling with elements of low order, in particular 4-node quadrilateral elements [62], [63], [64]. Mesh-dependency, or non-convergence of solutions with mesh refinement, is a result of finite element modeling as well. Convergent solutions should result in better-defined boundaries between material phases from one element to the next, but often finer microstructure appears as a result of mesh-refinement [28].

Several successful methods to solve these problems have been devised [62], [65], [66]. The heuristic algorithm proposed by Sigmund [67], [28] eliminates checkerboards, hinging and mesh-dependency issues by employing a filter in the algorithm that substitutes elements sensitivities for a single element with a weighted sum of all elements in a local radius. The

simple and efficient algorithm produces the same results as more costly algorithms built by other authors and is the preferred method. In these works, Sigmund also asserts this filtering technique also eliminates some local minima in the design parametrization, making optimization by gradient-based methods more reliable.

More recently, Gibert and Fadel [68] have shown that modeling with Voronoi (6-node hexagonal) elements inherently eliminates checkerboard designs and one-node hinges when applied to design for minimum compliance of a cantilever and Messerschmitt-Blkow-Blohm (MBB) beam without a need for any filtering algorithm. Similar, hexagonal Wachspres elements were shown to eliminate checkerboard problems for structural topology optimization problems [69]. However, these algorithms require using quadrilateral and triangular elements on the boundaries of design domains, complicating the finite element analysis setup [69]; additionally, the choice of finite element orientation in the domain discretization is not unique, introducing ambiguity into the discretization process and geometric bias into the optimization [70].

2.2.4 Optimization Routines

Because the TO problem presents hundreds to thousands of design variables (at least one for each finite element, regardless of the choice of interpolation), obtaining a solution to the optimization problem is difficult by nature. In addition, by simply assuming that stiffness is linearly dependent on design variables, Rozvany [71] notes that most TO problems are non-convex, and for those that are not, implementing standard interpolation schemes leads to non-convexity of the optimization problem. The addition of constraints and other design parameters only serve to increase the complexity of the TO design problem. However, Rozvany additionally notes that most engineering design problems are non-convex, due to the complexity of real-world design engineering. A detailed discussion of numerical issues in topology optimization is discussed in the review article by Sigmund and Petersson [66]. In this article, the authors attribute the existence of local minima due to the numerical complexity and inherent non-convexity of the problem, as well as the relative flatness of the

compliance objective function. Thus, this complexity must be met with robust and reliable optimization routines.

One way in which the problem is commonly solved for continuum structures is by using gradient-based methods. Gradient-based methods are more-frequently used because closed-form sensitivity equations are typically simple to derive and incur relatively little computational cost (when compared to the cost of non-deterministic solution algorithms or other zero-order methods). The use of closed-form first-order variable sensitivities (over finite difference methods) to approximate the TO problem has proved crucial, given the large number of design variables used. For example, Sigmund [28] used sequential linear programming (SLP) to solve the problem by calculating design sensitivities to create a linear approximation. The method of moving asymptotes (MMA), developed by Svanberg [72] for structural optimization problems, has also been used to determine the optimal design of large-displacement mechanisms that has been approximated using the adjoint method to determine design sensitivities [58]. Luo et al. [73] also utilized MMA [72] to solve the CTO problem with a large number of constraints. In meta-material optimization, MMA has been used in conjunction with adjoint sensitivity analysis [74], and optimality criteria (OC) methods have been used in the optimization of beam-interpolated meta-materials [21] and SIMP-interpolated continuum meta-materials [40]. Non-deterministic algorithms have been used less commonly in the optimization of continuum structures. However, these algorithms have proven useful in optimization of ground structures. A couple examples include the use of Non-dominated Sorting in Genetic Algorithms (NSGA) to design truss-like large-displacement mechanisms [75] and an evolutionary optimization technique to design compliant mechanisms with complex-shaped beam elements [76].

Given the inability to prove convergence to an optimum when using evolutionary algorithms, some controversy surrounds the choice of these algorithms in structural topology optimization. Rozvany [71] recently addressed this issue by comparing the SIMP interpolation, which is solved using deterministic methods, and evolutionary structural optimization (ESO), which is solved using non-deterministic methods. In this paper, Rozvany points

out that deterministic methods utilizing SIMP interpolations have been verified to numerically converge to mathematically proven solutions in topology optimization, and it is useful for a wide range of problems. On the other hand, he states that, “ESO is presently fully heuristic, computationally rather inefficient, methodologically lacking rationality, occasionally unreliable, with highly chaotic convergence curves. Unlike the quantitative verification of SIMP, ESO has only been ‘verified’ by vague visual comparisons with Michell topologies.” It is clear that he is a critic of the ESO method, but he brings forward the inability of non-deterministic methods to guarantee optimal solutions while having such a large computational cost, especially in the already costly TO methods. Rozvany’s criticism is supported by the fact that the vast majority of the TO methods and examples in the literature utilize some sort of gradient-based optimization rather than non-deterministic or other zero-order methods. The wide success of gradient-based topology optimization supports its continued use.

Chapter 3

Analytical Issues in Meta-Materials Analysis

It is possible for a set of optimal material properties needed by a global design to exist in which a feasible meta-material design cannot be found within manufacturing constraint limits. A good example of this is the design of a non-pneumatic wheel, in which the vertical thickness of the wheel is of the same order of length as the global design, and the microscopic scaling assumption of asymptotic homogenization is no longer met. Composites made of a single or only a few layers of UCs also present the same issue. The scaling assumption of asymptotic homogenization may be relaxed to find meta-material geometries that satisfy global design targets, but weakening these scaling assumptions may have consequences on the accuracy of the asymptotic homogenization analysis and subsequent designs, an error which then propagates upon integration of the meta-material component into the global design.

The volume averaging analysis, which was reviewed in Ch. 2 and is described in detail by Drago and Pindera [47] and Pindera et al. [46], offers an alternative to homogenization. Because the averaging analysis is derived from a more general mathematical principle, there are no scaling assumptions placed on the analysis domain, which is a key difference from the scaling assumptions placed on the domain of asymptotic homogeniza-

tion. This makes the averaging analysis a candidate for meta-material design for systems in which these scaling assumptions cannot be met due to realistic manufacturing constraints.

In this chapter, the importance of considering these scaling effects is shown by comparing effective meta-material moduli obtained for the same material geometries using the two different analyses. Multi-cell analysis results are presented as part of this discussion to demonstrate the convergence of the average strain/average stress method to asymptotic homogenization results. Then the homogenization restriction is lifted in two separate ways: first, single UC meta-material properties are analyzed for large aspect ratio rectangular cells (in which the width to length ratios W/L are different from one), and, second, by analyzing the properties of a single-layer composite material. The restriction of a well-scaled UC is lifted in single-layer materials as well by considering layers consisting of highly rectangular cells. Then, the two analysis methods, homogenization and volume averaging, are applied to a simple, two-level design of a meta-material in shear problem in which a displacement is targeted at a global level while a meta-material property is targeted at the lower level to satisfy the top-level design goal.

3.1 Comparison of Homogenization and Volume Averaging

The MATLAB computing language was used to implement the asymptotic homogenization analysis as described in the review papers by Hassani and Hinton [5],[39],[40], while the averaging analysis was implemented using MATLAB as described by Drago and Pindera [47]. The periodicity boundary conditions of homogenization were enforced using the constraint transformation method, while the boundary conditions of the volume averaging analysis were enforced using the method of Lagrange multipliers. (These methods are described in detail in Cook et al. [77]) Two different methods were implemented based on the compromise of simplicity of implementation, computational speed and necessity of setting zero and non-zero displacement constraints on individual nodes.

The two analysis methods were used to analyze the meta-material properties E_{ij}^M

in their intended manners: the analysis volume used for homogenization was a single RUC, while for the averaging analysis, the collection of UCs were averaged over. A two-dimensional isotropic base material with Young’s modulus $E = 30$ GPa and Poisson’s ratio $\nu = 0.30$ (under plane stress conditions) was modeled using four-node shell elements, as is commonly used in topology optimization. (The local material properties, i.e., those of the base material, may be isotropic, but for the non-homogeneous meta-material, the material properties will be, at best, orthotropic.) The codes were validated using the 20x20 element square domain with a rectangular hole found in [41] coinciding with or converging in the RVE limit to the homogenized meta-material properties. The codes were also validated using homogeneous orthotropic material properties. An ‘x’ topology and a ‘+’ topology were chosen as geometries to be used throughout the comparisons of the analyses. As discussed briefly in Chapter 1, these topologies are known periodic solutions to maximize shear and uniaxial stiffness in the design of composite structures [19].

3.1.1 $N \times N$ Unit Cell Analysis

In order to illustrate the $N \times N$ -cell convergence of the effective material properties resulting from these two geometries, UCs with 20x20 finite elements discretizations were chosen. For the both ‘x’ and ‘+’ geometries, the homogenized meta-material properties were determined. Next, the $N \times N$ analysis domains were constructed from both geometries with values of N from 1 to 8 (see Figure 3.2). For each value of N , the meta-material properties of the geometries were found using the displacement-based boundary conditions of the averaging analysis. This process was repeated for different thicknesses of bars constituting the meta-material from the minimum amount allowed by discretization to homogeneously-filled meta-material.

Plots comparing the meta-material properties are shown in Figures 3.3 and 3.4 for the ‘x’ geometries and Figures 3.5 and 3.6 for the ‘+’ geometries. (Only the E_{22}^U Young’s moduli were reported, as each solution is xy-symmetric, making the E_{33}^U moduli identical to the E_{22}^U moduli.) In these plots, the ratio of the meta-material modulus found using

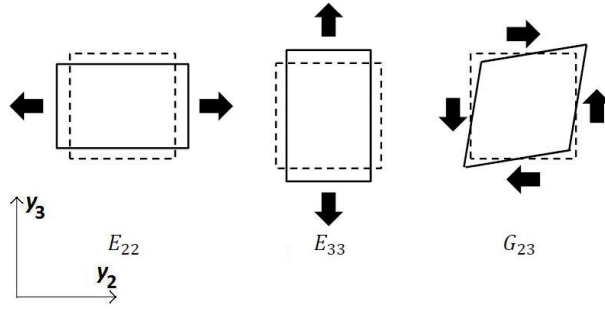


Figure 3.1: Three modes of deformation used in volume averaging and homogenization.

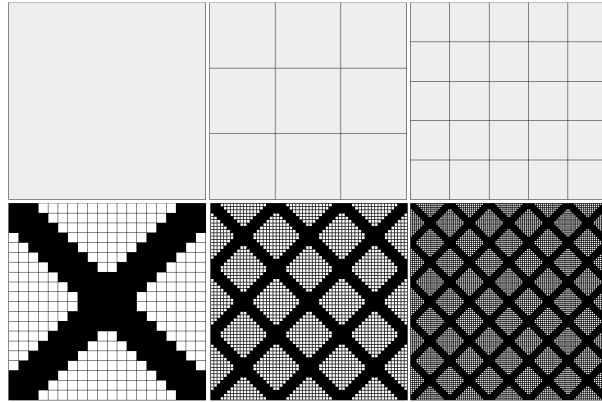


Figure 3.2: (Top) $N \times N$ analysis domains where, from left to right, $N = 1$, $N = 3$ and $N = 5$, respectively. All domains have the same total volume for averaging purposes. (Bottom) Example of domains filled with 'x' geometry.

composites methods to that of the homogenized meta-material modulus is plotted as a function of number of unit cells contained in the domain length, N . In each case, the homogenization approximation becomes increasingly appropriate with increasing N . Also, as the thicknesses of bars constituting the meta-material are increased, the geometries approach an isotropic material.

An interesting effect is noted in the distinct differences in these ratios for a single geometry. For the 'x' geometry, the shear moduli ratios rapidly converge to unity with increasing N , while the Young's moduli ratios demonstrate a very slow convergence (as seen by the scaling of the y-axes). A similar effect is seen for the '+' geometry in that the Young's moduli ratios rapidly converge to unity with increasing N , while the shear moduli ratios demonstrate a much slower convergence rate. This indicates that the design

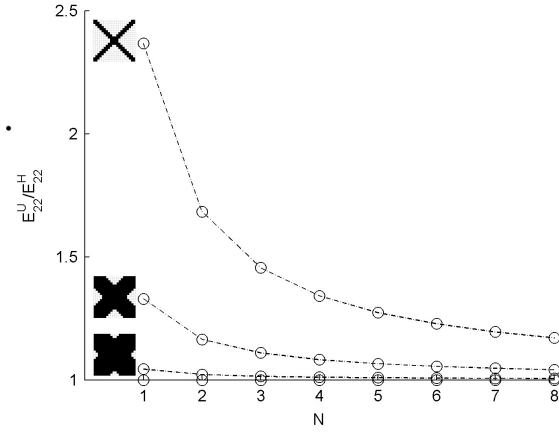


Figure 3.3: $N \times N$ analysis of meta-material Young's moduli E_{22}^U and E_{22}^H for the 'x' geometry.

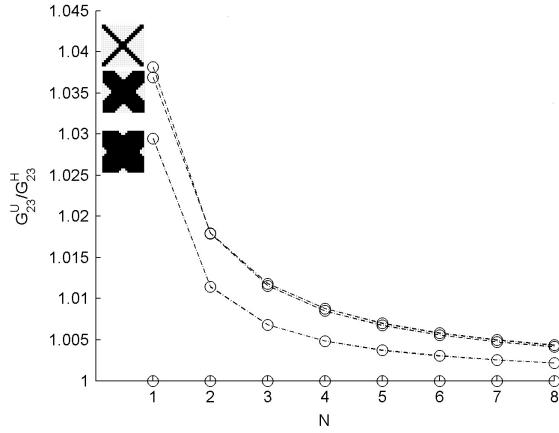


Figure 3.4: $N \times N$ analysis of meta-material shear moduli G_{23}^U and G_{23}^H for the 'x' geometry.

topology itself plays a key role in achieving the RVE limit. Thus, for global designs in which achievable solutions are below the RVE limit, i.e., small values of N , topology optimization by homogenization analysis may not be the best tool for determining an accurately-designed meta-material geometry. However, this same set of results stands as evidence that, in the RVE limit, homogenization is an accurate tool for meta-material analysis.

To investigate the mesh size effect in the $N \times N$ UC analysis, a single cell convergence test was completed for one of the 'x' designs and for one of the '+' designs. The discretization of the UC was increased sequentially along the length, while the overall widths of the constituting bars of the geometries were held constant (within discretization limits). The

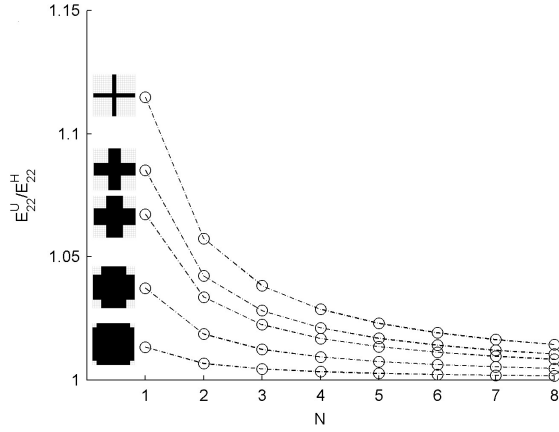


Figure 3.5: $N \times N$ analysis of meta-material Young's moduli E_{22}^U and E_{22}^H for the '+' geometry.

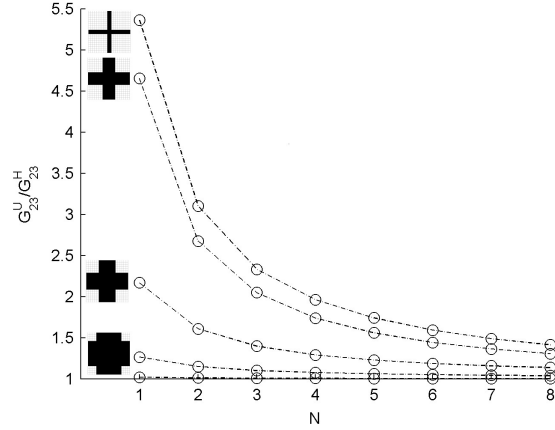


Figure 3.6: $N \times N$ analysis of meta-material shear moduli G_{23}^U and G_{23}^H for the '+' geometry.

homogenization and averaging analyses were run on each of the single UC problems over the different discretizations. (The UC was discretized from 10×10 finite elements to 40×40 finite elements, and the single-cell meta-material moduli were obtained.) Results comparing the ratios of averaged to homogenized moduli as a function of mesh size are shown in Figures 3.7 and 3.8.

In the case of the 'x' geometry, as the mesh size is reduced, the ratio of the averaged to homogenized moduli remains roughly constant, demonstrating that mesh size has little effect for that particular geometry. In the case of the '+' geometry, the same can be said

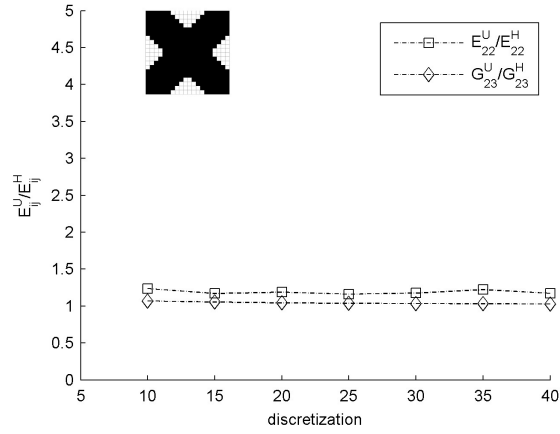


Figure 3.7: Finite element convergence analysis of ‘x’ geometry from 10x10 to 40x40 elements discretization.

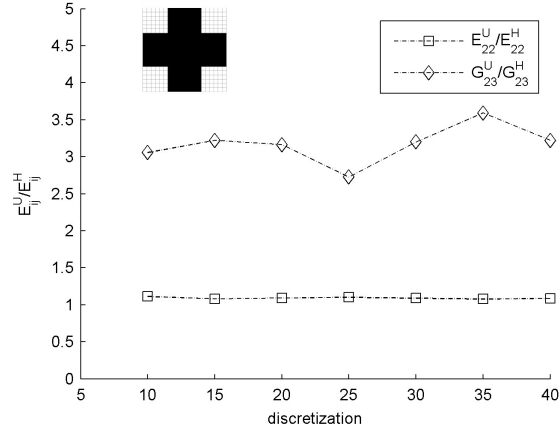


Figure 3.8: Finite element convergence analysis of ‘+’ geometry from 10x10 to 40x40 elements discretization.

about the effect of mesh size on the Young’s moduli. However, the total fluctuation in the shear moduli ratio is roughly 0.8. By referring back to Figure 3.6, for this particular problem the ratio of shear moduli for the 20x20 discretization is roughly 2.2. The discretization error can only account for 36% of the disparity between models, demonstrating that the mesh size can only be held partially responsible for the inconsistency in homogenized and averaged moduli for these particular examples. Instead, the previously mentioned inaccuracies in the physical assumptions of modeling are attributable.

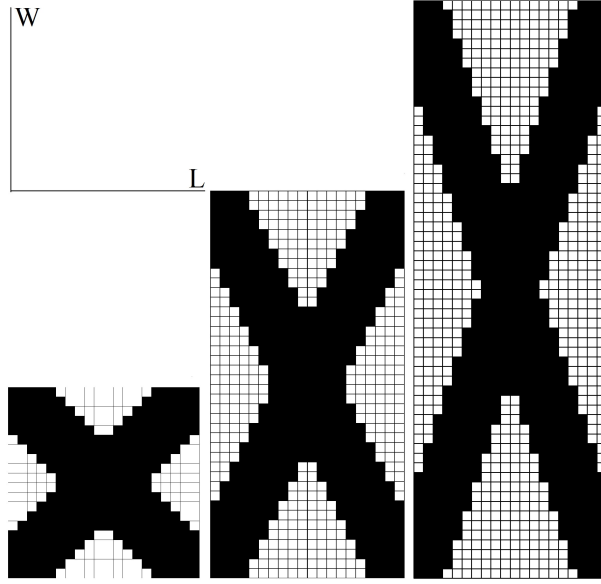


Figure 3.9: Similar unit cell geometries with different W/L scaling ratios.

3.1.2 Single, Rectangular Unit Cell Analysis

To demonstrate that homogenization analysis is no longer accurate under conditions that UC width to length ratios W/L are no longer unity, a set of analyses was completed comparing meta-material properties derived from both homogenization and composites analysis methods with the changing scale of W/L of the UC. In these numerical tests, the length L of the UC remained unchanged while the width W was varied between L and $3L$, meaning the total UC volume was varied between L^2 and $3L^2$ (see Figure 3.9).

As W was increased, more finite elements were added to the domain such that a single finite element contained the same amount of physical volume to eliminate variance of discretization errors attributable to element volume effects. Again, both the ‘x’ and ‘+’ geometries were tested, with the number of thicknesses of the each design’s bars held constant (within discretization limits) as the domain was made larger in width, W .

Results depicting the ratios of averaged to homogenized moduli as a function of domain width to length ratio are shown for the ‘x’ topology in Figures 3.10 and 3.11 and for the ‘+’ topology in Figure 37. (Bars of different thicknesses were used to investigate the effect the volume fraction on meta-material properties. Also, a discretization error is

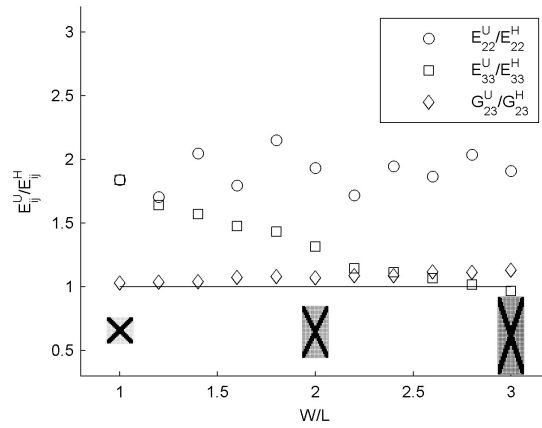


Figure 3.10: Meta-material properties as a function of W/L for single cell thin ‘x’ geometry.

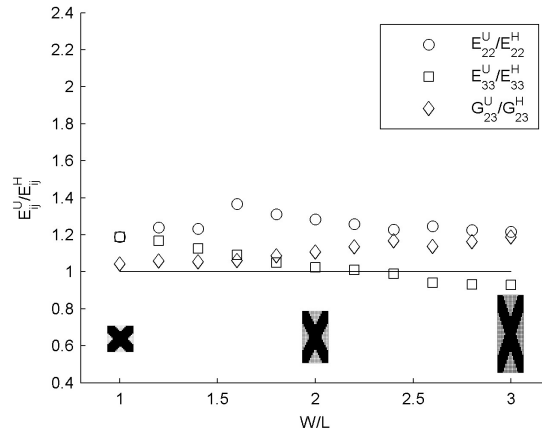


Figure 3.11: Meta-material properties as a function of W/L for single cell thick ‘x’ geometry.

present in the ‘x’ geometry results in which elements are not smoothly added as the UC is stretched from W/L equal 1 to W/L equal to 3. This is most clearly visible in the non-smooth behavior of the ratio of material properties for the thinner-barred ‘x’ geometry, top-left plot of Figure 36.)

From these single-cell results, it is clear that asymptotic homogenization theory and the composites averaging analysis do not predict the same meta-material moduli of a single cell in all cases. Even though the physical assumption is that homogenization is inaccurate, it cannot be assumed that the inaccuracy is with homogenization alone. This must be verified by looking at the homogeneous orthotropic materials with the homogenized moduli

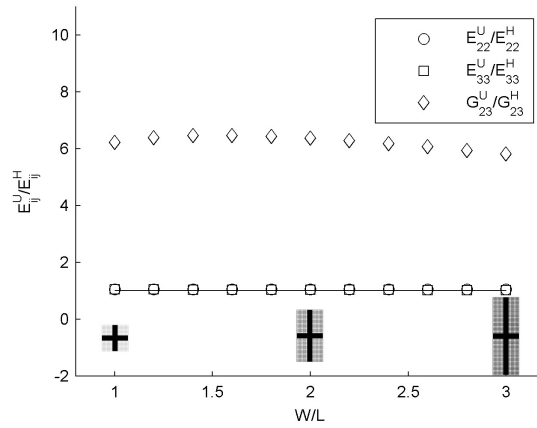


Figure 3.12: Meta-material properties as a function of W/L for single cell thin '+' geometry.

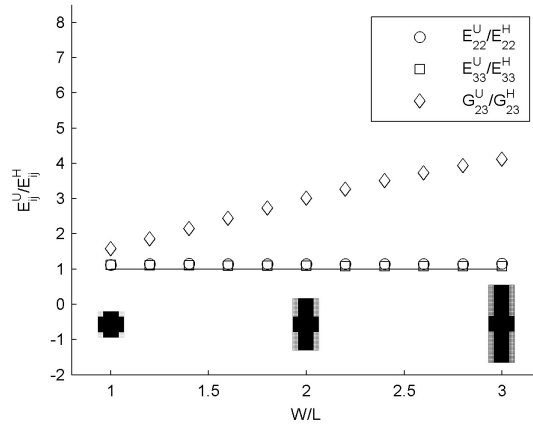


Figure 3.13: Meta-material properties as a function of W/L for single cell thick '+' geometry.

and averaged moduli values in a global model and comparing with the action of global model with the meta-material geometry. (Recalling the meta-material design procedure depicted in Figure 1.3, the meta-material is simulated as a homogenous orthotropic material during global optimization, but effective moduli are predicted at the meta-material design level. By inputting the geometry into the global-level simulation and comparing the effect of the model with the geometry to the effect of the global models with the homogenized moduli and averaged moduli, respectively, the accuracy of each of the models with respect to the global finite element problem can be evaluated. This is addressed in a latter section.)

However, several important observations should be noted. First, the relative con-

stancy of meta-material property ratios in Figures 3.10, 3.11 and 3.12 demonstrates a lack of dependence on the W/L ratios in those three cases, but in 3.13 there is a nearly linear dependence of the shear modulus on W/L . Also, in the case of the ‘x’ geometry, increasing the size of the bar thicknesses increases model agreement, but the same cannot be said for the ‘+’ geometry. As is the case for $N \times N$ analysis of the previous section, for ‘x’ geometries, the Young’s moduli do not coincide and the shear moduli do, and the shear moduli do not coincide for the ‘+’ geometry while the Young’s moduli do. As the width to length ratio is increased, the moduli undergo different trends. For example, the shear moduli remain relatively stable in the thin-barred ‘+’ geometry, while the shear moduli undergo a nearly-linear increase for the thick-barred ‘+’ geometry. However, no equivalent trend is noted for the ‘x’ geometries.

The question about the noise in the Young’s moduli of Figures 3.10 and 3.11 can be explained by the increasing discretization of the UC at each W/L step. The algorithm used to build the ‘x’ geometries draws a line from corner to corner of the UC, and then a Euclidean distance metric is used to choose elements to fill. As W/L is increased, a fluctuation of fewer and more cells within this inclusion distance. In these cases, while fluctuations about a constant value are apparent, the constant trend is of true physical note.

3.1.3 Single Layer Analysis

While Sec. 3.1.1 illustrated the different predictions of material properties using the two methods for square domains, these effects are also seen on single-layer domains. In this section, this divergence is explored on the extreme case of a single layer of unit cells. A single layer clearly violates the scaling assumption of homogenization theory. Again the comparison between the homogenized and averaging method can be analyzed by using both methods to compute material properties on a single layer of composite material.

In theory, the RVE limit could be reached by the averaging analysis while not necessarily requiring convergence to homogenized properties for a single layer, as the global

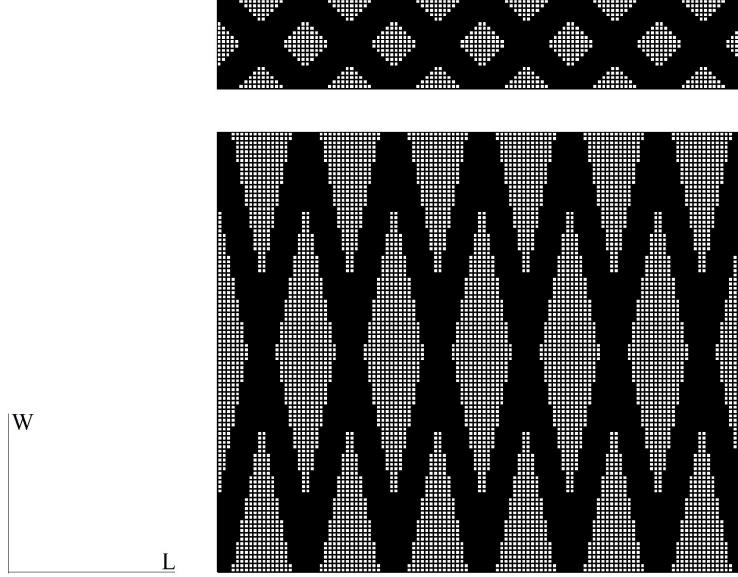


Figure 3.14: Single-layer materials with different W/L scaling ratios.

material scaling required by homogenization is violated. In addition, meta-material properties can be analyzed for non-square cells, but the relative scaling of the UC to the overall material changes in the process, possibly changing the accuracy of the meta-material property prediction when using homogenization or volume averaging. To test these hypotheses, homogenized properties for the same two ‘+’ and ‘x’ geometries were analyzed using a 20×20 element discretization for the UC with W/L fraction of one and a 20×100 discretization with W/L fraction of five (Figure 3.14). Then, the corresponding $N \times 1$ UC layers were analyzed using the averaging method in a manner similar to the $N \times N$ analyses. N was increased from one to fifteen incrementally in the same direction as the length L of the UC. Results for the ‘x’ geometry are shown in Figures 3.15 and 3.16, while typical results for the ‘+’ geometry are shown in Figures 3.17 and 3.18.

Again, the dependence of meta-material properties on design geometry is evident, as in all other cases. However, for the ‘x’ geometry, E_{22}^U does not converge to E_{22}^H , and the differences between these two values increases as W/L increases. In addition, convergence of G_{23}^U is G_{23}^H no longer achieved when W/L is increased. For the ‘+’ geometry, similar effects are noted in the convergence properties of G_{23}^U and G_{23}^H . Two distinct effects are

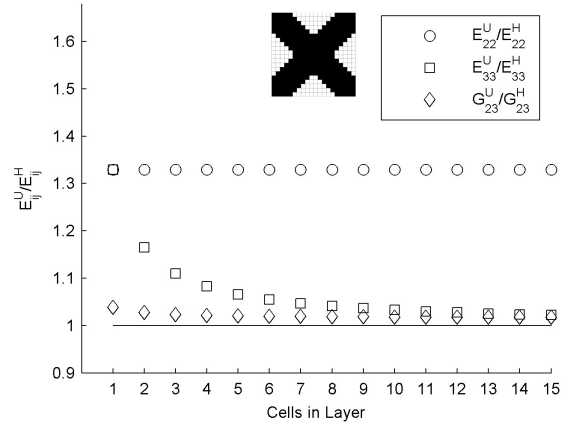


Figure 3.15: Comparative results for meta-material properties of a single layer of UCs for the ‘x’ geometry with W/L of the UC equal to one.

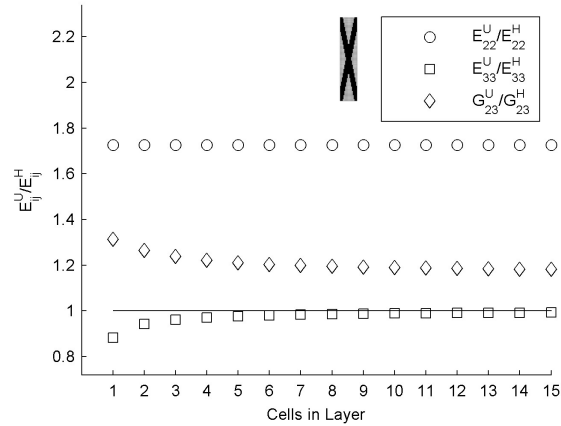


Figure 3.16: Comparative results for meta-material properties of a single layer of UCs for the ‘x’ geometry with W/L of the UC equal to five.

potentially at work here. For those layers with UCs with W/L equal to one, the global scaling assumption of homogenization is violated in one dimension, so there is no reason, even once the RVE limit has been achieved, to expect the averaging analysis to necessarily converge with the homogenization analysis. When W/L is increased to five, the single-parameter expansion of homogenization becomes invalid as well, amplifying the error of the homogenization analysis. While the homogenization analysis that uses a single-parameter expansion leads to what appear to be incorrect meta-material moduli, it is possible that a homogenization analysis obtained from a two-parameter expansion would produce correct

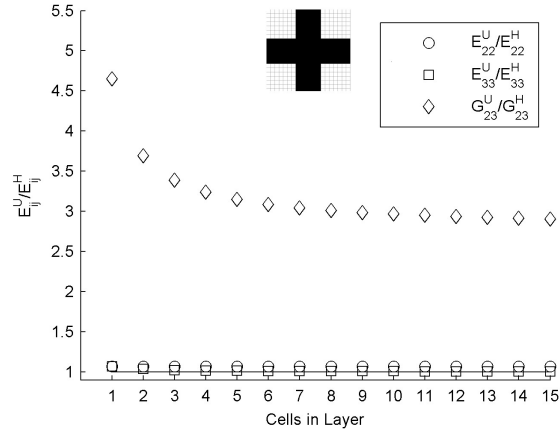


Figure 3.17: Comparative results for meta-material properties of a single layer of UCs for the ‘+’ geometry with W/L of the UC equal to one.

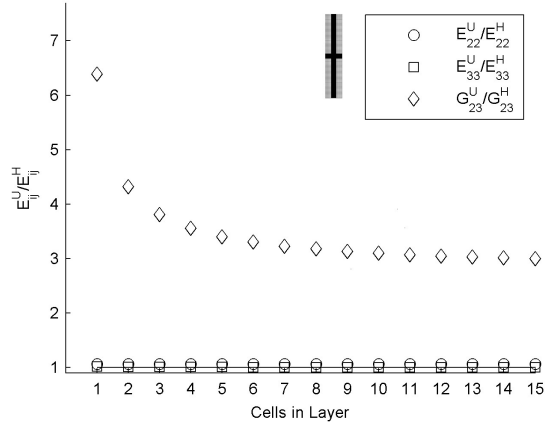


Figure 3.18: Comparative results for meta-material properties of a single layer of UCs for the ‘+’ geometry with W/L of the UC equal to five.

meta-material moduli.

Given these three different examples, the $N \times N$ analysis, the scaled UC analysis and the single-layer analysis, it is clear there are situations in which the two analytical models do not converge. However, what is not clear is which of the two methods, if either, is the numerically accurate method. The following section addresses this question with a simple meta-material design example.

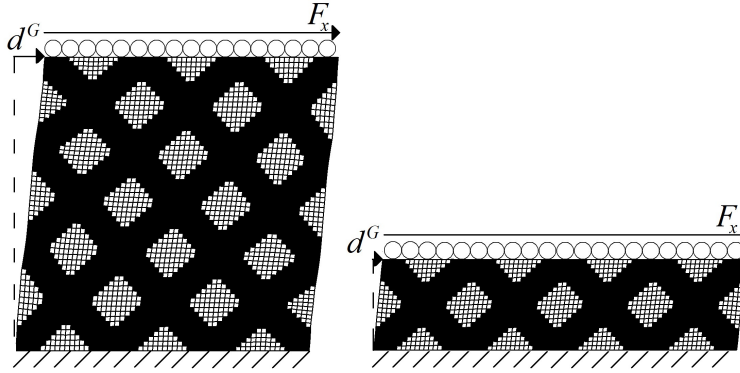


Figure 3.19: Loading conditions for simple shear design examples. The bottom nodes of each material are completely constrained, and the top nodes are constrained to displace only in the horizontal direction. A horizontal force F_x is placed on the top nodes, and the horizontal displacement d^G of the top is found as a result of the FEA.

3.2 Design Examples

Typically, the meta-material design process requires simulating the meta-material as part of the global design as a homogeneous orthotropic material with the properties given by the meta-material analysis, E_{ij}^M . However, if the analysis is inaccurate due to the violation of the scaling assumption, the meta-material may not perform in the manner intended when placed in the global design.

To demonstrate this point, three FEA problems were created in which materials were loaded in simple shear under traction boundary conditions, and displacements of the top edge were determined. First, the meta-material properties E_{ij}^M of a geometry were found using homogenization and averaging analyses. Then the material displacement d^G for the loading conditions of the global problem (as given in Figure 3.19) with the meta-material geometry was found, and the same boundary conditions were applied to a homogeneous, orthotropic material with meta-material properties E_{ij}^M to produce displacement d^M . This process, depicted in Figure 3.20, was completed using both the homogenization analysis and the composites averaging analysis. This was repeated for two different cases: one in which a square meta-material of constant volume was built out of $N \times N$ cells, just as in Sec. 3.1.1, and one in which the single-layer meta-material was built out of $N \times 1$ unit cells

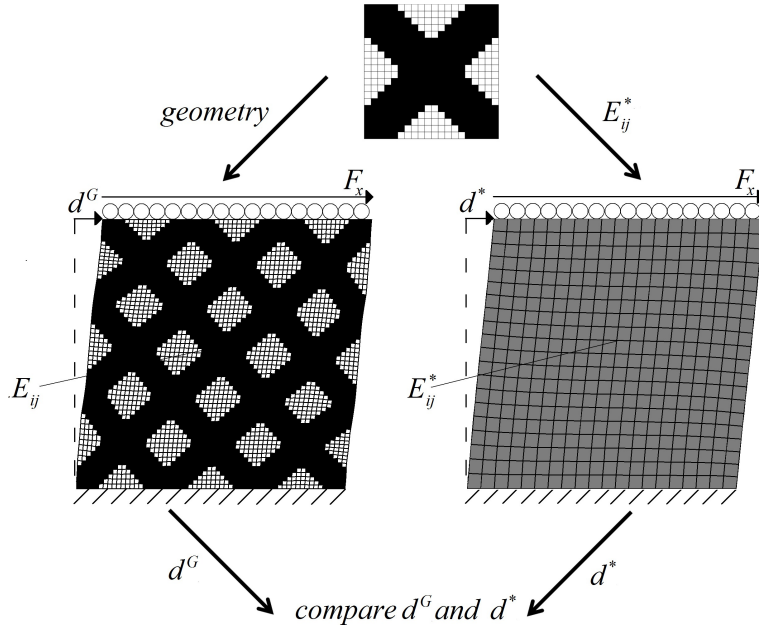


Figure 3.20: Depiction of the accuracy analysis of the meta-material design process in which the global displacement of the meta-material geometry was compared with that of the global displacement of the homogeneous, orthotropic material with properties E_{ij}^* using homogenization H or composites averaging U analyses.

with unit cell scaling W/L equal to one and W/L equal to five as in Sec. 3.1.3. (The same UC discretizations were used in each case.) For the $N \times N$, square meta-material, the relative errors of d^H and d^U from d^G are plotted as a function of N in Figures 3.21 and 3.22. Similarly, the relative errors are shown for the $N \times 1$ single-layer meta-material as a function of N in Figures 3.23, 3.24, 3.25 and 3.26. The results shown in Figures 3.21 and 3.22 for the $N \times N$ materials demonstrate a few important points. First, there is a design dependence on the convergence of the meta-materials properties to those approximated when below the RVE limit. However, in the RVE limit, the homogeneous, orthotropic material displacements appear to converge, albeit slowly in the case of the ‘+’ geometry, to those of the geometry displacements. For the single-layer materials (Figures 3.23, 3.24, 3.25 and 3.26), the results not only depict a strong convergence dependence on the meta-material design, but the displacements using the homogenized coefficients are inaccurate for all cases but one. For those geometries in which the displacements d^H are not consistent

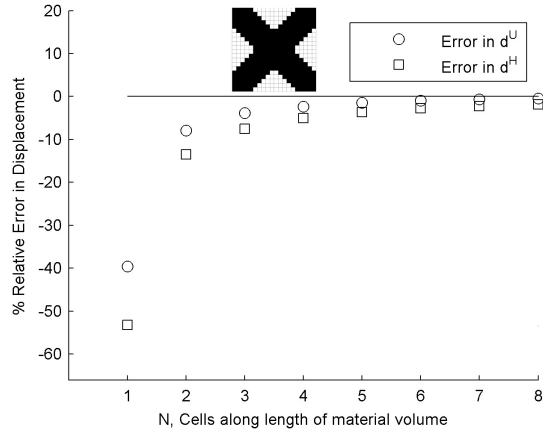


Figure 3.21: Relative errors of material displacements for square materials consisting of $N \times N$ unit cells ‘x’ geometry.

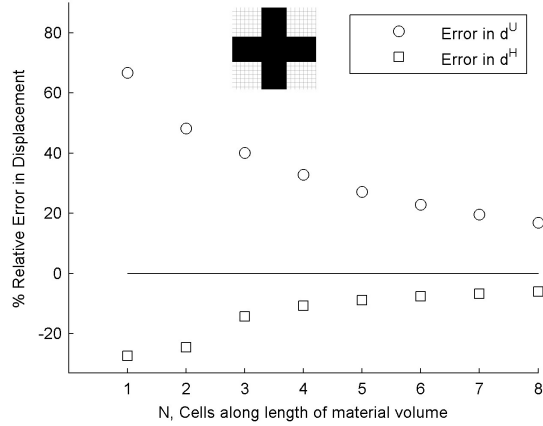


Figure 3.22: Relative errors of material displacements for square materials consisting of $N \times N$ unit cells ‘+’ geometry.

with geometry displacements d^G , the relative errors range between approximately 20% and 170%. However, in every case, the displacements predicted by the averaging analysis d^U agree with the geometry displacements d^G as the number of UCs in the meta-material layer is increased significantly. Also to note is an increase in relative error of convergence for this example when the W/L ratio is increased from one to five. The one case in which these designs are accurate is likely to be so because the same geometry that is optimal for pure shear (the ‘x’ geometry) is also local optimum in simple shear (the particular design example). However, the incorrect convergence in the other cases demonstrates the results

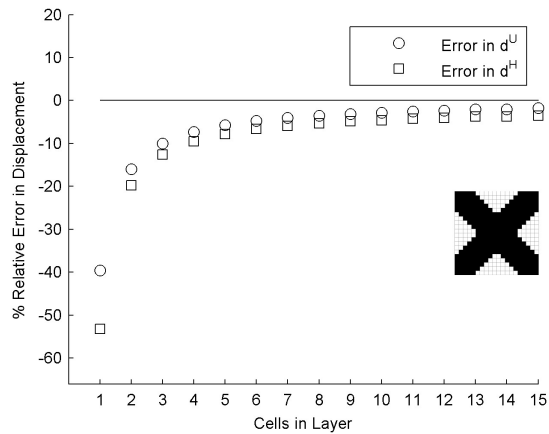


Figure 3.23: Relative errors of single-layer material displacements for ‘x’ geometry with W/L equal to one.

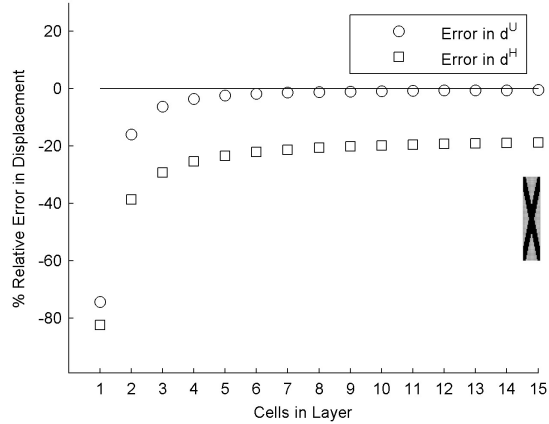


Figure 3.24: Relative errors of single-layer material displacements for ‘x’ geometry with W/L equal to five.

are sensitive to the topology and other geometry effects. In the case of the $N \times N$ and single-layered analyses, for this design example, the composite averaging analysis is accurate, while homogenization analysis is only accurate when the assumptions of homogenization are met.

One key point not to be overlooked from these results is that it appears that the RVE limit must be reached in every case in order for the global design parameters to be in agreement with the meta-material parameters. This negates the use of either homogenization or averaging analyses (as given here) as accurate methods when modeling below the RVE limit.

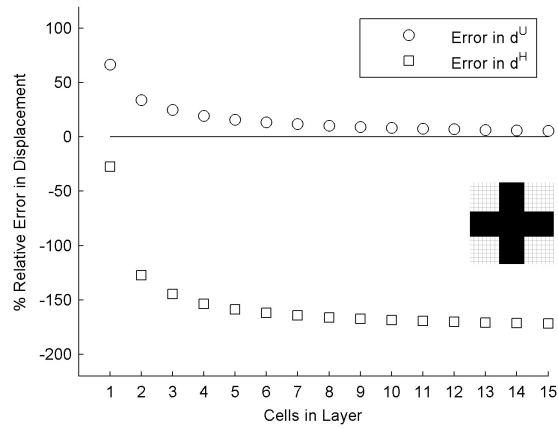


Figure 3.25: Relative errors of single-layer material displacements for ‘+’ geometry with W/L equal to one.

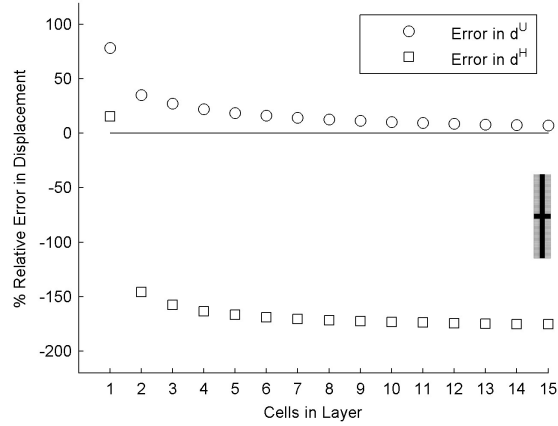


Figure 3.26: Relative errors of single-layer material displacements for ‘+’ geometry with W/L equal to five.

3.3 Summary

This chapter serves to clarify several important issues in the analysis of meta-materials for use in larger design assemblies. There are many cases in which the assumptions of asymptotic homogenization theory are not met. Given the results from these design examples, two different cases in which homogenization is inaccurate have been identified:

- when the small-parameter expansion is not valid
 - when the UC width to length ratio W/L is much larger than one such that the

unit cell is highly rectangular

- when the material scaling is such that the small-parameter expansion is no longer valid (i.e., single-layer materials).
- when too few cells are used to achieve the RVE limit (material design problems that include only a few UCs due to manufacturing constraints)

In the first case, volume averaging provides a better estimate of meta-material properties for use in the design optimization problem, while in the second case, neither analysis provides accurate meta-material moduli. However, when using a very small number of unit cells, other modeling methods that do not rely on meta-material parameters may be used. These methods that rely on only basic finite element modeling are outside the scope of meta-materials analysis and design and this body of research.

The scaling assumptions of homogenization are violated by creating single-layer composite meta-materials. By doing so, it becomes clear that the averaging analysis can predict with much greater fidelity the correct meta-material properties than the homogenization analysis that may be used in a homogeneous, orthotropic material in the global design. Also, loosening the square UC constraint to have non-unity W/L ratios opens up a wider range of design possibilities by adding another design parameter to the process to broaden the range of manufacturable meta-materials. (For example, longer, but not thinner, beams in shear result in a lower meta-material shear modulus without necessarily compromising manufacturability or yield properties.)

The strong dependence of these global convergence properties on meta-material design supports the need for topology optimization of the meta-material UC using the averaging analysis for those problems in which homogenization analysis is inaccurate, as the strength of a meta-material geometry is dependent on the placement, shape and size of voids introduced into the material. Without an accurate analytical tool, the meta-material will not necessarily perform as desired within the global assembly. However, below the RVE limit, there is not necessarily a gain in modeling fidelity by using the more computa-

tionally expensive averaging analysis over homogenization. While averaged meta-material properties E_{ij}^U may not converge rapidly to the homogenized properties E_{ij}^H , for the particular design of the square meta-material in simple shear, the displacements predicted by both homogenization and averaging converge to those of the geometry displacements. This supports the previous results of Drago and Pindera [47] and Pindera et al. [46] that homogenization analysis remains the most efficient method of meta-material analysis and optimization above the RVE limit for those meta-materials that meet the homogenization scaling assumptions.

The following chapters address the optimization tools needed for meta-material analysis in general, as well as the specifics of meta-material optimization using the volume averaging analysis. (As discussed in Chapter 2, optimization using asymptotic homogenization is well-studied for a number of design problems.)

Chapter 4

Optimality Conditions For Meta-Materials Topology Design Problems

In the design of meta-materials, two different types of design goals are typically used to target a property: a minimum amount of material used (weight or volume fraction) can be sought subject to satisfying the meta-material property E_k^* required (at a system level), or the 2-norm distance between the system requirement E_k^* and the meta-material property E_k can be minimized subject to weight or volume constraints. (Here, subscript $k \in \{22, 33, 23\}$ has been used instead of ij to simplify the notation.) The former method has been used with inverse homogenization analysis in the design of materials for specified linear elastic properties [20], [21], [78]. The latter method was described for linear elastic properties [40], [19], [79] and for thermal properties [80], and it was extended to the design of structures subject to multiple meta-material goals (stiffness and conduction) [81].

These methods seem similar in their basic approach, but there are subtle differences that can lead to difficulties in the implementation of the optimization methods when using continuous interpolations of the design space (e.g., solid isotropic microstructure with pe-

nalization, SIMP [54], [55]). For example, by targeting a desired material property while constraining the volume fraction, the design space can be limited such that the desired material property may no longer be feasible. Alternatively, when minimizing the volume fraction while constraining the difference between the desired property E_k^* and current property E_k , mathematical and numerical problems in the optimality conditions may arise, resulting in solutions that do not reach the targets or solutions are not suitable for material design. While the first example is common to all multicriteria optimization problems, the second example is specific to only those topology optimization problems that use continuous approximations to interpolate the design space. An argument could be made that using evolutionary algorithms could offer a solution to both of these problems, as they use 1-0 (inclusion-exclusion) methods to determine the finite elements to be included in an optimal structure (see, for example, Ling and Steven [82], Edwards et al. [83]). However, as pointed out in the review paper of Rozvany [71], these methods are computationally costly and non-deterministic in nature. Instead, it is common to implement SIMP or SIMP-like approximation methods that interpolate the density of each finite element on the continuous interval [0,1]: issues surrounding optimization and convergence of solutions are better understood, and deterministic algorithms can be used to easily solve a large number of topology optimization problems ([50], [52] and sources therein).

The purpose of this chapter is to examine the appropriate optimality conditions, either the Karush-Kuhn-Tucker (KKT) conditions or the more general Fritz-John (FJ) conditions, for the design of meta-materials with desired properties. First, the optimality conditions are stated for a general optimization problem, and the conditions are analyzed for three different optimization problems used to target multiple meta-material properties, and formulations are identified as either well-posed or ill-posed; in particular, the feasibility of 1-0 solutions at theoretical optimality when using continuous approximation methods is determined. Examples demonstrating these points using asymptotic homogenization with SIMP interpolation to determine the linear elastic properties of meta-materials (see, e.g., Hassani and Hinton [39] for a discussion of these techniques) are given and discussed in the

context of the different optimization formulations presented. Finally, a brief discussion of the utility of each of the optimization formulations summarizes the chapter.

4.1 Considered Optimization Problems

There are two functions of the density design variables \mathbf{x} (used to parameterize n finite elements of the design domain) in the topology optimization of meta-materials. The meta-material property $E_k(\mathbf{x})$ is obtained from some type of homogenization or other computational analysis, and the volume fraction $V(\mathbf{x})$ is defined as

$$V(\mathbf{x}) = \frac{1}{n} \sum_{j=1}^n x_j \quad (4.1)$$

The gradient of the volume fraction is given by

$$\nabla V(\mathbf{x}) = \frac{1}{n} \mathbf{u} \quad (4.2)$$

where $\mathbf{u} = (1, 1, \dots, 1)^T$ is a vector of ones with length n .

Let E_k^* denote the k th material design target desired for the meta-material design. Three different topology optimization formulations are considered. In the first problem, a minimum volume is desired subject to a linear constraint on k meta-material properties:

$$\begin{aligned} & \min_{\mathbf{x}} V(\mathbf{x}) & (4.3) \\ \text{s.t. } & h_k(\mathbf{x}) = E_k(\mathbf{x}) - E_k^* = 0 \text{ for } k \in \{1, 2, \dots, r\} \\ & g_i^1(x_i) = x_i - 1 \leq 0, \forall i \in \{1, 2, \dots, n\} \\ & g_i^2(x_i) = -x_i \leq 0, \forall i \in \{1, 2, \dots, n\} \end{aligned}$$

A constraint-relaxed version of Problem 4.3 is considered by changing the r linear equality

constraints into r quadratic inequality constraints:

$$\begin{aligned}
& \min_{\mathbf{x}} V(\mathbf{x}) & (4.4) \\
& \text{s.t. } g_i^1(x_i) = x_i - 1 \leq 0, \forall i \in \{1, 2, \dots, n\} \\
& g_i^2(x_i) = -x_i \leq 0, \forall i \in \{1, 2, \dots, n\} \\
& g_k^3(\mathbf{x}) = (E_k(\mathbf{x}) - E_k^*)^2 - \delta_k \leq 0 \text{ for } k \in \{1, 2, \dots, r\}
\end{aligned}$$

where δ_k is an engineering tolerance for material objective k . The final problem considered is the formulation in which the quadratic difference between objective and target is minimized subject to volume fraction constraints:

$$\begin{aligned}
& \min_{\mathbf{x}} \sum_{k=1}^r w_k (E_k(\mathbf{x}) - E_k^*)^2 & (4.5) \\
& \text{s.t. } g_i^1(x_i) = x_i - 1 \leq 0, \forall i \in \{1, 2, \dots, n\} \\
& g_i^2(x_i) = -x_i \leq 0, \forall i \in \{1, 2, \dots, n\} \\
& g_U^3(\mathbf{x}) = V(\mathbf{x}) - V_U \leq 0 \\
& g_L^4(\mathbf{x}) = V_L - V(\mathbf{x}) \leq 0
\end{aligned}$$

In these problems, constraints g_i^1 and g_i^2 are those boundary constraints on design variables x_i that become necessary when interpolating the design variables on the continuous interval $[0,1]$. In the next section, the optimality conditions for each of these problems are derived and discussed in detail without regard to a specific engineering application beyond meta-material design or material interpolation method.

4.2 Optimality Conditions

The optimality conditions considered are those conditions that must necessarily hold for a point to be a local optimum of an optimization problem. The Karush-Kuhn-Tucker (KKT) equations are those that express the mathematically necessary conditions for a

constrained optimization problem at optimal point \mathbf{x}^* . (See, for example, Bertsekas [84], Horst et al. [85], or Bazaraa et al. [86].) These conditions only apply if \mathbf{x}^* is a regular point, meaning that the gradients of the equality constraints and the active inequality constraints are linearly independent at \mathbf{x}^* . In each of the considered problems, it is assumed that point \mathbf{x}^* is a regular point, unless otherwise stated, and the KKT conditions are considered. When \mathbf{x}^* is shown to be no-longer regular, the weaker Fritz-John (FJ) necessary conditions are considered.

4.2.1 Minimizing Volume With Linear Material Constraints

The KKT conditions for Problem (4.3) consist of the stationarity condition

$$\nabla V(\mathbf{x}^*)^T + \sum_k \mu_k \nabla(E_k(\mathbf{x}^*) - E_k^*)^T + \sum_i \lambda_i^U \nabla(x_i^* - 1)^T + \sum_i \lambda_i^L \nabla(-x_i^*)^T = \bar{\mathbf{0}} \quad (4.6)$$

primal feasibility

$$h_k(\mathbf{x}^*) = 0, \quad g_i^1(x_i^* - 1) \leq 0, \quad g_i^2(x_i^*) \leq 0, \quad \forall i \in 1, 2, \dots, n \quad (4.7)$$

dual feasibility

$$\lambda_i^U \geq 0, \quad \lambda_i^L \geq 0, \quad \forall i \in 1, 2, \dots, n \quad (4.8)$$

and complementary slackness

$$\lambda_i^U (x_i^* - 1) = 0, \quad \lambda_i^L (-x_i^*) = 0, \quad \forall i \in 1, 2, \dots, n \quad (4.9)$$

Here, μ_k denotes the Lagrange multipliers associated with material equality constraint h_k , and there are up to n non-zero Lagrange multipliers λ_i^U and λ_i^L for the bounds on design variables x_i .

Using Eq. (4.2), the stationarity condition Eq. (4.6) can be written as

$$\frac{1}{n} \mathbf{u} + \sum_k \mu_k (\nabla E_k(\mathbf{x}^*))^T + \mathbf{R}^U \lambda^U + \mathbf{R}^L \lambda^L = \bar{\mathbf{0}} \quad (4.10)$$

where

$$\mathbf{R}^U = [\hat{\mathbf{e}}_{1U}^T, \hat{\mathbf{e}}_{2U}^T, \dots, \hat{\mathbf{e}}_{pU}^T], \mathbf{R}^L = [\hat{\mathbf{e}}_{1L}^T, \hat{\mathbf{e}}_{2L}^T, \dots, \hat{\mathbf{e}}_{qL}^T], \quad (4.11)$$

are matrices containing unit vectors $\hat{\mathbf{e}} = (0, 0, \dots, 1, \dots, 0)$ for only the p and q active upper and lower boundary constraints. Here, $\mu = (\mu_1, \mu_2, \dots, \mu_r)^T$, and $\lambda^U = (\lambda_1^U, \lambda_2^U, \dots, \lambda_p^U)^T$ and $\lambda^L = (-\lambda_1^L, -\lambda_2^L, \dots, -\lambda_q^L)^T$ are vectors of the Lagrange multipliers for only the active constraints. (The minus sign introduced by the gradient of active lower bounds has been included in the vector λ^L .) By writing $\overline{\nabla E} = [\nabla E_1^T, \nabla E_2^T, \dots, \nabla E_r^T]$, $\lambda = ((\lambda^U)^T, (\lambda^L)^T)^T$ and $\mathbf{R} = [\mathbf{R}^U \ \mathbf{R}^L]$, Eq. (4.10) can be written as the system of linear equations

$$-n [\overline{\nabla E} \ \mathbf{R}] \begin{bmatrix} \mu \\ \lambda \end{bmatrix} = \mathbf{u} \quad (4.12)$$

At optimality, the p columns of \mathbf{R}^U are all linearly independent, as are the q columns of \mathbf{R}^L , and $\text{span}(\mathbf{R}^U) \cap \text{span}(\mathbf{R}^L) = \emptyset$. Given Eq. (4.12), and assuming all material constraints h_k have been met, there are three different cases to consider at optimality.

Case 1 $r + p + q < n$: In this case, there are more rows than columns in linear system 4.12. The rows of $[\overline{\nabla E} \ \mathbf{R}]$ can be rearranged such that

$$-n \begin{bmatrix} \overline{\nabla E}_N \ \mathbf{0} \\ \overline{\nabla E}_A \ \mathbf{I} \end{bmatrix} \begin{bmatrix} \mu \\ \lambda \end{bmatrix} = \mathbf{u} = \begin{bmatrix} \mathbf{u}_N \\ \mathbf{u}_A \end{bmatrix} \quad (4.13)$$

where A and N denote those design variables that are or are not on the boundaries, respectively, $\mathbf{0}$ is a matrix of zeros and \mathbf{I} is the identity matrix, u_N^T is a vector of ones with length $n - p - q$ and u_A^T is a vector of ones with length $p + q$.

Let l and m denote the subscripts for design variables with and without active boundary constraints, respectively. Equation m from system 4.13 for the set of design variables not on a boundary is written

$$\sum_{k=1}^r \frac{\partial E_k}{\partial x_m} \mu_k = -\frac{1}{n} \quad (4.14)$$

while equation l from system 4.13 for the set of design variables on a boundary is written

$$\sum_{k=1}^r \frac{\partial E_k}{\partial x_l} \mu_k \pm \lambda_l^{U,L} = -\frac{1}{n} \quad (4.15)$$

(The term $\pm \lambda_l^{U,L}$ is positive if the upper boundary constraint is active and negative if the lower boundary constraint is active.) Since conditions (4.8) must be satisfied, by labeling subscript $l = a$ for active lower boundary constraints and $l = b$ for active upper boundary constraints, rearranging Eq. (4.15) gives

$$\sum_{k=1}^r \frac{\partial E_k}{\partial x_a} \mu_k \leq -\frac{1}{n} \quad (4.16)$$

$$\sum_{k=1}^r \frac{\partial E_k}{\partial x_b} \mu_k \geq -\frac{1}{n} \quad (4.17)$$

Combining Eqs. (4.14), (4.16) and (4.17)

$$\sum_{k=1}^r \frac{\partial E_k}{\partial x_a} \mu_k \leq \sum_{k=1}^r \frac{\partial E_k}{\partial x_m} \mu_k \leq \sum_{k=1}^r \frac{\partial E_k}{\partial x_b} \mu_k, \quad \forall a \neq b \neq m \quad (4.18)$$

Thus, the KKT conditions are satisfied for system (4.13) provided that Eq. (4.18) holds.

Case 2 $r + p + q = n$: In this case, the matrix $[\overline{\nabla E} \mathbf{R}]$ is square, $\det(\overline{\nabla E} \mathbf{R}) \neq 0$, and the optimal point \mathbf{x}^* is regular. Therefore, there exists a unique solution to Eq. (4.12). The KKT conditions hold if Eq. (4.18) is satisfied.

If $\det(\overline{\nabla E} \mathbf{R}) = 0$, the matrix $[\overline{\nabla E} \mathbf{R}]$ contains linearly dependent columns. The

regularity assumption at point \mathbf{x}^* is no longer valid, and the FJ conditions must be considered. In this case, the stationarity equation of the FJ conditions will have a vanishing multiplier in front of the gradient of the objective, reducing the condition to

$$\sum_k \mu_k \nabla(E_k(\mathbf{x}^*) - E_k^*)^T + \sum_i \lambda_i^U \nabla(x_i^* - 1)^T + \sum_i \lambda_i^L \nabla(-x_i^*)^T = \bar{0} \quad (4.19)$$

where

$$(\mu, \lambda) \neq \bar{0} \quad (4.20)$$

The dual feasibility conditions Eq. (4.8) still apply, and, because the constraints are all differentiable, the slackness conditions Eq. (4.9) still hold. Using the same previously defined terms, the stationarity requirement Eq. (4.19) can be written

$$[\overline{\nabla E} \ \mathbf{R}] \begin{bmatrix} \mu \\ \lambda \end{bmatrix} = \bar{0} \quad (4.21)$$

The linear dependence of the columns of $[\overline{\nabla E} \ \mathbf{R}]$ implies there are an infinite number of solutions to system (4.21). A similar argument to Case 1 can be made for the inactive and active constraints to give

$$\sum_{k=1}^r \frac{\partial E_k}{\partial x_m} \mu_k = 0 \quad (4.22)$$

$$\sum_{k=1}^r \frac{\partial E_k}{\partial x_a} \mu_k \leq 0 \quad (4.23)$$

$$\sum_{k=1}^r \frac{\partial E_k}{\partial x_b} \mu_k \geq 0 \quad (4.24)$$

which, once again, produces the result

$$\sum_{k=1}^r \frac{\partial E_k}{\partial x_a} \mu_k \leq \sum_{k=1}^r \frac{\partial E_k}{\partial x_m} \mu_k \leq \sum_{k=1}^r \frac{\partial E_k}{\partial x_b} \mu_k, \quad \forall a \neq b \neq m \quad (4.25)$$

Thus, the FJ conditions are satisfied provided that Eqs. (4.20), (4.21) and (4.25) hold.

Case 3 $r + p + q > n$: There are, at most, n independent columns in matrix $[\overline{\nabla E} \mathbf{R}]$. Matrix $[\overline{\nabla E} \mathbf{R}]$ again contains linearly dependent columns, and the FJ conditions must be considered instead. The same argument as in Case 2 can be made, where Eqs. (4.20), (4.21) and (4.25) must apply for the FJ conditions to hold. Given that Cases 1, 2 and 3 satisfy either the KKT conditions or the weaker FJ conditions at optimal point \mathbf{x}^* , and provided that all material properties E_k^* can be achieved at optimality, there always exists an optimal solution to Problem (4.3).

4.2.2 Minimizing Volume With Quadratic Material Constraints

The KKT conditions for Problem (4.4) include the stationarity condition

$$\begin{aligned} \nabla V(\mathbf{x}^*)^T + \sum_k \lambda_k \nabla((E_k(\mathbf{x}^*) - E_k^*)^2 - \delta_k)^T \\ + \sum_i \lambda_i^U \nabla(x_i^* - 1)^T + \sum_i \lambda_i^L \nabla(-x_i^*)^T = \bar{\mathbf{0}} \end{aligned} \quad (4.26)$$

primal feasibility

$$g_i^1(x_i^* - 1) \leq 0, \quad g_i^2(x_i^*) \leq 0, \quad \forall i \in 1, 2, \dots, n, \quad g_k^3(\mathbf{x}^*) \leq 0, \quad \forall k \in 1, 2, \dots, r \quad (4.27)$$

dual feasibility

$$\lambda_i^U \geq 0, \quad \lambda_i^L \geq 0, \quad \forall i \in 1, 2, \dots, n, \quad \lambda_k \geq 0, \quad \forall k \in 1, 2, \dots, r \quad (4.28)$$

and complementary slackness

$$\begin{aligned} \lambda_i^U (x_i^* - 1) = 0, \quad \lambda_i^L (-x_i^*) = 0, \quad \forall i \in 1, 2, \dots, n \\ \lambda_k ((E_k(\mathbf{x}^*) - E_k^*)^2 - \delta_k) = 0, \quad \forall k \in 1, 2, \dots, r \end{aligned} \quad (4.29)$$

λ_k denotes the Lagrange multiplier for the material inequality constraints g_k^3 , and λ_i^U and λ_i^L denote the Lagrange multipliers for the bounds on the design variables x_i , where there are up to n active boundary constraints. The stationarity condition 4.26 can be written in a manner similar to Eq. (4.10) for the linearly constrained problem by using the same definitions for \mathbf{R}^U , \mathbf{R}^L , λ^U and λ^L :

$$\frac{1}{n} \mathbf{u} + \sum_k 2\lambda_k (E_k(\mathbf{x}^*) - E_k^*) \nabla E_k(\mathbf{x}^*)^T + \mathbf{R}^U \lambda^U + \mathbf{R}^L \lambda^L = \bar{\mathbf{0}} \quad (4.30)$$

In Eq. (4.30), the matrix of gradients $\overline{\nabla E}$ takes the form

$$\overline{\nabla E} = [2(E_k(\mathbf{x}^*) - E_k^*) \nabla E_1, \dots, 2(E_r^M(\mathbf{x}^*) - E_r^*) \nabla E_r] \quad (4.31)$$

If all material constraints g_k^3 are active at optimality, the primal feasibility conditions (4.27) can be written

$$(E_k(\mathbf{x}^*) - E_k^*) = \pm \sqrt{\delta_k} \quad \forall k \in 1, 2, \dots, r \quad (4.32)$$

if all constraints on the material properties have been met. Thus, the matrix of gradients in Eq. (4.31) has the form

$$\overline{\nabla E} = [\pm 2\sqrt{\delta_1} \nabla E_1, \pm 2\sqrt{\delta_2} \nabla E_2, \dots, \pm 2\sqrt{\delta_r} \nabla E_r] \quad (4.33)$$

By writing $\lambda = (\lambda_1, \lambda_2, \dots, \lambda_r)^T$, $\lambda_C = ((\lambda^U)^T, (\lambda^L)^T)^T$ and $\mathbf{R} = [\mathbf{R}^U \ \mathbf{R}^L]$, Eq. (4.30) can be written

$$-n[\overline{\nabla E} \ \mathbf{R}] \begin{bmatrix} \lambda \\ \lambda_C \end{bmatrix} = \mathbf{u} \quad (4.34)$$

First, assume $\delta_k = 0$ for all k . The gradient matrix $\overline{\nabla E}$ vanishes, and \mathbf{x}^* is no longer regular. The FJ conditions must be considered, and they read

$$\sum_k \lambda_k \nabla ((E_k(\mathbf{x}^*) - E_k^*)^2 - \delta_k)^T + \sum_i \lambda_i^U \nabla (x_i^* - 1)^T + \sum_i \lambda_i^L \nabla (-x_i^*)^T = \bar{\mathbf{0}} \quad (4.35)$$

$$(\lambda, \lambda_C) \neq \bar{0} \quad (4.36)$$

with $\delta_k = 0$. Additionally, the primal feasibility, dual feasibility and slackness conditions, Eqs. (4.27), (4.28) and (4.29) still apply. Given Eq. (4.35), it is clear that, similar to Problem (4.3), the FJ conditions simply introduce a zero vector onto the right hand side of the linear system:

$$[\mathbf{0} \quad \mathbf{R}] \begin{bmatrix} \lambda \\ \lambda_C \end{bmatrix} = \bar{0} \quad (4.37)$$

Dividing through by $-n$ and rearranging the terms with active and inactive boundary constraints, system (4.37) is written

$$\begin{bmatrix} \mathbf{0} & \mathbf{0} \\ \mathbf{0} & \mathbf{I} \end{bmatrix} \begin{bmatrix} \lambda \\ \lambda_C \end{bmatrix} = \bar{0} \quad (4.38)$$

The top equations in system (4.38) imply λ_k are free for all values of k , while the equations in the bottom of system (4.38) imply $\lambda_l^{U,L} = 0$ for all active constraints l . Thus, in this case, there exists an infinite number of solutions to system (4.38) with degenerate constraints on the design variables. Though these solutions satisfy the FJ necessary conditions, Eqs. (4.27) - (4.29) and Eqs. (4.35) and (4.36), the degeneracy of all of the boundary constraints has implications on the convergence of the design variables to a 1-0 solution.

Now assume there is at least one $\delta_k \neq 0$. There are three cases to consider.

Case 1 $r + p + q < n$: This case is similar to the same case as that for Problem (4.3), but now the equations for design variables with inactive boundary constraints lead to the conditions

$$2 \sum_{k=1}^r \pm \sqrt{\delta_k} \frac{\partial E_k}{\partial x_m} \lambda_k = -\frac{1}{n} \quad (4.39)$$

while for those equations with design variables on upper and lower boundary constraints,

$$2 \sum_{k=1}^r \pm \sqrt{\delta_k} \frac{\partial E_k}{\partial x_a} \lambda_k \leq -\frac{1}{n} \quad (4.40)$$

$$2 \sum_{k=1}^r \pm \sqrt{\delta_k} \frac{\partial E_k}{\partial x_b} \lambda_k \geq -\frac{1}{n} \quad (4.41)$$

Combining Eqs. (4.39) - (4.41) yields

$$\sum_{k=1}^r \pm \sqrt{\delta_k} \frac{\partial E_k}{\partial x_a} \lambda_k \leq \sum_{k=1}^r \pm \sqrt{\delta_k} \frac{\partial E_k}{\partial x_m} \lambda_k \leq \sum_{k=1}^r \pm \sqrt{\delta_k} \frac{\partial E_k}{\partial x_b} \lambda_k, \quad \forall m \neq a \neq b \quad (4.42)$$

Thus, if there exists a $\delta_k \neq 0$, system (4.34) has a solution, and the KKT conditions hold provided that Eq. (4.42) is satisfied.

Case 2 $r + p + q = n$: Again, in this case, the matrix $[\overline{\nabla E} \ \mathbf{R}]$ is square. Since there is a $\delta_k \neq 0$ for at least one k , similar to Problem (4.3), there exists a unique solution to Eq. (4.34) provided $\det(\overline{\nabla E} \ \mathbf{R}) \neq 0$. If Eq. (4.42) is satisfied, the KKT conditions hold.

If $\det(\overline{\nabla E} \ \mathbf{R}) = 0$, the regularity assumption at point \mathbf{x}^* is no longer valid, and the FJ conditions must be considered. Eqs. (4.35) and (4.36) apply, where Eq. (4.35) can be written as the linear system

$$[\overline{\nabla E} \ \mathbf{R}] \begin{bmatrix} \lambda \\ \lambda_C \end{bmatrix} = \bar{0} \quad (4.43)$$

A similar argument to Case 1 for Problem (4.4) is made to give

$$\sum_{k=1}^r \pm \sqrt{\delta_k} \frac{\partial E_k}{\partial x_m} \lambda_k = 0 \quad (4.44)$$

$$\sum_{k=1}^r \pm \sqrt{\delta_k} \frac{\partial E_k}{\partial x_a} \lambda_k \leq 0 \quad (4.45)$$

$$\sum_{k=1}^r \pm \sqrt{\delta_k} \frac{\partial E_k}{\partial x_b} \lambda_k \geq 0 \quad (4.46)$$

Combining Eqs. (4.44), (4.45) and (4.46) results in the condition

$$\sum_{k=1}^r \pm \sqrt{\delta_k} \frac{\partial E_k}{\partial x_a} \lambda_k \leq \sum_{k=1}^r \pm \sqrt{\delta_k} \frac{\partial E_k}{\partial x_m} \lambda_k \leq \sum_{k=1}^r \pm \sqrt{\delta_k} \frac{\partial E_k}{\partial x_b} \lambda_k, \quad \forall m \neq a \neq b \quad (4.47)$$

The vanishing determinant of matrix $[\overline{\nabla E} \quad \mathbf{R}]$ implies an infinite number of solutions to system (4.43) exists. Provided that Eqs. (4.36) and (4.47) are satisfied, the FJ conditions hold at optimal point \mathbf{x}^* .

Case 3 $r + p + q > n$: Again, there are, at most, n independent columns, and the FJ conditions must be considered. The same logic as Case 2 applies, where system (4.43) has an infinite number of solutions. Provided that Eqs. (4.36) and (4.47) are satisfied, the FJ conditions hold.

Thus, for Problem (4.4), an optimal solution exists for $\delta_k \neq 0$. If $\delta_k = 0$ for all k , the optimal solution of Problem (4.4) satisfies the optimality conditions. However, all of the constraints on the design variable boundaries are degenerate, where all of the Lagrange multipliers are zero. The consequences on the application of this formulation to design engineering are presented in Section 4.4.

4.2.3 Minimizing the Material Objective with Volume Constraints

The KKT conditions for Problem (4.5) include the stationarity condition

$$\sum_k w_k \nabla((E_k(\mathbf{x}^*) - E_k^*)^2)^T \pm \lambda_V^{U,L} \nabla V(\mathbf{x}^*)^T + \sum_i \lambda_i^U \nabla(x_i^* - 1)^T + \sum_i \lambda_i^L \nabla(-x_i^*)^T = \bar{\mathbf{0}} \quad (4.48)$$

primal feasibility

$$g_i^1(x_i^* - 1) \leq 0, \quad g_i^2(x_i^*) \leq 0, \quad \forall i \in 1, 2, \dots, n, \quad g_U^3(\mathbf{x}^*) \leq 0, \quad g_L^4(\mathbf{x}^*) \leq 0, \quad \forall k \in 1, 2, \dots, r \quad (4.49)$$

dual feasibility

$$\lambda_i^U \geq 0, \quad \lambda_i^L \geq 0, \quad \forall i \in 1, 2, \dots, n, \quad \lambda_V^{U,L} \geq 0 \quad (4.50)$$

and complementary slackness

$$\lambda_i^U(x_i^* - 1) = 0, \quad \lambda_i^L(-x_i^*) = 0, \quad \forall i \in 1, 2, \dots, n, \quad \lambda_V^{U,L}V(\mathbf{x}^*) = 0 \quad (4.51)$$

Here, $\lambda_V^{U,L}$ is the Lagrange multiplier for the active upper (U) or lower (L) volume constraint; either one volume constraint or neither may be active, but not both simultaneously. By using the same definitions for \mathbf{R}^U , \mathbf{R}^L , λ^U and λ^L as previously employed, the stationarity condition, Eq. (4.48), can be written

$$\begin{bmatrix} \frac{\mathbf{u}}{n} & \mathbf{R}^U & \mathbf{R}^L \end{bmatrix} \begin{bmatrix} \lambda_V^{U,L} \\ \lambda^U \\ \lambda^L \end{bmatrix} = - \sum_{k=1}^r 2w_k(E_k(\mathbf{x}^*) - E_k^*)\overline{\nabla E_k}(\mathbf{x}^*) \quad (4.52)$$

For system (4.52), if a volume constraint is active, there are two cases to consider, while there is only one case to consider if neither volume constraint is active:

Case 1 $p + q < n$ with active volume constraint: By rearranging the rows of matrix $\begin{bmatrix} \frac{\mathbf{u}}{n} & \mathbf{R}^U & \mathbf{R}^L \end{bmatrix}$ and multiplying by n , Eq. (4.52) for this case is written

$$\begin{bmatrix} \mathbf{u}_N & \mathbf{0} \\ \mathbf{u}_A & n\mathbf{I} \end{bmatrix} \begin{bmatrix} \lambda_V^{U,L} \\ \lambda^U \\ \lambda^L \end{bmatrix} = -n \sum_{k=1}^r 2w_k(E_k(\mathbf{x}^*) - E_k^*)\overline{\nabla E_k}(\mathbf{x}^*) \quad (4.53)$$

where \mathbf{u}_N and \mathbf{u}_A denote vectors of ones for inactive and active boundary constraints, respectively. If all material objectives are met, $E_k(\mathbf{x}^*) - E_k^* = 0$, and the right hand side of

Eq. (4.53) vanishes. The linear system reads

$$\begin{bmatrix} \mathbf{u}_N & \mathbf{0} \\ \mathbf{u}_A & n\mathbf{I} \end{bmatrix} \begin{bmatrix} \lambda_V^{U,L} \\ \lambda^U \\ \lambda^L \end{bmatrix} = \bar{\mathbf{0}} \quad (4.54)$$

Any equation from the top part of the constraint matrix in system (4.54)

$$\lambda_V^{U,L} = 0 \quad (4.55)$$

while the equations for the active constraints are

$$\lambda_V^{U,L} \pm \lambda_l^{U,L} = 0, \quad \forall l \in 1, 2, \dots, p+q \quad (4.56)$$

Combining Eqs. (4.55) and (4.56) yields

$$\lambda_l^{U,L} = 0, \quad \forall l \in 1, 2, \dots, p+q \quad (4.57)$$

This implies, at optimality, system (4.52) has a trivial solution, as all Lagrange multipliers vanish. However, the KKT conditions are satisfied.

If only t material objectives are met ($1 \leq t < r$), then Eq. (4.53) becomes

$$\begin{bmatrix} \mathbf{u}_N & \mathbf{0} \\ \mathbf{u}_A & n\mathbf{I} \end{bmatrix} \begin{bmatrix} \lambda_V^{U,L} \\ \lambda^U \\ \lambda^L \end{bmatrix} = -n \sum_{k=1}^t 2w_k (E_k(\mathbf{x}^*) - E_k^*) \overline{\nabla E_k}(\mathbf{x}^*) \quad (4.58)$$

The m th row in the upper portion of this linear system reads

$$\lambda_V^{U,L} = -n \sum_{k=1}^t 2w_k (E_k(\mathbf{x}^*) - E_k^*) \frac{\partial E_k}{\partial x_m} \quad (4.59)$$

while the l th row in the lower portion reads

$$\lambda_V^{U,L} \pm n\lambda_l^{U,L} = -n \sum_{k=1}^t 2w_k(E_k(\mathbf{x}^*) - E_k^*) \frac{\partial E_k}{\partial x_l} \quad (4.60)$$

Combining Eqs. (4.59) and (4.60) and rearranging gives

$$\pm \lambda_l^{U,L} = - \sum_{k=1}^t 2w_k(E_k(\mathbf{x}^*) - E_k^*) \frac{\partial E_k}{\partial x_l} - \sum_{k=1}^t 2w_k(E_k(\mathbf{x}^*) - E_k^*) \frac{\partial E_k}{\partial x_m}, \quad l \neq m \quad (4.61)$$

The dual feasibility conditions (4.50) require

$$- \sum_{k=1}^t 2w_k(E_k(\mathbf{x}^*) - E_k^*) \frac{\partial E_k}{\partial x_m} \geq 0, \quad \forall m \quad (4.62)$$

$$\sum_{k=1}^t 2w_k(E_k(\mathbf{x}^*) - E_k^*) \frac{\partial E_k}{\partial x_a} \geq - \sum_{k=1}^t 2w_k(E_k(\mathbf{x}^*) - E_k^*) \frac{\partial E_k}{\partial x_m}, \quad \forall m \neq a \quad (4.63)$$

and

$$\sum_{k=1}^t 2w_k(E_k(\mathbf{x}^*) - E_k^*) \frac{\partial E_k}{\partial x_b} \leq - \sum_{k=1}^t 2w_k(E_k(\mathbf{x}^*) - E_k^*) \frac{\partial E_k}{\partial x_m}, \quad \forall m \neq b \quad (4.64)$$

where subscripts a and b denote variables on active lower and upper boundaries, as before.

Combining Eqs. (4.63) and (4.64) gives

$$\begin{aligned} \sum_{k=1}^t 2w_k(E_k(\mathbf{x}^*) - E_k^*) \frac{\partial E_k}{\partial x_b} &\leq - \sum_{k=1}^t 2w_k(E_k(\mathbf{x}^*) - E_k^*) \frac{\partial E_k}{\partial x_m} \\ &\leq \sum_{k=1}^t 2w_k(E_k(\mathbf{x}^*) - E_k^*) \frac{\partial E_k}{\partial x_a}, \quad \forall m \neq a \neq b \end{aligned} \quad (4.65)$$

Thus, in this case that t material constraints are not satisfied, system (4.58) has a solution provided that Eqs. (4.62) and (4.65) hold.

Case 2 $p + q = n$ with active volume constraint: In this case, system (4.52) takes the form

$$[\mathbf{u}_A \ n\mathbf{I}] \begin{bmatrix} \lambda_V^{U,L} \\ \lambda^U \\ \lambda^L \end{bmatrix} = -n \sum_{k=1}^r 2w_k (E_k(\mathbf{x}^*) - E_k^*) \overline{\nabla E_k}(\mathbf{x}^*) \quad (4.66)$$

There are $n + 1$ columns and n rows in matrix $[\mathbf{u}_A \ n\mathbf{I}]$. The columns of this matrix are linearly dependent, and the FJ conditions must be applied. The stationarity condition reads

$$\pm \lambda_V^{U,L} \nabla V(\mathbf{x}^*)^T + \sum_i \lambda_i^U \nabla (x_i^* - 1)^T + \sum_i \lambda_i^L \nabla (-x_i^*)^T = \bar{0} \quad (4.67)$$

where

$$(\lambda_V^{U,L}, \lambda) \neq \bar{0} \quad (4.68)$$

Additionally, primal feasibility, dual feasibility and complementary slackness, Eqs. (4.49), (4.50) and (4.51) still apply. Eq. (4.67) can be written

$$[\mathbf{u}_A n\mathbf{I}] \begin{bmatrix} \lambda_V^{U,L} \\ \lambda^U \\ \lambda^L \end{bmatrix} = \bar{0} \quad (4.69)$$

An equation from system (4.69) reads

$$\lambda_V^{U,L} \pm n\lambda_l^{U,L} = 0 \quad (4.70)$$

Dual feasibility requires Lagrange multipliers $\lambda_V^{U,L}$ and $\lambda_l^{U,L}$ be non-negative. Thus, the only solution to Eq. (4.70) is $(\lambda_V^{U,L}, \lambda) = \bar{0}$, contradicting Eq. (4.68), and the FJ conditions for this case do not hold.

Case 3 Neither volume constraint is active: Here, the Lagrange multiplier $\lambda_V^{U,L}$ vanishes, and Eq. (4.52) takes the form

$$\begin{bmatrix} \mathbf{0} \\ n\mathbf{I} \end{bmatrix} \begin{bmatrix} \lambda^U \\ \lambda^L \end{bmatrix} = -n \sum_{k=1}^r 2w_k(E_k(\mathbf{x}^*) - E_k^*) \nabla E_k(\mathbf{x}^*) \quad (4.71)$$

where λ^U and λ^L are vectors of Lagrange multipliers for the active boundary constraints. If all r material requirements are met, the right hand side of Eq. (4.71) vanishes, and the only solution is $\lambda_l^{U,L} = 0$ for all l , so that a trivial solution to linear system (4.71) is obtained. However, if only t material requirements are not met ($1 \leq t < r$), the right hand side of Eq. (4.71) no longer vanishes, and an equation from this system reads

$$\pm n \lambda_l^{U,L} = -n \sum_{k=1}^t 2w_k(E_k(\mathbf{x}^*) - E_k^*) \frac{\partial E_k}{\partial x_l} \quad (4.72)$$

The dual feasibility conditions (4.50) require in this case

$$\sum_{k=1}^t 2w_k(E_k(\mathbf{x}^*) - E_k^*) \frac{\partial E_k}{\partial x_b} \leq 0 \leq \sum_{k=1}^t 2w_k(E_k(\mathbf{x}^*) - E_k^*) \frac{\partial E_k}{\partial x_a}, \quad \forall a \neq b \quad (4.73)$$

Here, system (4.71) has a non-trivial solution, and the KKT conditions hold provided that Eq. (4.73) is satisfied.

Thus, for Problem (4.5), all of the formulations in which a volume constraint is active have only trivial solutions for the Lagrange multipliers of the linear systems associated with the stationarity conditions of the KKT conditions, implying all of the constraints are degenerate. The same is true when a volume constraint is not active and all of the material requirements are met. However, when one or more of the material requirements for this case is not met, it is possible to find a feasible, non-trivial, optimal solution \mathbf{x}^* .

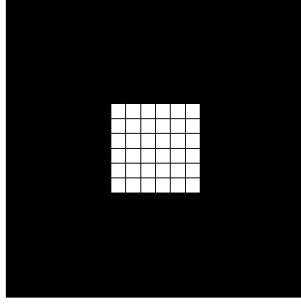


Figure 4.1: Initial point used for optimization.

4.3 Design Examples Using Homogenization

Given the mathematical analyses of these three problems, a few design examples are used to demonstrate the mathematical and design capabilities of each optimization method to target only a single meta-material property. To do this, asymptotic homogenization was used to analyze either the Young's modulus $E_{22}^H(\mathbf{x})$ or the shear modulus $G_{23}^H(\mathbf{x})$ of the material. The same design domain discretizations (20x20 square, shell elements) and termination parameters (1000 function evaluations, 200 iterations, material modulus tolerance equal to 10^{-3} and volume fraction tolerance equal to 10^{-4}) were used. At this discretization, there were 400 design variables. The linear equality constrained Problem (3) has no additional parameters, while the quadratic constrained Problem (4.4) has been optimized with both zero and non-zero values for δ , and different ranges of volume fraction boundaries were used for the volume fraction constrained Problem (4.5).

The initial point used for all optimizations, a material with a square hole, is shown in Figure 4.1. A linear, elastic material with Young's modulus $E_0 = 30$ GPa and Poisson's ratio $\nu = 0.30$ under a plane stress condition was used for the finite element analysis. For the optimization, the SIMP interpolation with penalization exponent $s = 3$ such that the effective Young's modulus E_i of element i was given by

$$E_i = E_0 x_i^s \tag{4.74}$$

A mesh filter, similar to that reported by Sigmund [28] was used to eliminate numeri-

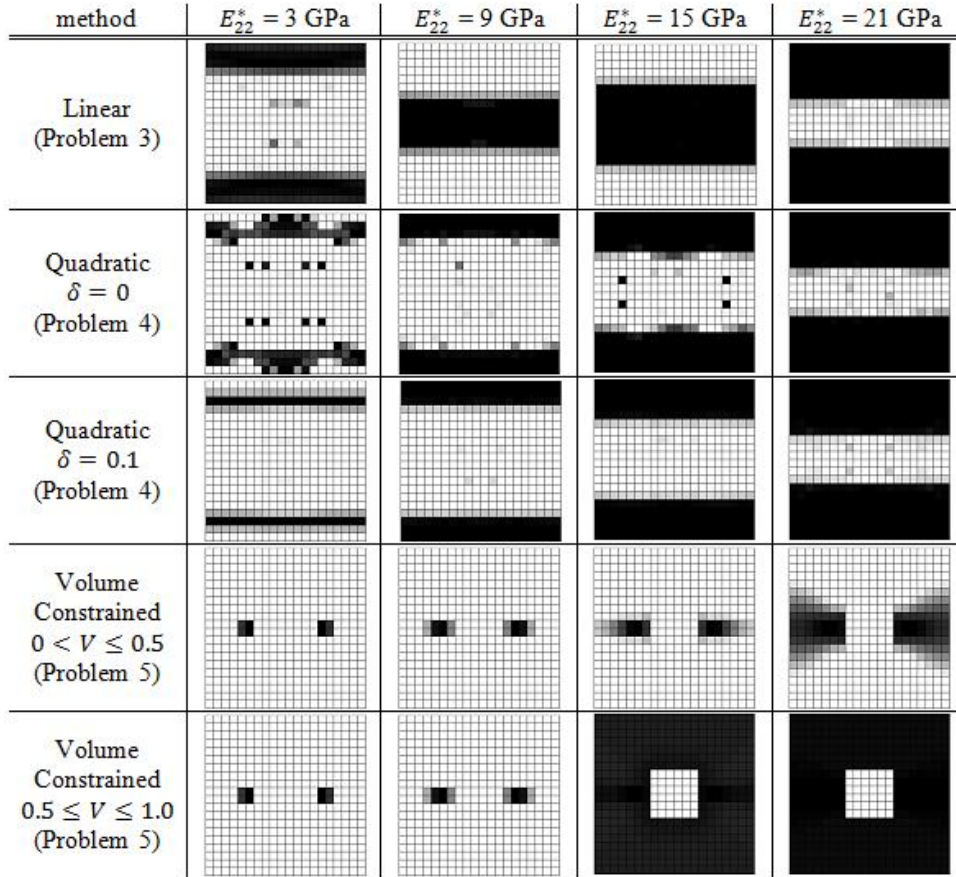


Figure 4.2: Visual results for optimizations targeting different Young’s moduli E_{22}^* . Numerical results are given in Table 4.1.

cal problems common to topology optimization of continuous design domains, including checkerboard solutions and one-node connected hinges. (See Sigmund and Petersson [66] and sources therein for a discussion of these issues.) The results for optimization of the Young’s modulus are given in Figure 4.2 and in Table 4.1, while results for optimization of the shear modulus are given in Figure 4.3 and Table 4.2. For optimization using Problem (4.4), $\delta = 0$ and $\delta = 0.1$ were chosen, while for optimization using Problem (4.5), the feasible volume fractions were constrained such that either $V \in (0,0.5]$ or $V \in [0.5,1]$. The number of active constraints on the finite elements is listed as a numerical verification of SIMP convergence of the final solution. The numerical results in Tables 4.1 and 4.2 share several common results. First, the linearly constrained optimization method, Problem (4.3),

Table 4.1: Numerical Results For Optimizations Targeting E_{22}^*

Linear (Problem 4.3)					
E_{22}^* [GPa]	E_{22}^H [GPa]	V	Iterations	Func. Eval.	Active Constraints
3	3.001	0.256	85	452	172
9	9.001	0.336	60	194	314
15	14.999	0.552	109	290	378
21	21.001	0.718	72	214	302
Quadratic, $\delta = 0$ (Problem 4.4)					
E_{22}^* [GPa]	E_{22}^H [GPa]	V	Iterations	Func. Eval.	Active Constraints
3	1.892 [†]	0.209	234	1001	183
9	8.708 [†]	0.315	248	1001	161
15	15.001	0.542	229	747	309
21	20.980 [†]	0.721	207	1001	331
Quadratic, $\delta = 0.1$ (Problem 4.4)					
E_{22}^* [GPa]	E_{22}^H [GPa]	V	Iterations	Func. Eval.	Active Constraints
3	2.645	0.151	175	1001	192
9	8.688	0.319	86	199	260
15	14.637 [†]	0.515	144	1001	113
21	20.487 [†]	0.710	114	1001	148
Volume Constrained, $0 < V \leq 0.5$ (Problem 4.5)					
E_{22}^* [GPa]	E_{22}^H [GPa]	V	Iterations	Func. Eval.	Active Constraints
3	0.000 [‡]	0.005	2	3	392
9	0.000 [‡]	0.014	2	3	394
15	12.704 [‡]	0.743	3	34	36
21	19.664 [‡]	0.863	2	29	36
Volume Constrained, $0.5 \leq V \leq 1.0$ (Problem 4.5)					
E_{22}^* [GPa]	E_{22}^H [GPa]	V	Iterations	Func. Eval.	Active Constraints
3	0.000 [‡]	0.005	2	3	392
9	0.000 [‡]	0.014	2	3	384
15	0.000 [‡]	0.036	2	3	352
21	0.000 [‡]	0.163	2	3	272

[†] Optimization terminated early by exceeding allowed number of function evaluations.

[‡] Optimization terminated early due to inability to find a feasible solution.

Table 4.2: Numerical Results For Optimizations Targeting E_{22}^*

Linear (Problem 4.3)					
G_{23}^* [GPa]	G_{23}^H [GPa]	V	Iterations	Func. Eval.	Active Constraints
1	1.001	0.420	36	144	14
4	4.000	0.546	122	380	177
5	5.000	0.650	109	418	187
7	7.001	0.813	72	418	272
Quadratic, $\delta = 0$ (Problem 4.4)					
G_{23}^* [GPa]	G_{23}^H [GPa]	V	Iterations	Func. Eval.	Active Constraints
1	0.944 [†]	0.348	194	1001	26
4	4.001	0.652	66	238	38
5	4.999	0.718	51	211	40
7	6.952 [†]	0.824	114	1001	233
Quadratic, $\delta = 0.1$ (Problem 4.4)					
G_{23}^* [GPa]	G_{23}^H [GPa]	V	Iterations	Func. Eval.	Active Constraints
1	0.684	0.308	132	750	40
4	3.680 [†]	0.561	167	1001	92
5	4.674 [†]	0.627	140	1001	106
7	6.678 [†]	0.786	139	1001	236
Volume Constrained, $0 < V \leq 0.5$ (Problem 4.5)					
G_{23}^* [GPa]	G_{23}^H [GPa]	V	Iterations	Func. Eval.	Active Constraints
1	0.000 [‡]	0.269	2	3	192
4	0.173 [‡]	0.467	3	28	44
5	1.665 [‡]	0.500	176	542	164
7	1.561 [‡]	0.500	344	1001	0
Volume Constrained, $0.5 \leq V \leq 1.0$ (Problem 4.5)					
G_{23}^* [GPa]	G_{23}^H [GPa]	V	Iterations	Func. Eval.	Active Constraints
1	0.000 [‡]	0.269	2	3	192
4	2.945 [‡]	0.720	3	31	36
5	4.282 [‡]	0.783	3	30	36
7	6.931 [‡]	0.882	3	23	36

[†] Optimization terminated early by exceeding allowed number of function evaluations.

[‡] Optimization terminated early due to inability to find a feasible solution.

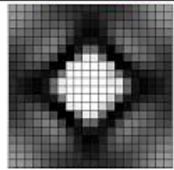
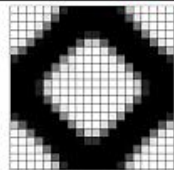
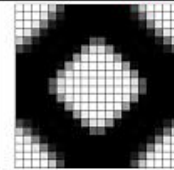
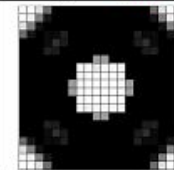
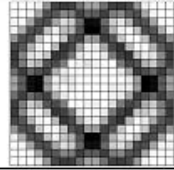
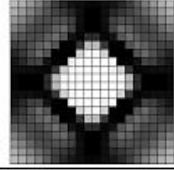
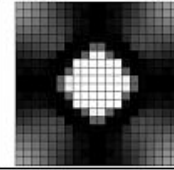
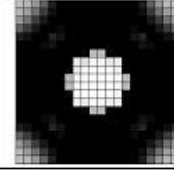
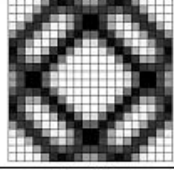
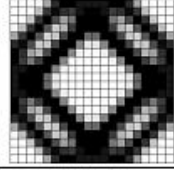
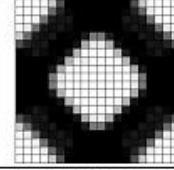
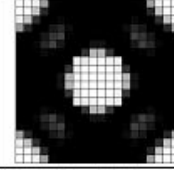
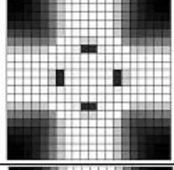
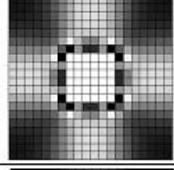
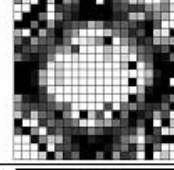
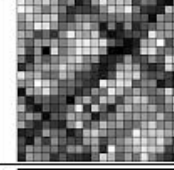
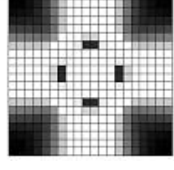
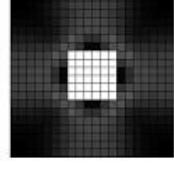
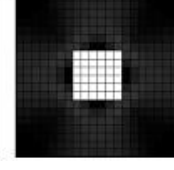
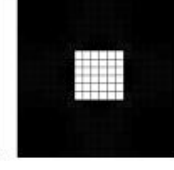
method	$G_{23}^* = 1 \text{ GPa}$	$G_{23}^* = 4 \text{ GPa}$	$G_{23}^* = 5 \text{ GPa}$	$G_{23}^* = 7 \text{ GPa}$
Linear (Problem 3)				
Quadratic $\delta = 0$ (Problem 4)				
Quadratic $\delta = 0.1$ (Problem 4)				
Volume Constrained $0 < V \leq 0.5$ (Problem 5)				
Volume Constrained $0.5 \leq V \leq 1.0$ (Problem 5)				

Figure 4.3: Visual results for optimizations targeting different Young’s moduli G_{23}^* . Numerical results are given in Table 4.2.

was successful in achieving the desired moduli E_{22}^* and G_{23}^* , numerically, with the fewest number of algorithm iterations and function evaluations. The optimizations with quadratic constraints on the material moduli had mixed results, where the use of the engineering tolerance δ in Problem (4.4) resulted in a larger range of allowable moduli upon successful termination of the optimization algorithm; many of the optimizations terminated prematurely, reaching the maximum allowed number of function evaluations when using quadratic material constraints for both zero and non-zero δ . None of the volume constrained optimizations achieved the desired moduli, as the optimization algorithm was unable to reach a feasible point. By comparing the $G_{23}^* = 1 \text{ GPa}$ or $E_{22}^* = 3 \text{ GPa}$ optimization attempts for the volume constrained method with volume fraction constrained to be less than 0.5

with the linearly constrained attempts with similar targets, it is clear that feasible, local optima existed for the volume constrained attempts. Similar results are true by looking at the larger moduli optimization attempts. Finally, In each of the optimization attempts, there are fewer active boundary constraints than total number of design variables. The visual results presented in Figures 4.2 and 4.3 support the numerical results. For the optimizations targeting E_{22}^* with linear material constraints and quadratic material constraints with non-zero δ , each of the solutions are bar-like geometries with few intermediate densities, whereas $\delta = 0$ optimizations resulted in somewhat blurry solutions with intermediate densities (best demonstrated in the $E_{22}^* = 3$ GPa case). The G_{23}^* optimizations showed similar convergence, or lack thereof, for these three optimization methods. In the volume constrained solutions, the solutions lack a distinguishable geometry, being at a numerical lower bound of the optimization, or they have not moved in an appreciable way from the initial point.

4.4 Discussion

The results of the mathematical evaluation of the optimality conditions are summarized in Table 4.3. From these results, it is clear that, when attempting to target a number of material properties in a meta-material design problem, a problem formulation using linear constraints as in Problem (4.3) can be used. For a topology optimization problem that utilizes any continuous material interpolation method, achieving a 1-0 solution implies that all of the design variables are on one boundary or another. It is shown here that there are infinitely many solutions to the problem due to the existence of an underdetermined linear system at optimality. However, with the need to use some filtering method to eliminate checkerboard solutions, the number of design variables is typically greater than the number of active boundary and material property constraints. This is because the mesh-filtering scheme introduces a common situation in which intermediate design densities are obtained. This case was shown to lead to the overdetermined system of linear equations in Section

4.2.1. The design examples presented in Section 4.3 support these conclusions, since all of the optimization attempts were numerically successful, but only one was not visually well-resolved.

Table 4.3: Summary of Mathematical Analysis of Optimality Conditions

Problem 3	Conditions Satisfied
$r + p + q < n$	KKT
$r + p + q = n$	KKT ^a , FJ ^b
$r + p + q > n$	FJ
Problem 4	Conditions Satisfied
$\delta k = 0 \forall k$	Neither
$\exists k$ such that $\delta_k \neq 0, r + p + q < n$	KKT
$\exists k$ such that $\delta_k \neq 0, r + p + q = n$	KKT ^a , FJ ^b
$\exists k$ such that $\delta_k \neq 0, r + p + q > n$	FJ
Problem 5	Conditions Satisfied
$p + q < n$, active volume constraint, all material requirements met	KKT [†]
$p + q < n$, active volume constraint, one or more material requirements not met	KKT
$p + q = n$, active volume constraint	Neither
Neither volume constraint active, all material requirements met	KKT [†]
Neither volume constraint active, one or more material requirements not met	KKT

[†] Boundary constraints are degenerate. ^a Non-zero determinant of constraint matrix.

^b Zero determinant of constraint matrix .

In the case of the constraint-relaxed Problem (4.4) using quadratic constraints on the material properties, the problem formulation was shown to admit only the trivial solution for the Lagrange multipliers for the exact design of material properties in meta-material topology design ($\delta_k = 0 \forall k$). Vanishing Lagrange multipliers using quadratic constraints are noted elsewhere; in particular, Alexandrov and Lewis note the use of quadratic equality constraints in collaborative optimization of systems results in vanishing Lagrange multipliers do not exist at optimality [87]. In Problem (4.4), the zero Lagrange multipliers associated with boundary constraints imply that all of these constraints are degenerate at optimality;

the constraints could be removed from the optimization problem and the same point would be obtained as optimal. This is an issue because, while the material requirements will be met, the notion that every one of these boundary constraints on the design variables does not affect the quality of the solution is obviously contrary to the purpose of topology optimization for which 1-0 solutions are desired. These conclusions are demonstrated with the design examples given in Section 4.3, as the optimizations where $\delta = 0$ resulted in geometries that had many intermediate densities in the design domain. These solutions are not suitable for material design.

However, when a non-zero value for δ_k in Problem (4.4) was chosen, the optimization problem was shown to be theoretically well-posed, and the visual results in Section 4.3 display well-resolved geometries similar to the linearly constrained examples. These methods could be used to target one set of material properties exactly subject to achieving a property within specified tolerances δ_k or to design of meta-materials under uncertainty (see Seepersaad et al. [38]).

Finally, when using the material targets as objectives and constraining volume fractions as in Problem (4.5), only solutions in which the boundary constraints are degenerate were shown to exist when all of the material requirements are met, and in the rare case that all boundary constraints on the design variables are met, the problem is mathematically ill-posed. Again, the degeneracy asserts that the design variable constraints do not take an important role in the topology optimization method, which is contrary to the desirability of a 1-0 solution at optimality. Design examples given in Section 4 support this conclusion, because none of the optimizations were successful, despite the existence of feasible, SIMP-convergent geometries. When one or more material requirements is not achieved, the KKT conditions were shown to hold at an optimal point with non-trivial solutions for the Lagrange multipliers.

Comparing each of the three problems for targeting a single material property, only Problem (4.3) and Problem (4.4) with non-zero δ were shown to be theoretically and numerically well-posed. Additionally, the numerical results suggest that implementing Problem

(4.3) may be more numerically efficient than implementing Problem (4.4), but further testing is required. When using these problems to target multiple material properties, Problem (4.3) and Problem (4.4) with non-zero δ were shown to be well-posed problems when all material constraints are met, whereas Problem (4.5) was only well-posed when one or more material constraints was explicitly not met in the optimization. These results suggest that Problems (4.3) and (4.4) are more viable optimization formulations for topology design.

4.5 Summary

The optimality conditions are derived for three meta-material topology optimization problems: two targeting meta-material properties using linear equality or quadratic inequality constraints, respectively, while minimizing a volume function, and one minimizing the differences between material targets and material properties in the objective while constraining the allowed volume fraction. Based on the analysis presented here, the formulation using linear constraints is recommended because it is mathematically well-posed and offers the desired 1-0 solutions for topology design. Surprisingly, this formulation is not prevalent in the literature. On the other hand, the other formulations that are widely-used are not always well-posed, and they admit solutions that do not achieve 1-0 convergence. Future insights may be provided by considering the physical material properties represented by the function $E(\mathbf{x})$.

Chapter 5

Topology Optimization Using Volume Averaging

In Chapter 3, it was demonstrated that the volume averaging analysis is accurate for analyzing single-layer material properties, while asymptotic homogenization is not. Then, in Chapter 4, the KKT and FJ optimality conditions for three different meta-material topology optimization problems where meta-material properties are targeted were analyzed. Given these, a topology optimization method using the volume averaging analysis can be built.

In this chapter, a topology optimization routine for the volume averaging analysis is described. The SIMP interpolation is used to parameterize the design space with variables x_i . Design sensitivities (first order derivatives with respect to the design variables) are obtained for all of the constraints. This includes calculating the derivatives of the volume fraction $V(\mathbf{x})$ and the meta-material properties $E_{22}^U(\mathbf{x})$, $E_{33}^U(\mathbf{x})$ and $G_{23}^U(\mathbf{x})$ with respect to the design variables, written as $\frac{\partial V}{\partial x_i}$, $\frac{\partial E_{22}^U}{\partial x_i}$, $\frac{\partial E_{33}^U}{\partial x_i}$ and $\frac{\partial G_{23}^U}{\partial x_i}$, respectively, are derived. The effect of initial points is investigated briefly next, and then results are given for the optimization programs, written using the described parametrization, analysis and sensitivities.

5.1 Optimization Methods

Given the mathematical analysis of the optimality conditions in Chapter 4, the optimization method in which a minimum volume is desired subject to a linear equality constraint, Problem 4.3, was chosen. For the targeted optimization of E_k^U using the volume averaging analysis (where E_k^U is E_{22}^U , E_{33}^U or G_{23}^U), this problem is written

$$\begin{aligned}
 & \min_{\mathbf{x}} V(\mathbf{x}) & (5.1) \\
 \text{s.t. } & h_k = E_k^U(\mathbf{x}) - E_k^* = 0 \text{ for } k \in \{22, 33, 23\} \\
 & g_i^2 = x_i - 1 \leq 0, \forall i \in \{1, 2, \dots, n\} \\
 & g_i^3 = -x_i \leq 0, \forall i \in \{1, 2, \dots, n\}
 \end{aligned}$$

With a well-posed optimization problem (the optimality conditions can be achieved), a deterministic optimization algorithm can be applied to obtain an optimum solution. As discussed in Chapter 2, approximation methods (SLP, SQP and MMA) are commonly used to solve a topology optimization problem. MATLAB's optimization toolbox provides an implementation of the SQP algorithm through the `fmincon()` function [88]. At every iteration of the algorithm, the SQP algorithm computes a local quadratic approximation of the objective function and local linear approximations of the constraints through the use of Taylor expansions, but to do this, derivatives of these functions must be obtained [89]. Finite difference methods can be used to calculate these derivatives numerically, but they are very inefficient for problems with large numbers of design variables. Instead, closed-form expressions for the derivatives of the analysis functions with respect to the design variables, called design sensitivities, are typically provided to significantly increase the computational efficiency of the optimization algorithm. In this work, the design sensitivities for Problem 5.1 are derived first for a single unit cell, and then they are extended to the design of multiple unit cells by using variable linking techniques between unit cells.

5.1.1 Single Unit Cell Design Sensitivities

There are three types of functions for which design sensitivities are needed: one for the volume fraction $V(\mathbf{x})$, one for the meta-material constraint h_k , and those for the design variable bounds g_i . The sensitivities for the design variable bounds g_i are trivial and calculated within MATLAB's optimization toolbox. For the volume fraction sensitivity, recall

$$V(\mathbf{x}) = \frac{1}{n} \sum_{j=1}^n x_j \quad (5.2)$$

which, for a continuously interpolated topology optimization problem, sensitivities are given by

$$\nabla V(\mathbf{x}) = \frac{1}{n} \mathbf{u} \quad (5.3)$$

where $\mathbf{u} = (1, 1, \dots, 1)^T$ is a vector of ones with length n .

The design sensitivities for the linear constraint function $h(\mathbf{x})$ for a single unit cell

$$h_k(\mathbf{x}) = E_k^U(\mathbf{x}) - E_k^* \quad (5.4)$$

are not as simple to calculate. The derivative of Eq. 5.4 with respect to design variable x_l is

$$\frac{\partial h_k(\mathbf{x})}{\partial x_l} = \frac{\partial E_k^U(\mathbf{x})}{\partial x_l} \quad (5.5)$$

From Chapter 2, recall that the compliance C of the structure can be given as a function of strains ε_k , meta-material property E_k^U and unit cell volume Y (when only in a single mode of deformation) as

$$C = \varepsilon_k E_k^U \varepsilon_k Y \quad (5.6)$$

Applying the meta-material linear constitutive relation Eq. 2.15, equilibrium requirements Eqs. 2.21 and 2.22, and strain energy equivalence requirement for an RVE Eq. 2.17 (note,

this assumes the analysis volume is an RVE), Eq. 5.6 can be written as

$$E_k^U = \frac{C}{Y (\bar{\varepsilon}_k)^2} \quad (5.7)$$

where the bar denotes the strain was prescribed as a (constant) parameter of the FEA. Thus, the sensitivity of material property E_k^U with respect to design variable x_l (and also constraint h_k via Eq. 5.5) is given as a factor of the derivative of the compliance function, or

$$\frac{\partial E_k^U}{\partial x_l} = \frac{1}{Y (\bar{\varepsilon}_k)^2} \frac{\partial C}{\partial x_l} \quad (5.8)$$

Similarly, if the stress is prescribed as a constant parameter of the FEA, the meta-material property can be written

$$E_k^T = \frac{(\bar{\sigma}_k)^2 Y}{C} \quad (5.9)$$

The derivative with respect to design variable is

$$\frac{\partial E_k^T}{\partial x_l} = -\frac{(\bar{\sigma}_k)^2 Y}{C^2} \frac{\partial C}{\partial x_l} \quad (5.10)$$

This particular formulation is convenient because sensitivity equations in classic minimum compliance topology optimization are written in terms of the compliance function, and simple extension of those methods can be utilized.

To calculate the design sensitivities with respect to the compliance when displacement boundary conditions are used, recall the compliance function can be written in terms of loads \mathbf{f} and displacements \mathbf{u}

$$C = \mathbf{u}^T \mathbf{f} \quad (5.11)$$

where both the loads and displacements are found through the FEA. Eq. 5.11 is written in terms of free and constrained nodes, denoted by subscripts F and C, respectively. With displacement boundary conditions, there are no forces applied to any nodes in the finite element model. (Recall from Chapter 2 that, in the case of the Young's modulus E_{22}^U

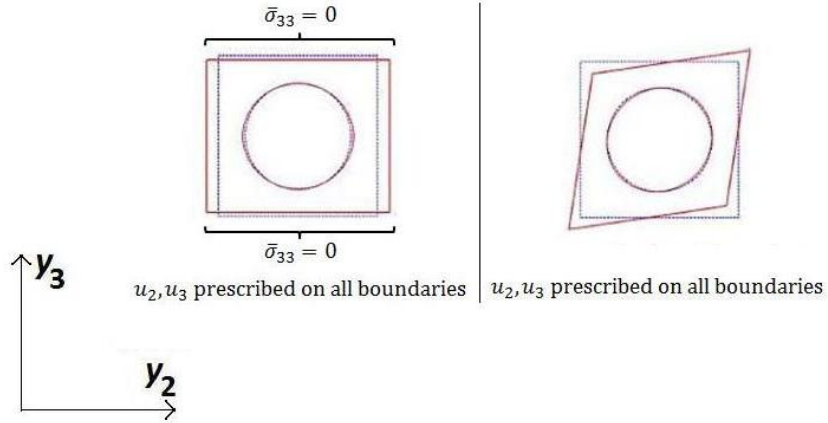


Figure 5.1: Depiction of periodicity and variable linking for optimization.

simulation, for the upper and lower boundaries displacements u_2 are directly prescribed and displacements u_3 are applied such that the average normal stresses $\bar{\sigma}_{33}$ on these two boundaries are zero, while the displacements u_2 and u_3 are directly prescribed for the nodes on the left and right boundaries; the simulation for E_{33}^U is similar. In the case of the shear modulus G_{23}^U simulation, the boundary displacements u_2 and u_3 are all prescribed. See Figure 5.1.) Thus,

$$C = [\mathbf{u}_F^T \quad \mathbf{u}_C^T] \begin{bmatrix} 0 \\ \mathbf{f}_C \end{bmatrix} = \mathbf{u}_C^T \mathbf{f}_C \quad (5.12)$$

the derivative of the compliance with respect to the design variables is written

$$\frac{\partial C}{\partial x_l} = \frac{\partial \mathbf{u}_C^T}{\partial x_l} \mathbf{f}_C + \mathbf{u}_C^T \frac{\partial \mathbf{f}_C}{\partial x_l} = \mathbf{u}_C^T \frac{\partial \mathbf{f}_C}{\partial x_l} \quad (5.13)$$

In Eq. 5.13, the first term vanishes because the displacements of the constrained nodes do not change with respect to a change in design variables, as only displacement boundary constraints are used:

$$\frac{\partial \mathbf{u}_C^T}{\partial x_l} = \mathbf{0} \quad (5.14)$$

The derivatives of the forces with respect to the design variables for the constrained nodes

are found by writing the finite element equation

$$\mathbf{K}(\mathbf{x})\mathbf{u} = \mathbf{f} \quad (5.15)$$

in terms of constrained and free nodes:

$$\begin{bmatrix} \mathbf{K}_{\mathbf{FF}} & \mathbf{K}_{\mathbf{FC}} \\ \mathbf{K}_{\mathbf{CF}} & \mathbf{K}_{\mathbf{CC}} \end{bmatrix} \begin{bmatrix} \mathbf{u}_{\mathbf{F}} \\ \mathbf{u}_{\mathbf{C}} \end{bmatrix} = \begin{bmatrix} \mathbf{0} \\ \mathbf{f}_{\mathbf{C}} \end{bmatrix} \quad (5.16)$$

The first line of Eq. 5.16 is

$$\mathbf{K}_{\mathbf{CF}}\mathbf{u}_{\mathbf{F}} + \mathbf{K}_{\mathbf{CC}}\mathbf{u}_{\mathbf{C}} = \mathbf{f}_{\mathbf{C}} \quad (5.17)$$

the derivative of which, utilizing Eq. 5.14, gives

$$\frac{\partial \mathbf{f}_{\mathbf{C}}}{\partial x_l} = \frac{\partial \mathbf{K}_{\mathbf{CF}}}{\partial x_l} \mathbf{u}_{\mathbf{F}} + \mathbf{K}_{\mathbf{CF}} \frac{\partial \mathbf{u}_{\mathbf{F}}}{\partial x_l} + \frac{\partial \mathbf{K}_{\mathbf{CC}}}{\partial x_l} \mathbf{u}_{\mathbf{C}} \quad (5.18)$$

The second line of the matrix equation is used to write the relation

$$\mathbf{u}_{\mathbf{F}} = -\mathbf{K}_{\mathbf{FF}}^{-1} \mathbf{K}_{\mathbf{FC}} \mathbf{u}_{\mathbf{C}} \quad (5.19)$$

which implies

$$\frac{\partial \mathbf{u}_{\mathbf{F}}}{\partial x_l} = -\frac{\partial \mathbf{K}_{\mathbf{FF}}^{-1}}{\partial x_l} \mathbf{K}_{\mathbf{FC}} \mathbf{u}_{\mathbf{C}} - \mathbf{K}_{\mathbf{FF}}^{-1} \frac{\partial \mathbf{K}_{\mathbf{FC}}}{\partial x_l} \mathbf{u}_{\mathbf{C}} \quad (5.20)$$

By applying the matrix relation

$$\frac{\partial \mathbf{A}^{-1}}{\partial x_l} = \mathbf{A}^{-1} \frac{\partial \mathbf{A}}{\partial x_l} \mathbf{A}^{-1} \quad (5.21)$$

Eq. 5.20 becomes

$$\frac{\partial \mathbf{u}_{\mathbf{F}}}{\partial x_l} = -\mathbf{K}_{\mathbf{FF}}^{-1} \frac{\partial \mathbf{K}_{\mathbf{FF}}}{\partial x_l} \mathbf{K}_{\mathbf{FF}}^{-1} \mathbf{K}_{\mathbf{FC}} \mathbf{u}_{\mathbf{C}} - \mathbf{K}_{\mathbf{FF}}^{-1} \frac{\partial \mathbf{K}_{\mathbf{FC}}}{\partial x_l} \mathbf{u}_{\mathbf{C}} \quad (5.22)$$

which, utilizing Eq. 5.19, is written

$$\frac{\partial \mathbf{u}_F}{\partial x_l} = \mathbf{K}_{FF}^{-1} \frac{\partial \mathbf{K}_{FF}}{\partial x_l} \mathbf{u}_F - \mathbf{K}_{FF}^{-1} \frac{\partial \mathbf{K}_{FC}}{\partial x_l} \mathbf{u}_C \quad (5.23)$$

Define \mathbf{H}^e as the elemental stiffness matrix for element e , and define \mathbf{H}_{CC}^e , \mathbf{H}_{FC}^e , \mathbf{H}_{CF}^e and \mathbf{H}_{FF}^e as the corresponding elemental stiffness matrices split according to the constrained and free nodes, extracted from \mathbf{H}^e . The matrix \mathbf{H}^e has the dimensions of the global stiffness matrix \mathbf{K} such that the assembly of the global stiffness matrix is given by a sum of the elemental stiffness matrices according to the finite element assembly process:

$$\mathbf{K} = \sum_e \mathbf{H}^e \quad (5.24)$$

Using the SIMP interpolation with SIMP exponent s , a component of any of \mathbf{H}_{CC}^e is written

$$\mathbf{H}_{CC}^e = \mathbf{H}_{CC,0} x_e^s \quad (5.25)$$

Thus,

$$\mathbf{K}_{CC} = \sum_e \mathbf{H}_{CC,0} x_e^s \quad (5.26)$$

and the derivative is given by

$$\frac{\partial \mathbf{K}_{CC}}{\partial x_l} = \sum_e \mathbf{H}_{CC,0} \frac{\partial x_e^s}{\partial x_l} = \sum_e \mathbf{H}_{CC,0} s x_e^{s-1} \delta_{le} = \mathbf{H}_{CC,0} x_l^s \frac{s}{x_l} = \mathbf{H}_{CC}^l \frac{s}{x_l} \quad (5.27)$$

(The first order derivatives of the global stiffness matrices with respect to design variable x_l follow a similar calculation.) With this result, Eq. 5.23 is written

$$\frac{\partial \mathbf{u}_F}{\partial x_l} = \mathbf{K}_{FF}^{-1} \left(\mathbf{H}_{FF}^l \mathbf{u}_F - \mathbf{H}_{FC}^l \mathbf{u}_C \right) \frac{s}{x_l} \quad (5.28)$$

which is then inserted into Eq. 5.18 to give

$$\frac{\partial \mathbf{f}_C}{\partial x_l} = \mathbf{H}_{CF}^l \frac{s}{x_l} \mathbf{u}_F + \mathbf{K}_{CF} \mathbf{K}_{FF}^{-1} \left(\mathbf{H}_{FF}^l \mathbf{u}_F - \mathbf{H}_{FC}^l \mathbf{u}_C \right) \frac{s}{x_l} + \mathbf{H}_{CC}^l \frac{s}{x_l} \mathbf{u}_C \quad (5.29)$$

Factoring like terms and expressing Eq. 5.29 as a matrix equation gives

$$\frac{\partial \mathbf{f}_C}{\partial x_1} = \frac{s}{x_l} \left[\mathbf{H}_{CF}^l - \mathbf{K}_{CF} \mathbf{K}_{FF}^{-1} \mathbf{H}_{FF}^l \mid - \mathbf{K}_{CF} \mathbf{K}_{FF}^{-1} \mathbf{H}_{FC}^l + \mathbf{H}_{CC}^l \right] \begin{bmatrix} \mathbf{u}_F \\ \mathbf{u}_C \end{bmatrix} \quad (5.30)$$

Using Eq. 5.30, Eq. 5.13 is written

$$\frac{\partial C}{\partial x_l} = \frac{s}{x_l} \left[\mathbf{u}_C^T \mathbf{H}_{CF}^l - \mathbf{u}_C^T \mathbf{K}_{CF} \mathbf{K}_{FF}^{-1} \mathbf{H}_{FF}^l \mid - \mathbf{u}_C^T \mathbf{K}_{CF} \mathbf{K}_{FF}^{-1} \mathbf{H}_{FC}^l + \mathbf{u}_C^T \mathbf{H}_{CC}^l \right] \begin{bmatrix} \mathbf{u}_F \\ \mathbf{u}_C \end{bmatrix} \quad (5.31)$$

By using Eq. 5.19, the central two terms of Eq. 5.31 are simplified to yield

$$\frac{\partial C}{\partial x_l} = \frac{s}{x_l} \left[\mathbf{u}_C^T \mathbf{H}_{CF}^l + \mathbf{u}_F^T \mathbf{H}_{FF}^l \mid \mathbf{u}_F^T \mathbf{H}_{FC}^l + \mathbf{u}_C^T \mathbf{H}_{CC}^l \right] \begin{bmatrix} \mathbf{u}_F \\ \mathbf{u}_C \end{bmatrix} \quad (5.32)$$

which is further simplified to

$$\frac{\partial C}{\partial x_l} = \frac{s}{x_l} \left[\mathbf{u}_F^T \mid \mathbf{u}_C^T \right] \begin{bmatrix} \mathbf{H}_{FF}^l & \mathbf{H}_{FC}^l \\ \mathbf{H}_{CF}^l & \mathbf{H}_{CC}^l \end{bmatrix} \begin{bmatrix} \mathbf{u}_F \\ \mathbf{u}_C \end{bmatrix} \quad (5.33)$$

By recombining the matrices and using the definition of the compliance, Eq. 5.33 is written

$$\frac{\partial C}{\partial x_l} = \frac{s}{x_l} \mathbf{u}_l^T \mathbf{H}^l \mathbf{u}_l = \frac{s}{x_l} \mathbf{u}_l^T \mathbf{f}_l = \frac{s}{x_l} C_l \quad (5.34)$$

By inserting the result from Eq. 5.34 into Eq. 5.8 and then into Eq. 5.5, the sensitivities for the material constraint is written

$$\frac{\partial h(\mathbf{x})}{\partial x_l} = \frac{\partial E_k^U(\mathbf{x})}{\partial x_l} = \frac{1}{Y(\bar{\varepsilon}_k)^2} \frac{s}{x_l} C_l \quad (5.35)$$

Design problems in which traction boundary conditions are used is more common in topology optimization, and the derivative of the compliance with respect to design variable

x_l is found readily in the literature [90], [91], [92], [93]:

$$\frac{\partial C}{\partial x_l} = -\frac{s}{x_l} C_l \quad (5.36)$$

Note, Eq. 5.36 is the same as Eq. 5.34, less a difference in sign. Given Eqs. 5.36, 5.10 and Eq. 5.5, the derivative of the material constraint with respect to the design variable x_l is

$$\frac{\partial h(\mathbf{x})}{\partial x_l} = \frac{(\bar{\sigma}_k)^2 Y}{C^2} \frac{s}{x_l} C_l \quad (5.37)$$

5.1.2 Multiple Unit Cell Design Sensitivities

When designing multiple unit cells using volume averaging, because of the periodic nature of the structure, variables can be linked in the optimization problem. Figure 5.2 depicts a four unit cell geometry in which the corresponding elements from each unit cell have the same value for the design density, x_e . Given the equivalence of element densities

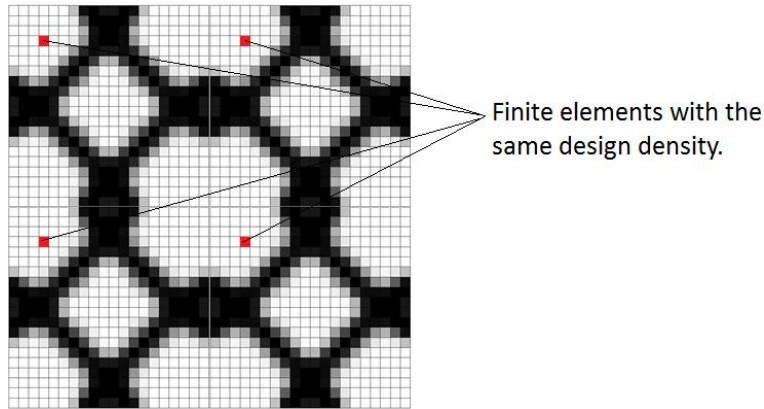


Figure 5.2: Depiction of periodicity and variable linking for optimization.

from one unit cell to the next periodically, the optimization problem can be reduced from a problem with nxN variables (where n is the number of finite elements in a unit cell and N is the number of unit cells in the design domain) to a problem with n variables. This implies the volume fraction and volume fraction sensitivities are the same as given in Eqs. 5.2 and 5.3, respectively.

The material constraint and sensitivities can be derived by following a derivation similar to that found in Qiu et al. [93]. When displacement boundary conditions are used, the derivative of the constraint given in Eq. 5.4 reads

$$\frac{\partial h_k(\mathbf{x})}{\partial x_l} = \frac{\partial E_k^U}{\partial x_l} = \frac{1}{Y(\bar{\varepsilon}_k)^2} \frac{\partial C}{\partial x_l} \quad (5.38)$$

where C is the compliance of the N unit cells of the meta-material, and

$$C = \mathbf{U}^T \mathbf{F} = \sum_{j=1}^N C^j \quad (5.39)$$

Here, \mathbf{F} and \mathbf{U} are the global load and displacement vectors, composed of the force and load vectors of the individual unit cells. From Eq. 5.39, the derivative with respect to element density x_l is given by

$$\frac{\partial C}{\partial x_l} = \frac{\partial(\mathbf{U}^T \mathbf{F})}{\partial x_l} = \sum_{j=1}^N \frac{\partial C^j}{\partial x_l} \quad (5.40)$$

Using Eq. 5.34, and factoring by recognizing that each unit cell shares in common the same element density for element l but not compliance, Eq. 5.40 is written

$$\frac{\partial C}{\partial x_l} = \frac{s}{x_l} \sum_{j=1}^N C_l^j \quad (5.41)$$

Finally, using this result in Eq. 5.38 gives

$$\frac{\partial h_k(\mathbf{x})}{\partial x_l} = \frac{1}{Y(\bar{\varepsilon}_k)^2} \frac{s}{x_l} \sum_{j=1}^N C_l^j \quad (5.42)$$

Thus, the element sensitivities for the optimization of multiple cells are given as a simple sum of compliances of the individual elements across the N unit cells. These sensitivities were validated using a finite differences MATLAB code, similar to the single cell sensitivities.

The derivation of the sensitivities when traction boundary conditions are used is

similar:

$$\frac{\partial h_k(\mathbf{x})}{\partial x_l} = \frac{(\bar{\sigma}_k)^2 Y}{C^2} \frac{s}{x_l} \sum_{j=1}^N C_l^j \quad (5.43)$$

5.2 Optimization Parameters and Results

The multiple cell optimization code was implemented using MATLAB’s SQP solver through the `fmincon()` function with the design sensitivities derived in the preceding section. Because the design sensitivities are derived for materials that meet the RVE requirement, it is only necessary to apply one set of boundary conditions, as the other set of boundary conditions will produce the same set of moduli (as demonstrated by Drago and Pindera [47] and verified in Chapter 3). Given this, displacement boundary conditions were used in the FEA for implementation with the topology optimization code. An isotropic base material with Young’s modulus $E = 30$ GPa and Poisson’s ratio $\nu = 0.3$ was used with a plane stress condition on the finite elements such that the two-dimensional linear constitutive matrix D is given by

$$D = \frac{E}{1 - \nu^2} \begin{bmatrix} 1 & \nu & 0 \\ \nu & 1 & 0 \\ 0 & 0 & \frac{1-\nu}{2} \end{bmatrix} \quad (5.44)$$

5.2.1 Initial Point Study

Because initial points can play a key role in optimization problems, different initial design domains were used (Figure 5.3). These points are the single-cell representation of the multi-cell optimization problem. Four different points were selected: a fully-filled design domain, the ‘x’ and ‘+’ geometries, and a filled domain with a centered, square hole. The fully-filled point is the simplest initial point and is commonly used in minimum compliance TO, the ‘x’ and ‘+’ geometries represent local topological minima of the shear and tension material design problems, and the square hole point is adapted from the original papers on the homogenization problem ([41], [4]).

Each of these initial points were used for optimization of a 3x3 unit cell design

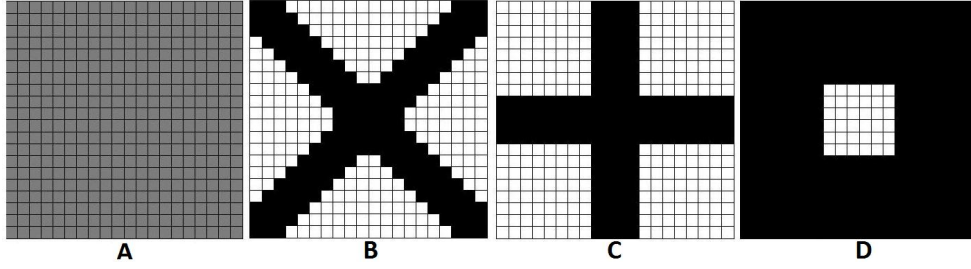


Figure 5.3: Initial points used for topology optimization of materials. A is a fully-filled design domain, B and C are the ‘x’ and ‘+’ geometries, and D is a material with a square hole in the middle.

domain to target $E_{22} = 3$ or 15 GPa, $E_{33} = 3$ or 15 GPa, or $G_{23} = 2$ or 6 GPa. As a termination parameter, the required constraint satisfaction tolerance and objective tolerance were set to 10^{-4} GPa and 10^{-4} , respectively. In the event that the optimizer could not achieve a local minimum, the algorithm was set to terminate early after 200 iterations or after 1000 function evaluations.

Numerical results are shown in Table 5.1 and visual results are shown in Figures 5.4-5.9. From the numerical results, by recalling that the minimum volume fraction was sought by the optimization, it is clear that initial point A, the fully-filled point, is the worst performing of the four points. As for the optimizations using the other three initial points, it is not clear that one point outperformed another based off of the volume fraction or constraint satisfaction that the target modulus E_k^* is equal to the achieved modulus E_k^U at optimality.

The visual optimization results demonstrate a few important points. First, optimization from a uniform point using the volume averaging model leads to a uniform solution. This is because, in a single mode of deformation, the stress gradient at every iteration is constant across the elements. This, in turn, makes the compliance and, thus, the element sensitivities with respect to the material constraint, constant. The optimizer is unable to differentiate from one element to the next, leaving the uniform solution to be the only possible solution. The elements all have the same intermediate density, making the solution non-SIMP convergent. (Recall that SIMP convergence requires the solutions be primarily a

Table 5.1: Numerical Results For Optimization Using Different Initial Design Points

Initial Point	E_{22}^* [GPa]	E_{22}^U [GPa]	V	Comp. Time [s]	Iter.	Func. Eval.
A	3	3.000	0.464	33.9	6	11
B	3	3.001	0.153	1015.3	94	360
C	3	2.943	0.221	2619.4	142	1001
D	3	3.090	0.181	2503.1	137	1001
A	15	15.000	0.794	22.2	4	7
B	15	14.979	0.592	2533.2	146	1001
C	15	14.986	0.614	2521.5	137	1001
D	15	0.000	0.054	156.8	9	62

Initial Point	E_{33}^* [GPa]	E_{33}^U [GPa]	V	Comp. Time [s]	Iter.	Func. Eval.
A	3	3.000	0.464	33.6	6	11
B	3	2.995	0.161	2888.1	155	1001
C	3	2.999	0.232	2171.8	137	825
D	3	3.034	0.174	2469.3	128	1001
A	15	15.000	0.794	21.8	4	7
B	15	14.839	0.579	2504.1	167	1001
C	15	15.000	0.715	1119.6	68	453
D	15	14.961	0.647	2532.4	144	1001

Initial Point	G_{23}^* [GPa]	G_{23}^U [GPa]	V	Comp. Time [s]	Iter.	Func. Eval.
A	2	2.000	0.558	26.8	5	9
B	2	1.964	0.441	2206.2	179	1001
C	2	1.999	0.334	820.1	56	371
D	2	1.987	0.429	2214.1	176	1001
A	6	6.000	0.804	20.35	4	7
B	6	6.000	0.806	202.1	27	87
C	6	0.000	0.040	97.0	11	89
D	6	6.001	0.739	507.4	63	225

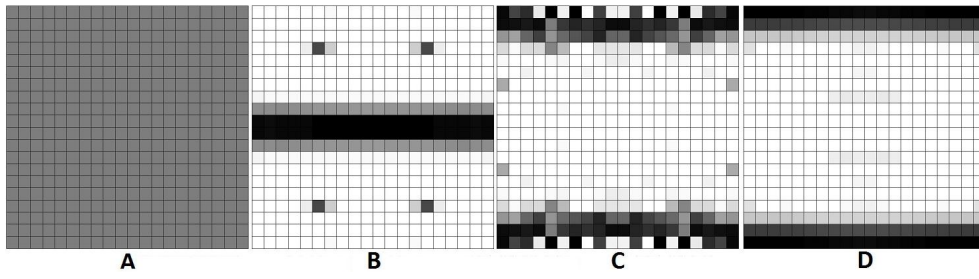


Figure 5.4: Target Modulus $E_{22}^* = 3$ GPa

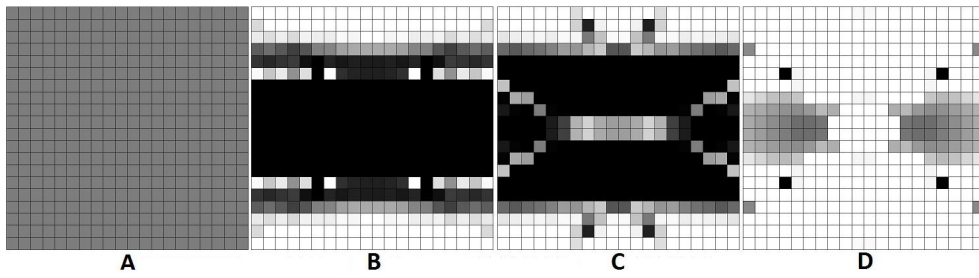


Figure 5.5: Target Modulus $E_{22}^* = 15$ GPa

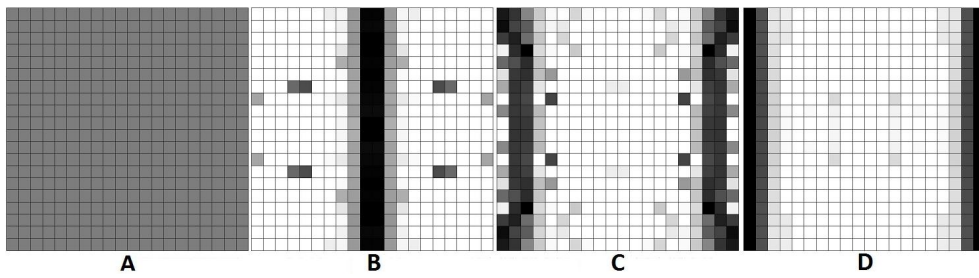


Figure 5.6: Target Modulus $E_{33}^* = 3$ GPa

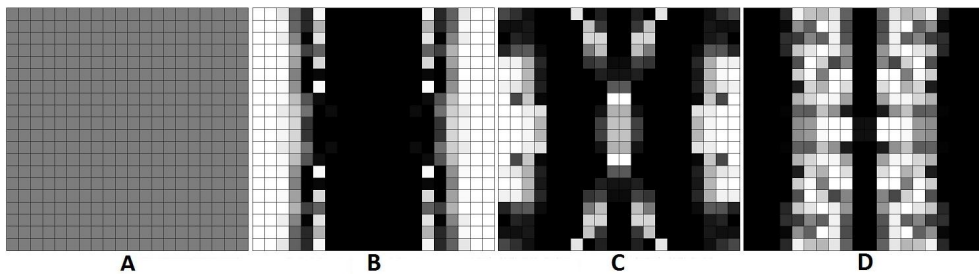


Figure 5.7: Target Modulus $E_{33}^* = 15$ GPa

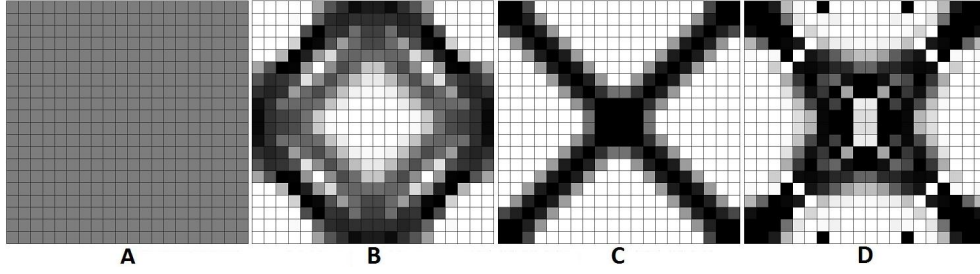


Figure 5.8: Target Modulus $G_{23}^* = 2$ GPa

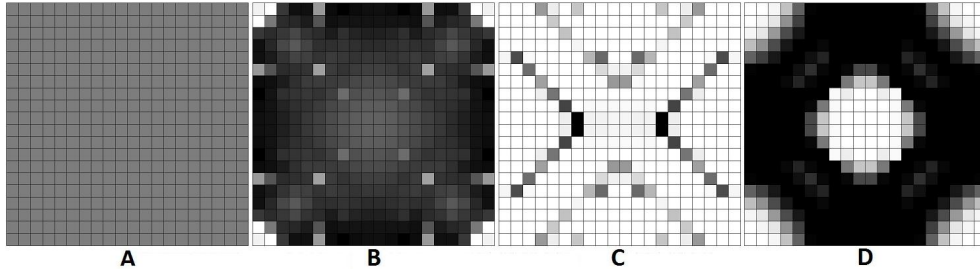


Figure 5.9: Target Modulus $G_{23}^* = 6$ GPa

1-0 solution, representing the presence or absence of material, respectively.) However, the material constraint is reached in every case, providing partial validation of the optimization method. In the other cases, solutions that are SIMP convergent are those from initial points B and D in Figures 5.4 and 5.6, the solution from initial point C in Figure 5.8, and the solution from initial point D in Figure 5.9.

The optimization results from the attempts to achieve $E_{22}^U = 15$ GPa demonstrate an interesting, but commonplace, result. In the three cases in which the initial points B, C and D were used, none of the optimizations were successful. Optimization efforts from points B and C terminated before reaching optimality, while the optimization from initial point D jumped almost immediately to a boundary of the optimization and was unable to satisfy the material constraint, terminating the optimization early. These result from either the initial point being outside the feasible design space, or from the lack of an optimal, SIMP-convergent solution for the optimization problem. These are typical problems in material design by TO, as well as in TO in general. The former issue can be solved by

choosing a different initial point within the feasible domain (if one exists), while the latter issue can usually be solved by optimizing with a finer finite element mesh. Finer domain discretization and subsequent optimization has been done here, but is not presented in this work for brevity. It is clear that there is a continuously thicker solution that will solve the optimization problem to achieve a continuously varied material constraint on E_{22}^U , but domain discretization with finite elements effectively discretizes the solution space to only discrete values.

Given these results, two major conclusions can be drawn. First, optimization from a uniform starting point using the volume averaging model will not generally result in a SIMP convergent solution. A large number of elements must be tuned to intermediate or minimum density as an initial point. Second, by using different initial points, different SIMP convergent solutions with different topologies that achieve the material constraints can be found. This demonstrates the existence of different local minima for the material TO problem using the volume averaging model. However, this is no different from any other TO problem that uses a material interpolation scheme. This issue was discussed briefly in the context of the literature review in Chapter 2.

5.2.2 Optimization of a Single Layer of Cells

As was discussed in Chapter 3, the volume averaging and homogenization models both agree when the assumptions of homogenization are met. However, these assumptions are not met for the design of a single layer of UCs. For these materials, the volume averaging model was shown to be the more accurate of the two models. Given this, the focus of the optimization in this chapter using the volume averaging method is for design of single layer materials.

Three sets of optimization problems were solved by simulating a single layer with 12 square UCs with individual 20x20 finite element discretizations. In each set, different meta-material moduli E_k^* were targeted for a single mode of deformation (horizontal tension, vertical tension, and transverse shear) using the methods presented in the Section 5.1. The

same termination parameters and base material were used as in the initial point study from Section 5.2.1. The initial point with a square hole (D from Figure 5.3) was used. Some numerical results and corresponding visual results are shown in Table 5.2 and Figures 5.10, 5.11 and 5.12. Complete results are reported in Appendix B.

Table 5.2: Numerical Results For Optimization of a Single Layer Material with 12x1 UCs

Def. Mode	E_k^* [GPa]	E_k^U [GPa]	V	Comp. Time [s]	Iter.	Func. Eval.
E_{22}	3	3.001	0.229	1547.9	98	318
E_{22}	9	9.001	0.347	1329.1	101	318
E_{22}	21	21.001	0.726	1078.9	58	257
E_{33}	3	3.001	0.151	1225.9	98	293
E_{33}	9	9.000	0.343	2352.1	158	563
E_{33}	21	20.999	0.738	561.2	41	137
G_{23}	2	2.001	0.416	719.5	61	188
G_{23}	4	3.996	0.562	3853.6	126	1001
G_{23}	5	5.001	0.664	666.1	55	174

From these results, it is clear that the optimization is capable of achieving a large range of target moduli for each individually targeted mode of deformation. Additionally, the topological geometries that were found were shown to be optimal periodic topologies for design of composite structures in uniaxial tension and shear stiffness [19]. For the results presented in Table 5.2, eight of the nine optimization attempts resulted in termination by reaching the desired tolerances in objective and constraints, while only one terminated before reaching desired tolerances. In this case, the value $G_{23}^* = 4$ GPa was desired, but the optimization terminated after reaching 1001 function evaluations. However, the optimizer was just outside the desired tolerance of being with 0.001 GPa of the desired shear modulus. It is possible that the optimization problem could be solved within the desired tolerances by discretizing the design domain with a finer mesh of finite elements. It appears from the visual results that the SIMP convergence was achieved in all of these cases, with very few intermediate densities present in the solutions.

There were cases in which the optimizer was not able to achieve a convergent solution. These results, which are reported in Appendix B with the all of the optimization

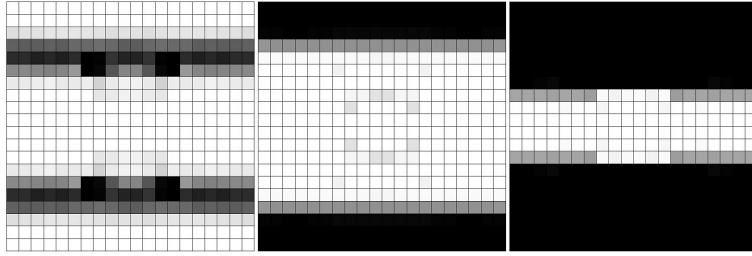


Figure 5.10: Results for the optimization of a single material layer (12x1 UCs) with target moduli $E_{22}^* = 3$ GPa, 9 GPa and 21 GPa, from left to right. Numerical results are given in Table 5.2.

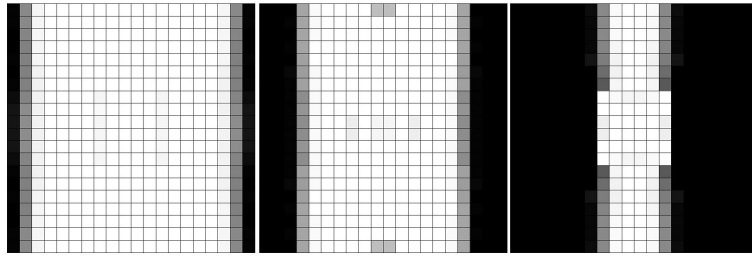


Figure 5.11: Results for the optimization of a single material layer (12x1 UCs) with target moduli $E_{33}^* = 3$ GPa, 9 GPa and 21 GPa, from left to right. Numerical results are given in Table 5.2.

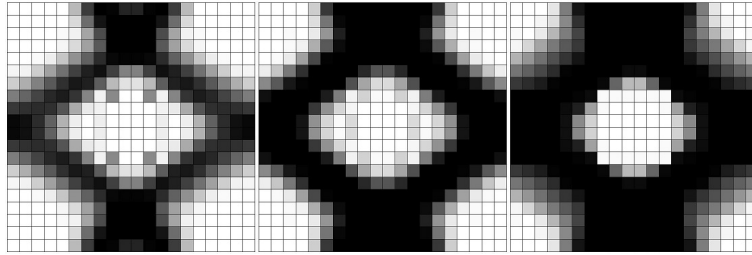


Figure 5.12: Results for the optimization of a single material layer (12x1 UCs) with target moduli $G_{23}^* = 2$ GPa, 4 GPa and 5 GPa, from left to right. Numerical results are given in Table 5.2.

results, should be easily solved by rediscretizing the design domain or beginning the optimization from a different starting point. It is also important to note that optimization by homogenization exhibits the same issues. Visual and numerical results using the standard homogenization method with the same optimization parameters are given in Appendix B

for comparison. From those results, especially when targeting a shear modulus, optimization using volume averaging appears to be as or more reliable than optimization using homogenization.

5.3 Summary

In this chapter, a topology optimization algorithm that utilizes the volume averaging analysis was presented. First-order design sensitivities were derived so that an efficient, gradient-based method could be used to solve the optimization problem. These methods were applied to single-objective optimization problems in both modes of tension and in shear. The effects of initial points on achieving both convergent and SIMP-convergent solutions were shown to be non-negligible. Single-layer solutions were successfully achieved for a wide range of optimization targets; for unsuccessful attempts, remeshing of the design domain should lead to successfully achieving the desired target. With this, the optimization algorithm using volume averaging can be applied to the design of periodic materials with a simple periodic structure of UCs.

Chapter 6

Non-Simple Connectivity In Meta-Materials Analysis and Optimization

In Chapter 3, asymptotic homogenization techniques were shown to be inaccurate in the design of single layer or thin meta-materials, while the more general volume averaging analysis was shown to provide accurate meta-material parameters when applied to these designs. Then, in Chapter 5, a topology optimization method was presented in which the volume averaging method could be used to design meta-materials in a manner similar to the topology optimization techniques used with the asymptotic homogenization analysis. In both of these chapters, only simply-connected periodic materials were considered. However, as shown in Chapter 1, arrays of non-simply connected UCs can be used to generate periodic material structures like the conventional honeycomb.

This chapter explores the same issues presented in Chapters 3 and 5 for materials with non-simple connectivity. First, a brief theoretical framework is laid for each analysis method with the displaced periodicity. Next, the accuracies of asymptotic homogenization and volume averaging are explored for thin-layered materials in the context of honeycomb

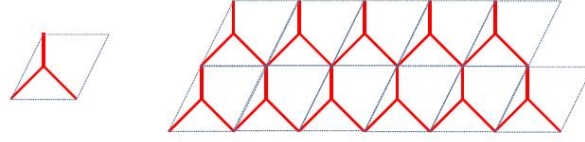


Figure 6.1: Honeycomb structure with simple periodicity made of parallelogram-shaped UCs.

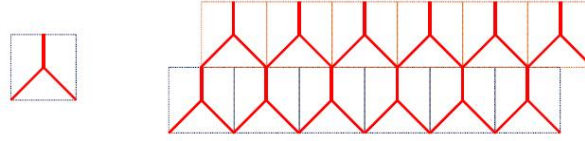


Figure 6.2: Honeycomb structure with non-simple connectivity made of rectangular UCs.

structures. As an additional validation technique, the meta-material properties predicted by these analysis methods are compared against those given by well-established, closed-form equations that predict meta-material properties for thin-walled honeycomb materials. Then, the topology optimization techniques presented in Chapter 5 are extended to the design of non-simply connected structures.

6.1 Mathematical Framework for Analysis

As discussed briefly in Section 1.3, two different periodicities could be used to generate a honeycomb: a simple periodicity with parallelogram-shaped UCs (Figure 6.1) or a non-simply connected structure with rectangular UCs (Figure 6.2).

The design of structures with simple periodicities using parallelograms has been investigated previously [22], [16]. The implementation of the parallelogram method requires that finite element equations and boundary conditions be changed to accommodate for the non-square geometry, as the original formulation was derived for square UCs. (The equations for homogenization of non-square, parallelogram UCs have since been derived by Diaz and Bénard [16]. For the averaging method, displacement and traction boundary conditions for the mechanical properties analyses of unidirectional fiber composites with square and hexagonal-shaped UCs were given by Li [94].) As was shown in Chapter 3, care

should be taken to ensure the width to length ratio remains well scaled, $W/L \approx 1$, for the homogenization equations to necessarily maintain their accuracy. Additionally, non-square finite elements must be used to discretize the design domain, which can complicate the setup of the finite element problem and bias the optimization solution (see Section 2.2.2 of the literature review in Chapter 2).

To derive what changes in the FEA are necessary when non-simply connected geometries are analyzed, first recall from Section 2.1.1 of the literature review the definition of a periodic function: a material with position vector $z = \{z_1, z_2, z_3\}$ is Y -periodic if, for all material characteristics described by function F ,

$$F(z + NY) = F(z) \quad (6.1)$$

where

$$N = \begin{bmatrix} n_1 & 0 & 0 \\ 0 & n_2 & 0 \\ 0 & 0 & n_3 \end{bmatrix} \quad (6.2)$$

and n_i are integers. $Y = \{Y_1, Y_2, Y_3\}$ is some vector that contains the periodicity of the structure, and F is any scalar, vector or tensor function of vector z . For the two-dimensional, simply-connected materials considered in Chapters 3 and 5, the displacement fields Φ_i (where $i \in 22, 33, 23$ denotes the three meta-material analyses necessary to obtain meta-material properties) satisfy

$$\Phi_i(y_1, y_2) = \Phi_i(y_1 + L, y_2) = \Phi_i(y_1, y_2 + W) = \Phi_i(y_1 + L, y_2 + W) \quad (6.3)$$

(See Figure 6.3.) In this case, the periodicity vector has the form $Y = (L, W)^T$. Meanwhile, for the non-simple periodicity depicted in Fig. 6.3, the second layer of unit cells is displaced by b in the y_2 direction such that the material displacements satisfy

$$\Phi_i(y_2, y_3) = \Phi_i(y_2 + L, y_3) = \Phi_i(y_2 + b, y_3 + W) = \Phi_i(y_2 + L + b, y_3 + W) \quad (6.4)$$

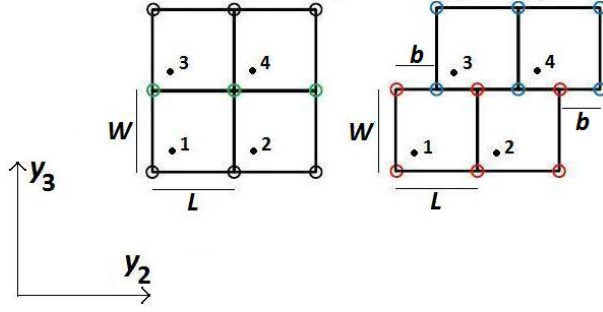


Figure 6.3: (Left) Simply-connected topology. (Right) A topology in which the unit cells are not simply connected.

In the application of asymptotic homogenization theory to finite elements, three finite element equations

$$K\Phi_i = f_i \quad (6.5)$$

(in two-dimensions) must be solved subject to some periodicity constraints. Hassani and Hinton [39] provide a straight-forward discussion of the derivation of these constraints. Up to Eq. 6.5, the derivation is general and requires no consideration of periodicity. However, the integral equations these finite element equations are derived from require that they are solved on the domain of the unit cell (with local coordinates z_i), which includes the domain boundaries. Because the displacement fields in the unit cell must be periodic throughout, when the periodicity of the unit cell is non-simple, the displacement field on the boundary of the unit cell $\chi_i \subseteq \Phi_i$ must satisfy

$$\begin{aligned} \chi_i(0, z_3) &= \chi_i(L, z_3), & 0 \leq z_3 \leq W \\ \chi_i(z_2, 0) &= \chi_i(z_2 + b, W), & 0 \leq z_2 \leq L - b \\ \chi_i(z_2, 0) &= \chi_i(z_2 - (L - b), W), & L - b \leq z_2 \leq L \end{aligned} \quad (6.6)$$

These are the displacements that must be enforced through the finite element method, either directly or through numerical methods like the Lagrange multiplier or penalty methods. For a unit cell in the non-simply connected structure analyzed using homogenization with periodic boundary conditions given in Eq. 6.6, an example of linked nodes is depicted

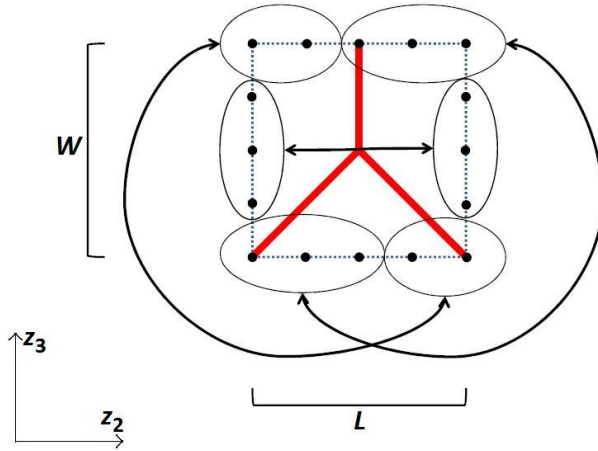


Figure 6.4: Enforcement of periodic boundary conditions for homogenization when analyzing using non-simply connected structures. (The coordinates z_i indicate the analysis domain is the UC only.)

in Fig. 6.4.

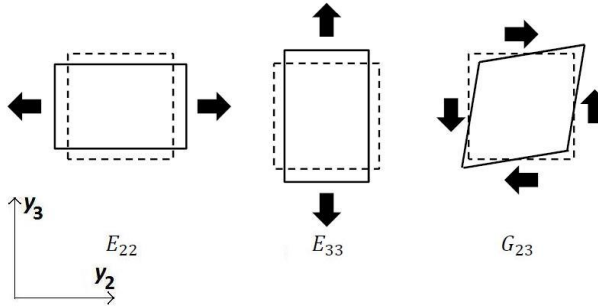


Figure 6.5: Three modes of deformation used in volume averaging.

The volume averaging method is derived from a simpler set of principles. In this method, only the average strain and average stress theorems are utilized to integrate over a number of unit cells in the analysis domain Y with meta-material coordinates (y_2, y_3) . By simulating three modes of deformation in two dimensions, two in tension and one in shear (Fig. 6.5), on the boundaries of the analysis domain and determining the average strains $\bar{\epsilon}_i$ using

$$\bar{\epsilon}_i = \frac{1}{Y} \int_Y \epsilon_i dY \quad (6.7)$$

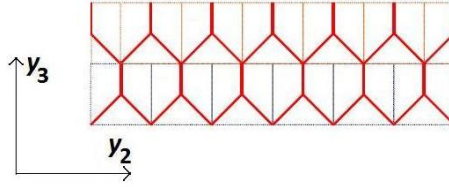


Figure 6.6: Example analysis domain of a two-layer material analyzed using the volume averaging method.

and average stresses $\bar{\sigma}_i$ using

$$\bar{\sigma}_i = \frac{1}{Y} \int_Y \sigma_i dY \quad (6.8)$$

the effective meta-material parameters E_{ij}^U can be determined as a solution of

$$\bar{\sigma}_i = E_{ij}^U \bar{\varepsilon}_i \quad (6.9)$$

When using the volume averaging method, for a two-layer system with the same periodicity given in Eq. 6.4, the second layer of the analysis volume will contain two half-cells, one on either end (Fig. 6.6). In particular, no changes to the boundary conditions or basic analysis method are required.

These equations demonstrate the design of structures with non-simple connectivity using rectangular unit cells requires few changes in the analytical methods: the homogenization analysis only requires the proper linking of periodic boundary conditions on the corresponding edges of the unit cells, while the volume averaging analysis requires no changes in boundary conditions, as a portion of the structure (beyond a single unit cell) is analyzed. The simplicity of these methods, combined with the preservation of the use of square finite elements for topology optimization, makes these methods attractive possibilities for meta-material design.

6.2 Comparison of Homogenization and Volume Averaging for Non-Simply Connected Structures

Given a simple implementation of the analyses for non-simply periodic materials, the accuracies of these methods must next be demonstrated. Here, a set of honeycomb structures was analyzed using the same methods presented in Chapter 3. Homogenization codes were used as described above to analyze meta-material properties for a single UC, and the volume averaging analysis was used to analyze meta-material properties for $N \times N$ systems of UCs and for $12 \times N$ layers of UCs. Two different thicknesses of honeycombs were chosen, one with thin members and one with much thicker members. 20×20 finite element discretizations for the UC were used.

Results from the $N \times N$ UC analyses are shown in Figures 6.7 and 6.8, while results for the $12 \times N$ layer analyses are shown in Figures 6.9 and 6.10. For the $N \times N$ analyses, it is clear that the volume averaging method agrees with homogenization for the analysis of all three elastic material properties as a larger number of UCs are included, despite the shifted periodicity. By looking at the $12 \times N$ layer analyses, it becomes clear that the non-simply connected structure affects the accuracy of some material properties in a more pronounced way than it does for other properties, as the two models do not agree as well in their estimations of the E_{22}^M Young's moduli as they do with the other two moduli, E_{33}^M and G_{23}^M . This result is consistent with the irregular periodicity of the UCs, as the second layer is shifted with respect to the first layer in the y_2 coordinate direction.

Given similar model convergence between homogenization and volume averaging for simply and non-simply connected structures (see Section 3.1 from Chapter 3), the same design comparison studies were used as those in Section 3.2. Non-simply connected meta-materials with both $N \times N$ and $12 \times N$ cell layouts were simulated under simple shear loading conditions (see Figure 3.19). The same two UCs with thin and thick members as those used to verify moduli comparison studies were used to generate $N \times N$ honeycomb materials and $12 \times N$ layered materials to evaluate the accuracies of the two analysis methods in the

meta-material design process.

The results of the design comparison analyses for the thin-member honeycomb geometries are shown in Figures 6.11 and 6.12, while the results for the thick-member geometries are shown in Figures 6.13 and 6.14. For the $N \times N$ materials, the two models appear to converge to a relative error below 10% for the thick honeycomb and a relative error below 5% for the thin honeycomb when 8×8 UCs are used in the meta-material design problem. As for the materials with layers of honeycombs, for the thick honeycomb the relative error of the displacement using the averaging method remains below 2% for any number of layers included in the meta-material; the relative error using homogenization is above 15% for a

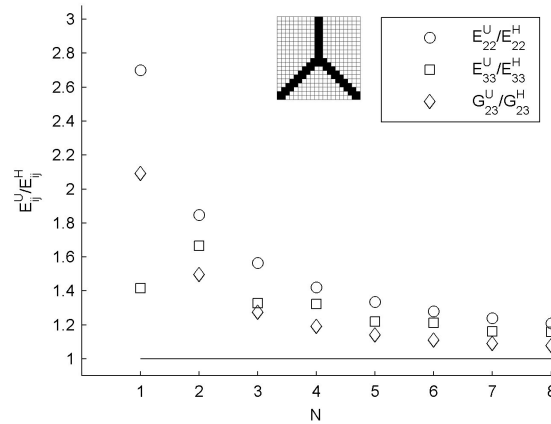


Figure 6.7: $N \times N$ analysis for meta-material moduli of thin honeycomb geometry.

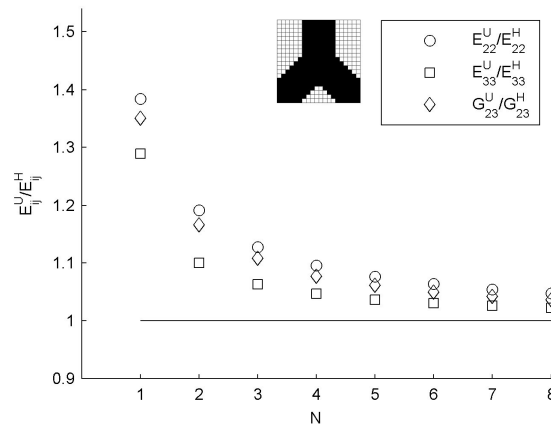


Figure 6.8: $N \times N$ analysis for meta-material moduli of thick honeycomb geometry.

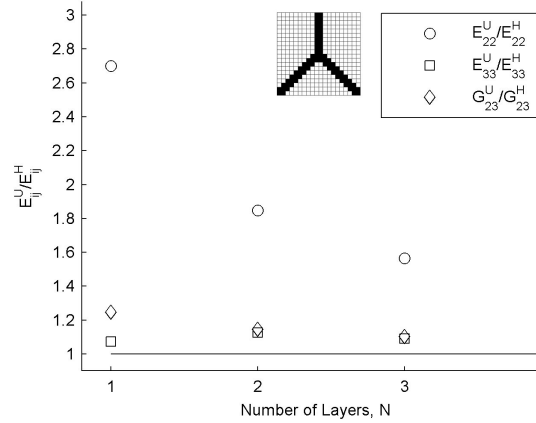


Figure 6.9: 12xN layer analysis for meta-material moduli of thin honeycomb geometry.

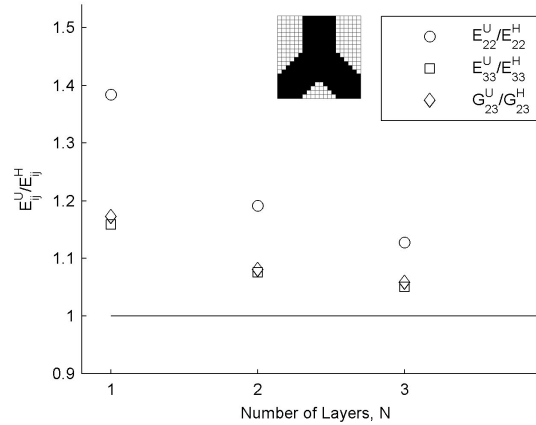


Figure 6.10: 12xN layer analysis for meta-material moduli of thick honeycomb geometry.

single layer, reaching errors around 5% upon the inclusion of three or more layers of UCs to the material. For the thin honeycomb, similar conclusion can be drawn, with the relative error using the averaging method remaining below 5% in all cases, and the homogenization method requires three or more layers to achieve relative errors below 5%.

Collectively, these results demonstrate similar model convergence as those given in Section 3.1 of Chapter 3. Thus, it makes sense to utilize lattices of rectangular UCs with non-simple connectivity for the design of meta-materials using the volume averaging or homogenization techniques.

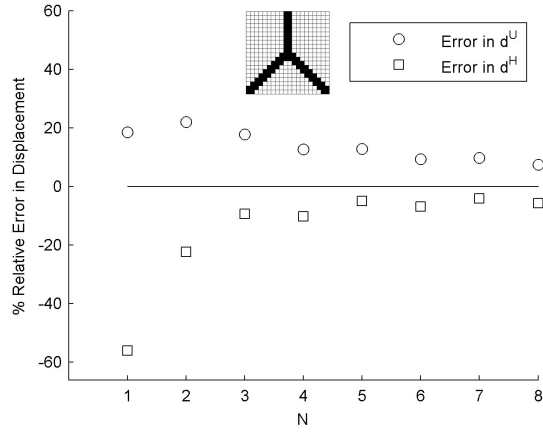


Figure 6.11: Relative errors of material displacements consisting of $N \times N$ unit cells with thin honeycomb geometry.

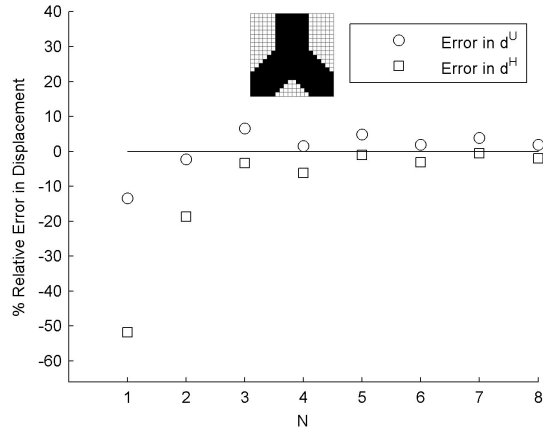


Figure 6.12: Relative errors of material displacements consisting of $N \times N$ unit cells with thick honeycomb geometry.

6.3 Comparison of Meta-Material Properties to Analytical Formulae

As an additional validation of the non-simply connected code, the meta-material properties of honeycomb structures were compared with benchmark formulae derived by Gibson et al. [95] and discussed more extensively in Gibson and Ashby [96]. The in-plane, linear elastic formulae were derived from standard beam theory (see, for example, Hibbeler [49]) considering only flexure, neglecting axial and shear effects. The E_{22} , E_{33} and G_{23}

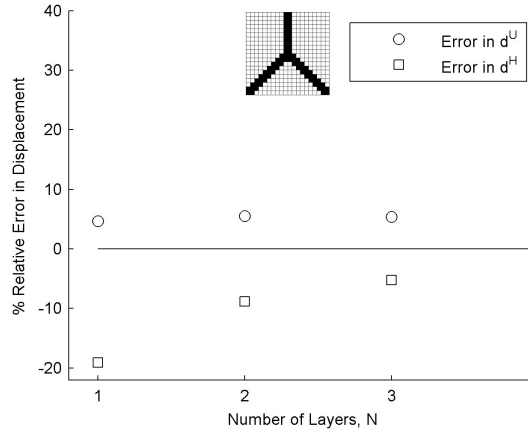


Figure 6.13: Relative errors of material displacements consisting of $12 \times N$ layers of unit cells with thin honeycomb geometry.

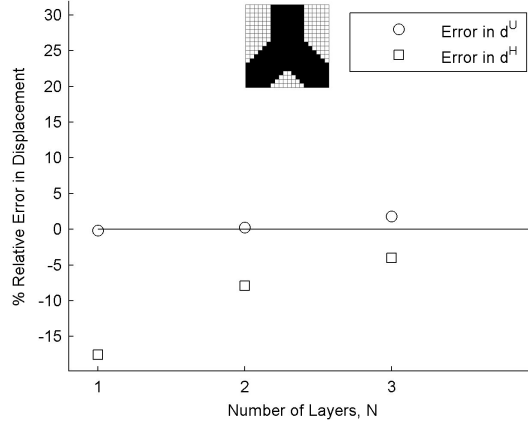


Figure 6.14: Relative errors of material displacements consisting of $12 \times N$ layers of unit cells with thick honeycomb geometry.

moduli are estimated using parameters h , t , l , and θ (see Figure 6.15) and base material with Young's modulus E_s .

$$E_{22} = E_s \frac{t^3 \cos \theta}{l^3 (h/l + \sin \theta) \sin^2 \theta} \quad (6.10)$$

$$E_{33} = E_s \frac{t^3 (h/l + \sin \theta)}{l^3 \cos^3 \theta} \quad (6.11)$$

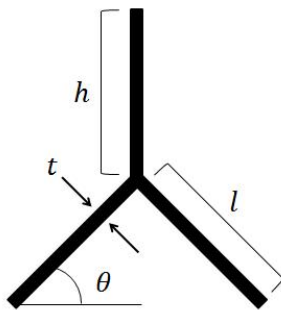


Figure 6.15: Parameters for analytical equations predicting the in-plane meta-material moduli of honeycomb structures as given by Gibson et. al [95].

$$G_{23} = E_s \frac{t^3}{l^3} \frac{(h/l + \sin \theta)}{(h/l)^2 (2h/l + 1) \cos \theta} \quad (6.12)$$

These formulae have been validated experimentally and refined for more design-specific and analysis-accuracy needs [97], [98], [99], [100].

The meta-material moduli predicted for different honeycomb structures using these analytical formulae were compared with those predicted by both homogenization and volume averaging analyses using the non-simply connected geometry described in the previous section. Honeycomb structures with varied angles θ and varied thicknesses t were analyzed to investigate the similarities and differences between the closed-form analysis and the numerical methods. 20x20 finite element discretizations of the honeycomb structures were used for the numerical methods, where an 8x8 lattice of UCs was used for volume averaging and a single cell for homogenization. A Young's modulus $E_s = 30$ GPa was chosen for the base material. The parameters used in Eqs. (6.10), (6.11) and (6.12) are given in Table 6.1.

Plots displaying the meta-material moduli as a function of member thickness t for structure 3 are shown in Figures 6.16, 6.17 and 6.18. (Full results are given in Appendix C.) All three plots display similar trends. First, it is clear that the homogenization and volume averaging models are in strong agreement, as an 8x8 UC volume has been utilized for the volume averaging analysis. However, the analytical honeycomb formulae only agree with the numerical models for those geometries with smaller member thicknesses; the 2 mm

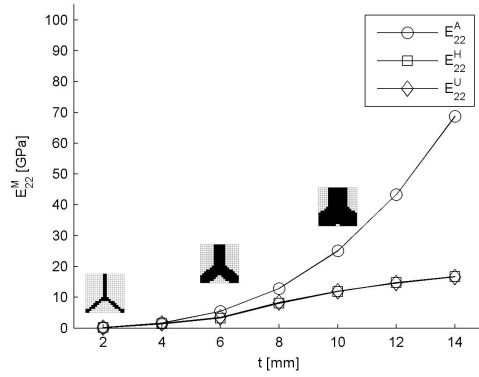


Figure 6.16: Plot of analytical and numerical E_{22}^M moduli as a function of member thickness in honeycombs.

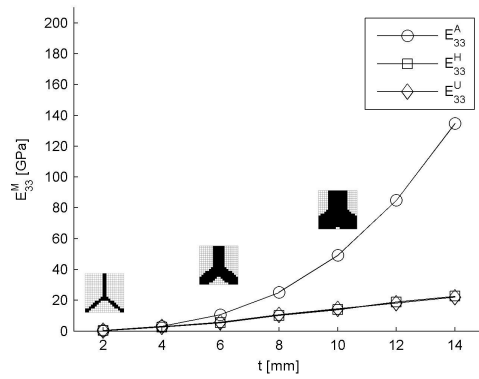


Figure 6.17: Plot of analytical and numerical E_{33}^M moduli as a function of member thickness in honeycombs.

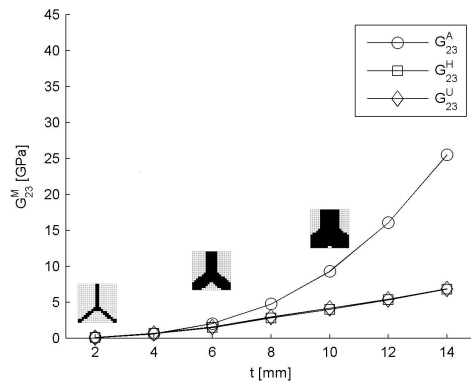


Figure 6.18: Plot of analytical and numerical G_{23}^M moduli as a function of member thickness in honeycombs.

Table 6.1: Parameters Used For the Analytical Comparison of Honeycombs in the Equations Given by Gibson et. al [95]

Structure	θ [rad]	l [mm]	h [mm]	Range of thickness t [mm]
1	0	10.00	19.5	2.00-14.00
2	0.3367	10.59	16.50	2.00-14.00
3	0.6107	12.21	13.00	2.00-14.00
4	0.8330	14.87	9.00	2.00-14.00
5	0.9505	17.20	6.00	2.00-14.00
6	1.107	22.36	0.00	2.00-14.00

and 4 mm geometries are in agreement, and divergence of the numerical models from the analytical model begins around 6 mm. As the UCs become more fully filled, the numerical models demonstrate a converging trend, whereas the analytical formulae do not.

The answer to the question as to which models are more accurate is apparent. As these plots are functions of thickness, this makes sense, as all of the analytical formulae are cubic in thickness t , and in the limit that $t \rightarrow \infty$, $E_k^A \rightarrow \infty$ in each case. Additionally, the maximum meta-material Young's modulus must be less than the material Young's modulus, $E_k^M \leq E_s$ for $k = 22, 33$, and the corresponding maximum shear modulus is bounded by the relation $G_{23} \leq \frac{E_s}{2(1+\nu_s)}$, where ν_s is the Poisson ratio of the base material. The analytical formulae clearly violate these bounds (30 GPa) for E_{22} and E_{33} at larger values of t while the numerical models do not; using the worst-case Poisson ratio $\nu_s = 0$, the maximum meta-material shear modulus is 15 GPa, which is violated by the analytical formula but not by the numerical models. However, the honeycomb models, derived from elementary beam theory, are known to decrease in accuracy rapidly for $\frac{t}{l} \geq \frac{1}{4}$ [95].

Given the numerical model (homogenization and volume averaging) agreement for thin membered honeycombs with analytical honeycomb calculations that have been validated experimentally, the agreement between homogenization and volume averaging in the asymptotic (small parameter expansion) homogenization limit (demonstrated in Section 6.2), and the satisfaction of upper bounds on meta-material moduli for the numerical models, it can be concluded that the use of non-simple, periodicity lattices is an accurate

alternative to discretize the global design domain into UCs. With accurate analysis methods in place, the optimization methods introduced in Chapter 5 can be extended to the design of non-simply connected materials.

6.4 Topology Optimization of Non-Simply Connected Structures

The topology optimization problem

$$\begin{aligned}
 & \min_{\mathbf{x}} V(\mathbf{x}) & (6.13) \\
 \text{s.t. } & h_k(\mathbf{x}) = E_k^M(\mathbf{x}) - E_k^* = 0 \text{ for } k \in \{1, 2, \dots, r\} \\
 & g_i^1(x_i) = x_i - 1 \leq 0, \forall i \in \{1, 2, \dots, n\} \\
 & g_i^2(x_i) = -x_i \leq 0, \forall i \in \{1, 2, \dots, n\}
 \end{aligned}$$

was implemented in MATLAB using the homogenization and volume averaging analyses presented in Sections 6.2 and 6.3. Two-dimensional, four-node, linear-elastic, isotropic, plane-stress elements with with Young's modulus $E = 30$ GPa and Poisson's ratio $\nu = 0.3$ were again used for the FEA of a single UC using homogenization and a 12x2 grid of UCs for the volume averaging analysis. 20x20 element discretizations were used for each UC. A number of target moduli were used to target E_{22}^M , E_{33}^M and G_{23}^M using both homogenization and volume averaging methods.

Numerical and visual results for optimization with homogenization are given in Table 6.2 and Figure 6.19. By looking at the numerical results, it appears that the lower-valued modulus targets (which result in thin-members geometries) perform better than the higher-valued targets. For example, for the two optimization runs with targets $E_{22}^* = 6$ and 9 GPa, the optimizations terminated in numerically convergent solutions, achieving the desired moduli. However, the optimization run with target $E_{22}^* = 18$ GPa terminated early, stopped by reaching the maximum number of 1000 function evaluations. (The E_{33} and

Table 6.2: Numerical Results For Optimization of a Non-Simply Periodic Structure Using Homogenization

Def. Mode	E_k^* [GPa]	E_k^H [GPa]	V	Comp. Time [s]	Iter.	Func. Eval.
E_{22}	6	5.999	0.223	392.4	102	259
E_{22}	9	9.000	0.350	310.0	124	418
E_{22}	18	2.844	0.452	2643.3	95	1001
E_{33}	6	6.000	0.246	475.1	127	375
E_{33}	9	9.000	0.347	668.0	158	563
E_{33}	18	17.979	0.715	500.9	148	1001
G_{23}	1	0.999	0.332	201.8	82	227
G_{23}	2	2.001	0.411	196.7	79	199
G_{23}	6	5.993	0.777	554.2	107	1001

G_{23} optimization runs resulted in similar convergence behaviors.) The visual results also display similar issues: the thinner-barred geometries are or are close to SIMP convergent, while the higher targets either did not achieve their target modulus or did not reach SIMP convergent solutions at all.

Table 6.3: Numerical Results For Optimization of a 12x2 Non-Simply Periodic Structure Using Volume Averaging

Def. Mode	E_k^* [GPa]	E_k^U [GPa]	V	Comp. Time [s]	Iter.	Func. Eval.
E_{22}	6	6.001	0.227	5153.6	144	432
E_{22}	9	8.993	0.340	13337.0	194	1001
E_{22}	18	17.999	0.627	4002.4	92	327
E_{33}	6	5.999	0.243	5428.6	130	398
E_{33}	9	8.999	0.349	7569.7	175	635
E_{33}	18	8.534	0.716	6971.3	46	277
G_{23}	1	1.001	0.320	2418.5	73	203
G_{23}	2	2.000	0.455	7482.2	154	627
G_{23}	6	5.999	0.830	2788.1	48	247

The numerical and visual results for the optimization of the 12x2 non-simply periodic structure using volume averaging are shown in Table 6.3 and Figure 6.20. The numerical results show similar issues to that of the homogenization optimization: the optimizer has more success at finding lower-modulus materials with correspondingly thinner-member

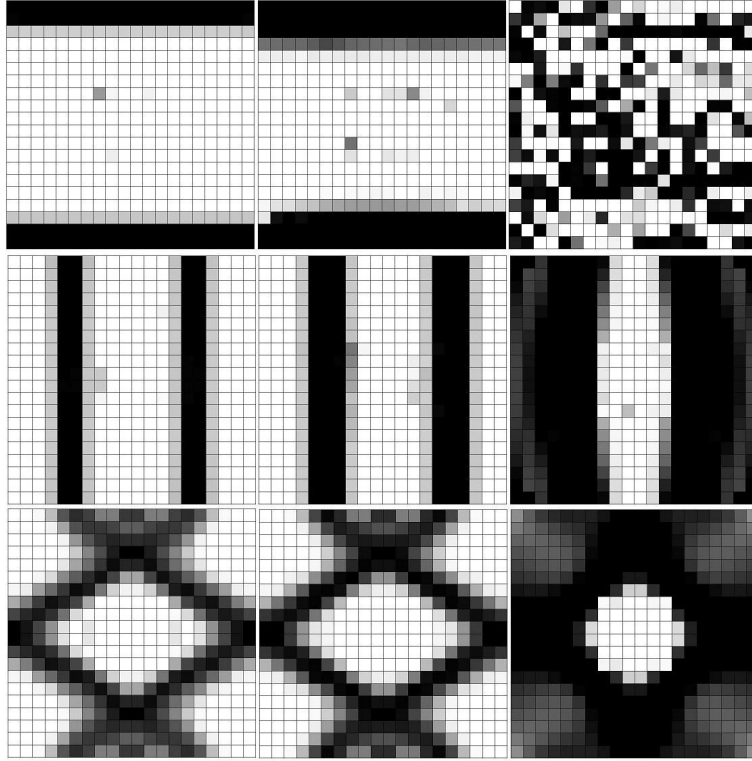


Figure 6.19: Results for the optimization of a non-simply periodic structure using homogenization with target moduli $E_{22}^* = 6$ GPa, 9 GPa and 18 GPa from top left to top right, with target moduli $E_{33}^* = 6$ GPa, 9 GPa and 18 GPa from center left to center right, and with target moduli $G_{23}^* = 1$ GPa, 2 GPa and 6 GPa from bottom left to bottom right. Numerical results are given in Table 6.2.

geometries. The E_{33}^* optimizations with targets 6 and 9 GPa were successful, but the optimizer became trapped in a local minimum for the 18 GPa target, unable to achieve the target modulus. Also, similar to the homogenization optimization, the visual results show that SIMP convergence was easier to attain in thinner geometries. One more interesting effect occurred in the optimization targeting $G_{23}^* = 2$ GPa. The non-simple connectivity of the structure appears to have pushed the optimizer to break the 22-symmetry and 33-symmetry of the optimization problem. Convergent solutions for most problems, regardless of the periodicity of the UCs, have maintained at least one plane of symmetry, but this is a rare example where both symmetries have been broken for a convergent solution.

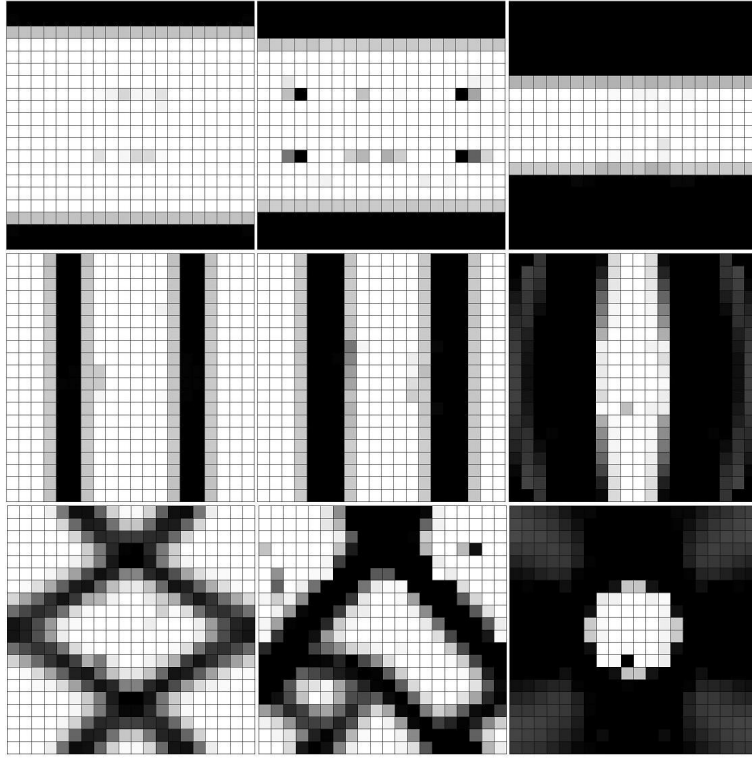


Figure 6.20: Results for the optimization of a non-simply periodic 12x2 UC structure using volume averaging with target moduli $E_{22}^* = 6$ GPa, 9 GPa and 18 GPa from top left to top right, with target moduli $E_{33}^* = 6$ GPa, 9 GPa and 18 GPa from center left to center right, and with target moduli $G_{23}^* = 1$ GPa, 2 GPa and 6 GPa from bottom left to bottom right. Numerical results are given in Table 6.3.

Full results for both analysis and optimization methods are reported in Appendix C. On the whole, a comparison of the two methods when a non-simply connected structure is used appears similar to that of the simple periodic structures. In particular, the homogenization analysis and optimization method is faster than volume averaging. However, both methods produce numerically and SIMP-convergent geometries for a large number of problems. For those optimization problems that are unable to converge, remeshing of the design domain to a larger number of elements will generally produce convergent results. Thus, for those problems in which homogenization is accurate, that particular method should be employed, while the volume averaging method should be employed for those cases in which

homogenization assumptions are not met.

6.5 Summary

In this chapter, a method was presented for the analysis of honeycomb and other structures that can be divided into non-simply connected lattices of rectangular UCs. A mathematical and physical basis for the correct the boundary conditions for each method was provided, and then analyses were shown to demonstrate the same trends as lattices with simple connectivity: both methods are accurate when the homogenization limit is met, but only the volume averaging method is accurate for materials using single layers. Numerical validations of the analyses were presented next using well-established equations that predict the meta-material properties of thin-membered honeycombs. Finally, topology optimization problems were using these analyses were shown to produce topologically and numerically useful results for large set of test problems. Given mathematical, physical and numerical validation, these methods can be used to design structures with non-simple connectivity.

Chapter 7

Meta-Material Design of the Shear Beam of a Non-Pneumatic Wheel

In this chapter, the topology design of the shear beam for the non-pneumatic wheel is presented using the methods presented in the preceding chapters of this work. First, the design parametrization from the top to the bottom level of the meta-material process and the corresponding feasible design space are described for the shear beam. The optimization setup and results are described for the design of the shear beam using different base materials and unit cell parameterizations in terms numbers of layers and connectivity. Finally, a discussion and summary of the results of the design study are given.

7.1 Design Study Parametrization

The method used to design the shear beam of the non-pneumatic wheel is a two-level process (Fig. 7.2). The top level (system-level) analysis optimization of the wheel is presented in the conference paper by Thyagaraja et al. [13]. The goal of the system-level optimization, with the design variables DV given in Table 7.1, was to identify one or a set of optimal designs in which the elastomeric shear beam is designed with a linear elastic material. Then, the hysteretic energy loss in the material of the shear beam undergone

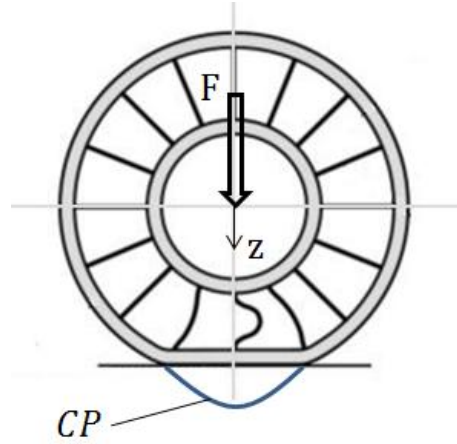


Figure 7.1: Depiction of non-pneumatic wheel optimization variables. F is an applied force to the central hub that displaces downward with displacement z . The contact pressure CP profile with the ground is used in the inequality constraints g_i .

during the cyclic loading and unloading of the beam during tire rotation will be reduced or eliminated altogether. This optimization problem is written as

$$\begin{aligned}
 \min_{DV} \quad & (\gamma_{SL}^* - \max(\gamma_{SL})) & (7.1) \\
 \text{s.t.} \quad & g_1 = CP - 414 \text{ kPa} \leq 0, \\
 & g_2 = 207 \text{ kPa} - CP \leq 0, \\
 & g_3 = \max(CP) - 448 \text{ kPa} \leq 0 \\
 & DV \in \Omega
 \end{aligned}$$

where γ_{SL} is the shear strain of the shear layer, and the constraints on the average and maximum contact pressure CP are required for vehicle performance and road wear purposes. The design variables and constraint parameters are shown in Figure 7.1. A large target shear strain γ_{SL}^* , 10%, is desired to closely mimic the large deformation capabilities of elastomers.

First, a sensitivity analysis of the non-pneumatic wheel model was completed, demonstrating that the shear layer thickness $sThk$ and shear modulus G_{23} were the most influential design variables for the system optimization. Because the finite element model

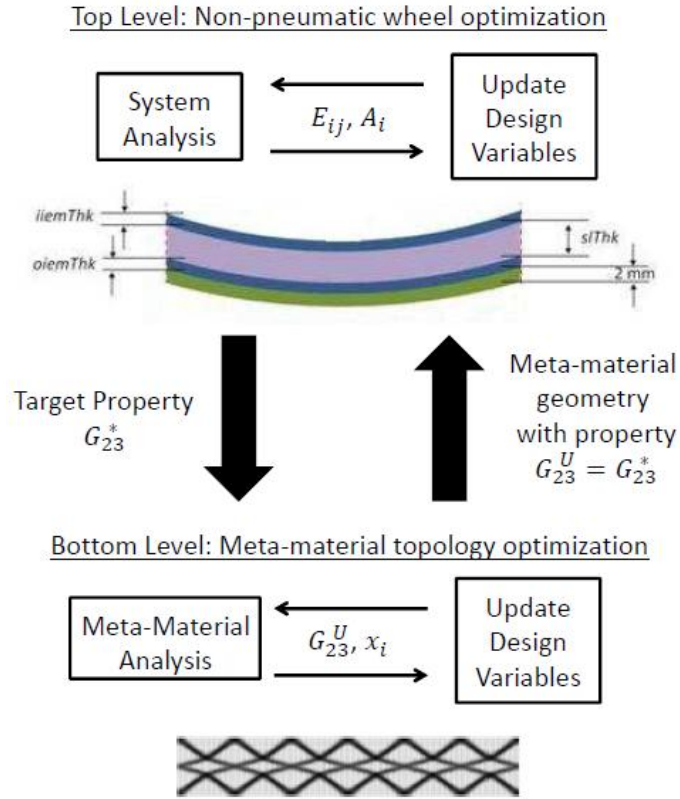


Figure 7.2: Two-level optimization process used for meta-material design of the shear beam of the non-pneumatic wheel.

used to simulate the wheel is large and computational costly to solve for the static loading, a neural networks approach was used to generate a meta-model, and the non-dominated sorting genetic algorithm (NSGA-II) was used to optimize on the model. The solutions of the optimization of the orthotropic shear layer were found to lie on the hyperbolic curve

$$G_{23} \cdot sThk = 67 \text{ MPa} \cdot \text{mm} \quad (7.2)$$

within the bounds of shear layer thickness $5\text{mm} \leq sThk \leq 12\text{mm}$ and corresponding shear modulus $5.5 \text{ MPa} \leq G_{23} \leq 14 \text{ MPa}$ (Fig. 7.3).

Table 7.1: Design variables and bounds used in the non-pneumatic wheel optimization [13]

Design Variable	Lower Bd.	Upper Bd.
shear layer thickness	4 mm	12 mm
inner inext. membrane thickness	0.1 mm	1 mm
outer inext. membrane thickness	0.1 mm	1 mm
shear layer Young's modulus	1 MPa	750 MPa
shear layer Young's modulus	1 MPa	750 MPa
shear layer shear modulus	3 MPa	20 MPa
shear layer Poisson's ratio	-0.99	0.99

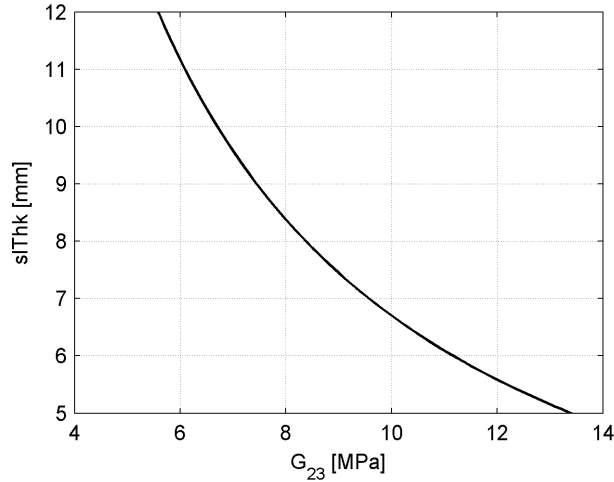


Figure 7.3: Set of optimal solutions potentially targeted for the design of the meta-material shear layer.

7.2 Topology Optimization of the Shear Layer

Given the results of the system optimization, the meta-material (bottom-level) topology optimization was attempted using three different elastic base materials: polycarbonate (PC) with Young's modulus $E = 2.7$ GPa and Poisson's ratio $\nu = 0.42$, mild steel with $E = 210$ GPa and $\nu = 0.29$, and aluminum 7075-T6 with $E = 70$ GPa and $\nu = 0.33$. For different values of the shear layer thickness $slThk$, the shear modulus G_{23}^* to be targeted was computed using Eqn. 7.2.

The physical dimensions of the shear layer, being very small (5-12 mm in thickness),

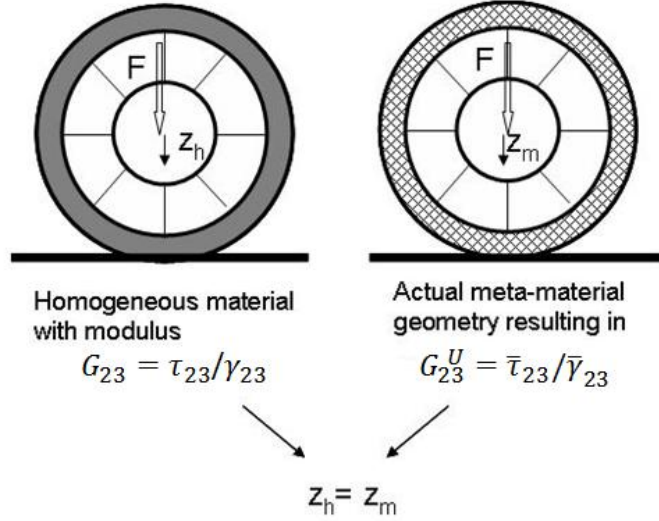


Figure 7.4: Meta-material tie requirements for the non-pneumatic wheel design. The tie exists only if the displacements z_m and z_h are equal.

place a realistic manufacturing constraint on any meta-material designed for the shear layer. This constraint allows the inclusion of only one or a few layers of unit cells. In Chapter 3, it was shown that the homogenization process for analyzing unit cells for single layer materials is not accurate when incorporated into the global design process. However, by using the volume averaging method to analyze meta-material properties, the integrity of the meta-material design process is maintained, as properties analyzed with the averaging method are accurate at the global design level. This means that the system at the top level behaves in the same way when simulated using the homogeneous material with assigned meta-material properties and the actual meta-material structure (Fig. 7.4). For example, a load F is applied to the central hub of the wheel with the meta-material shear beam, resulting in hub displacement z_m . When the meta-material is substituted with a homogeneous material with the same material properties as the meta-material, the central hub, subjected to load F , should experience the same displacement, $z_h = z_m$. Failure in this tie between the levels would invalidate the overall meta-material design process.

Optimization using the volume averaging analysis as described in Chapter 5 was utilized. The solid isotropic microstructure with penalization (SIMP) method was used to

interpolate the material onto the finite elements of the design domain [52], and a mesh-filter, commonly used to prevent numerical issues such as checkerboarding and one-node connected hinges was implemented. Given to the discussion in Chapter 4, the optimization problem was formulated as

$$\begin{aligned}
 & \min_{\mathbf{x}} \quad V(\mathbf{x}) & (7.3) \\
 & \text{s.t. } h(\mathbf{x}) = G_{23}^U(\mathbf{x}) - G_{23}^* = 0 \\
 & \quad x_i^s \in [x_{min}, 1], \text{ for } i = 1, 2, \dots, n
 \end{aligned}$$

where $V \in [0, 1]$ is the volume fraction of the unit cell, G_{23}^U is the shear modulus of the material given by the volume averaging analysis, G_{23}^* is the target shear modulus, s is the SIMP exponent, x_i is design variable i , and n is the number of elements in the unit cell.

7.2.1 Design Using Simple Connectivity

The design process of the wheel using simple connectivity proceeded along the following path and is reported here in this order. First, topology optimization using the three base materials was completed using low-resolution (30x30 elements) discretizations for the unit cell with a varied number of layers of unit cells. The goal of this was to obtain a set of designs that achieve or come close to achieving SIMP convergence while attaining the target shear modulus G_{23}^* , as well as to identify those base materials that are not capable of doing so. Then, for those designs that were successful, a high-resolution (40x40 elements) refinement of the design optimization problem was attempted from four different initial design points, and satisfactory, convergent designs were identified.

7.2.1.1 Optimizations Using a Low-Resolution (30x30 elements) Mesh

For the 30x30 discretizations of the unit cell, design domains with 12 unit cells along the length of the shear layer and either one or two layers along the thickness *sThk* were optimized on using each of the three previously mentioned base materials. Plane stress

Table 7.2: Low-resolution optimization results

s/Thk [mm]	base material	layers	G_{23}^U [GPa]	V
5	PC	1	13.38 ^{†,‡}	0.146
5	PC	2	13.40 [‡]	0.157
6	PC	1	11.17	0.141
6	PC	2	11.17	0.149
7	PC	1	9.57	0.190
7	PC	2	9.57 [‡]	0.150
8	PC	1	8.38	0.181
8	PC	2	8.38	0.153
9	PC	1	7.44	0.136
9	PC	2	7.44	0.123
10	PC	1	6.67 ^{†,‡}	0.117
10	PC	2	6.70	0.130
11	PC	1	6.09	0.117
11	PC	2	6.09 [‡]	0.159
12	PC	1	5.58 [‡]	0.115
12	PC	2	5.58	0.112
7	AL	1	9.57	0.067
8	AL	1	8.38	0.043
8	AL	2	8.34 [†]	0.060
9	AL	2	7.44	0.052
11	AL	1	6.09	0.039




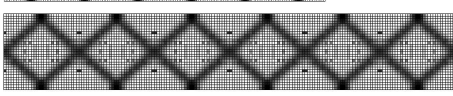
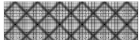


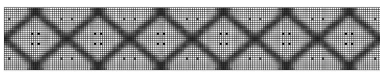
[†] Optimization terminated early by exceeding allowed number of function evaluations.

[‡] Material depicted in Table 7.3.

elements with thickness equal to 200 mm (the in-plane thickness of the non-pneumatic wheel model) were used. A SIMP exponent $s = 3$ was used to generate the low-resolution designs. The termination parameters used for the optimization were an objective tolerance equal to 10^{-4} on the volume fraction and a constraint tolerance equal to 10^{-3} MPa on the shear modulus. Early termination parameters of 200 algorithm iterations and 1000 function evaluations were also given. The optimizations for which feasible designs, those that appeared to generate resolved geometries while obtaining the goal modulus G_{23}^* , are reported in Table 7.2, while several of these materials designs are depicted in Table 7.3.

No convergent solutions were obtained from the optimization attempts using mild

Table 7.3: Selected visual results for optimizations using 30x30 unit cell discretizations

G_{23}^U [MPa]	Single-Layer Polycarbonate (PC) Material
13.38	
11.17	
6.67	
5.58	
G_{23}^U [MPa]	Two-Layer Polycarbonate (PC) Material
7.44	
6.09	
G_{23}^U [MPa]	Single-Layer Aluminum 7075-T6
8.34	
6.09	

Six unit cells are shown in the horizontal direction for each material.

steel. Additionally, only a few of the optimization attempts using aluminum 7075-T6 were successful in achieving the desired shear moduli. The shear moduli of both mild steel and the aluminum alloy are three to four orders of magnitude higher than the target moduli required for the shear layer design. However, the majority of the optimization attempts using PC as a base material resulted in shear moduli with or very near the target moduli; PC has a shear modulus two to three orders of magnitude larger than the target shear moduli. From these results, it became apparent that there is a realistic upper bound for base materials that can be used in this design process. While metals were one of the original groups of materials hypothesized to satisfy the design requirements of the meta-material shear layer, they were eliminated by this low-resolution optimization study. However, polymers, PC in particular, appear to achieve these design requirements.

As for the optimization process itself, the existence of an upper bound on materials

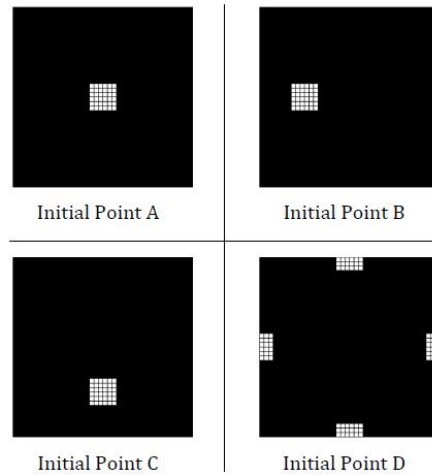


Figure 7.5: Initial points used for the high-resolution design of the meta-material shear layer.

serves to provide validation of the numerical accuracy of the method, requiring realistic materials to be used to achieve a feasible meta-material solution. The figures in Table 7.3 also provided some guidance on the engineering process and tuning of the optimizer for the high-resolution optimizations. Simple ‘x’ or diamond structures appear in the majority of the feasible solutions, indicating this geometry is local topological minimum for design in shear. This is consistent with the optimal solutions of other materials optimized in shear using homogenization methods (e.g., those found in Zhang et al. [19]), validating the topological design methods used. However, with the exception of the two top-most geometries in Table 7.3, the finite element densities of the solutions of the included elements are not very close to 1; many are in the range (0.3,0.6). This results in blurry visual solutions, as well as a loss of fidelity in the numerical results. This issue would have to be corrected in further optimization studies to produce numerically accurate results.

7.2.1.2 Optimizations Using a High-Resolution (40x40 elements) Mesh

For the the high-resolution optimization attempts, 40x40 element discretizations of the unit cell were used. As single-layer optimizations appeared to produce the best results (aside from the aforementioned SIMP-convergence issue), optimization attempts

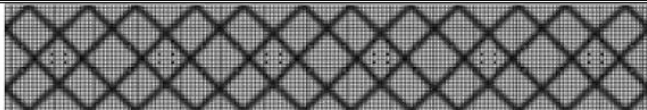
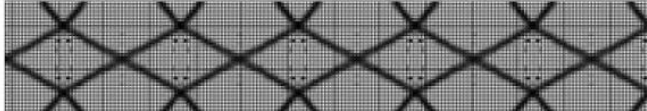



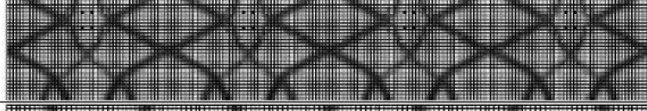


$slThk$ [mm]	G_{23}^U [MPa]	V	Material
5	13.40	0.179	
6	11.70	0.129	
7	9.57	0.165	
8	8.37	0.136	
9	7.44	0.171	
10	6.70	0.172	
11	6.09	0.150	
12	5.58	0.115	

Figure 7.6: Simply connected meta-materials generated from initial point A.

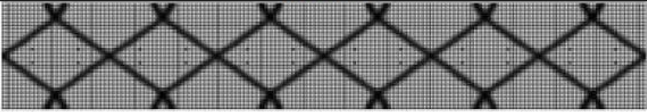


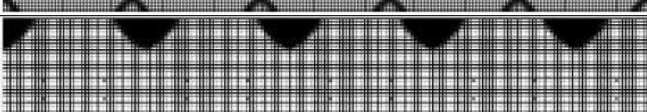
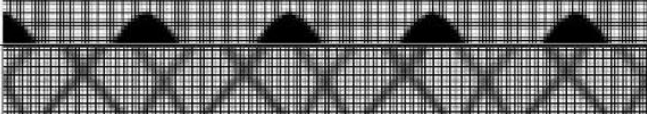
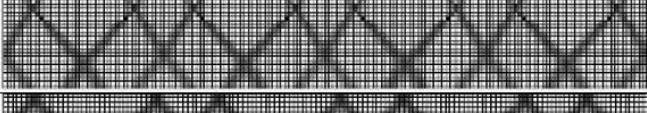


$slThk$ [mm]	G_{23}^U [MPa]	V	Material
5	13.40	0.125	
6	11.70	0.175	
7	9.57	0.104	
8	8.37	0.138	
9	7.44	0.149	
10	6.67	0.138	
11	6.09	0.161	
12	5.58	0.128	

Figure 7.7: Simply connected meta-materials generated from initial point B.




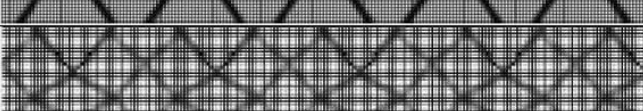

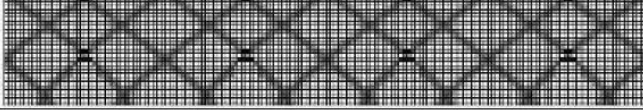

$slThk$ [mm]	G_{23}^U [MPa]	V	Material
5	13.40	0.114	
6	11.70	0.214	
7	9.57	0.102	
8	8.37	0.147	
9	7.44	0.145	
10	6.70	0.169	
Optimization was not successful in obtaining a solution.			
12	5.58	0.133	

Figure 7.8: Simply connected meta-materials generated from initial point C.

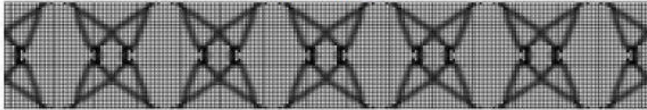
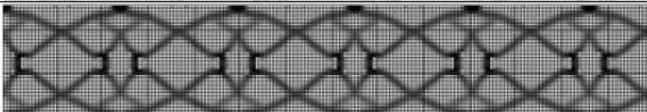




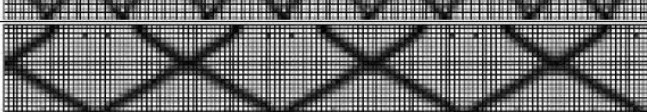
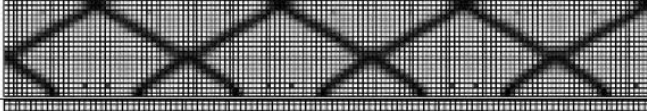
$slThk$ [mm]	G_{23}^U [MPa]	V	Material
5	13.40	0.177	
6	11.70	0.210	
7	9.57	0.161	
8	8.37	0.156	
9	7.44	0.146	
10	6.70	0.123	
11	6.09	0.676	
12	5.58	0.676	

Figure 7.9: Simply connected meta-materials generated from initial point D.

using the high-resolution mesh were restricted to single-layer materials with 10 unit cells in the analysis domain. Only PC was used as a base material for the high-resolution studies. The same termination parameters as those used in the low-resolution optimizations were used here. To attempt to solve the SIMP-convergence issue, the SIMP exponent was increased to $s = 4$. Because of the dependence of the topology optimization algorithm on the initial point, and because a number of feasible solutions were desired, four different initial points (Fig. 7.5) were used for each of these optimizations. (Recall from Chapter 2 that the topology optimization problem has many local minima with non-unique solutions; by choosing different initial points, the optimizer may converge on a different minimum of the problem.)

The resulting materials are depicted in Figs. 7.6 to 7.9. The first thing to notice is variety of topologies, in general and within one group of initial points. For example, for those materials generated from initial point A, the microstructure generated with $G_{23}^U = 13.4$ MPa is similar to the diamond structures generated in many of the low-resolution designs, while the microstructures with $G_{23}^U = 11.17$ MPa and 5.58 MPa are very similar. There are also some microstructures that did not generate feasible microstructures by either not achieving SIMP convergence (e.g., the $G_{23}^U = 6.70$ MPa geometry from initial point A) or lacking connectivity (e.g., the $G_{23}^U = 8.37$ MPa geometry from initial point B).

More importantly, many of these geometries resulted in SIMP-convergent, feasible microstructures while achieving the target moduli. These are presumed to be due to the use of higher-resolution meshes and the utilization of the larger SIMP exponent. These results are displayed on the curve generated from Eqn. 7.2 in Fig. 7.10.

7.2.2 Design Using Non-Simple Connectivity

The topological design of a non-simply connected shear layer using the volume averaging analysis, described in Chapter 6, was used to generate material designs for the shear layer. Because the mild steel and aluminum materials were ruled out as potential base materials in Section 7.2.1, PC was used as a base material for the 40x40 discretizations of

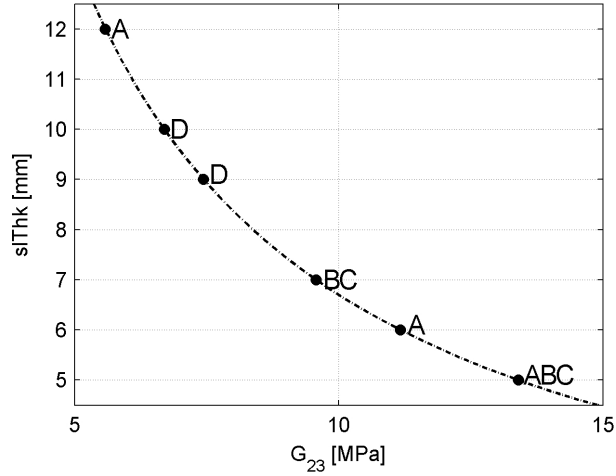


Figure 7.10: Feasible design results from high-resolution optimization study. The dashed line indicates the optimal results, Eq. 7.2, from the top-level optimization of the wheel, and the letters on the plot indicate which initial point(s) was used to generate a meta-material design at that point.

the UCs comprising the material. For the shifted connectivity to be effective, at least two layers of UCs had to be considered. However, manufacturing limits should limit the utility of the code to only two to three layers at most, where the 12 mm shear band contains layers 4 mm in thickness with three layers, while the 5 mm shear band contains layers 2.5 mm in thickness. For these reasons, problems with two layers of UCs with horizontal offset $L/2$ were considered. The same shear layer thicknesses and starting points used in the high-resolution studies presented in Section 7.2.1 were used here.

The results from these high-resolution optimizations are displayed in Figures 7.11 to 7.14. A number of optimizations either did not generate a geometry or did not generate a well-resolved, SIMP-convergent geometry. Additionally, some well-resolved results are not feasible, as they do not connect the lower and upper portions of the design domain; these include the 13.40 MPa and 6.70 MPa geometries from initial point A, the 8.37 MPa and 7.44 MPa geometries from initial point D, and the not fully-resolved results in the 11.70 MPa and 5.58 MPa results from initial point C.

More importantly, there are two classes of convergent results that emerged from

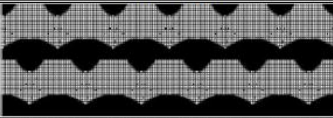


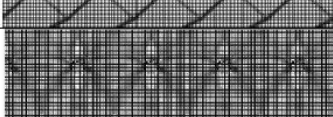
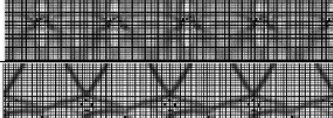
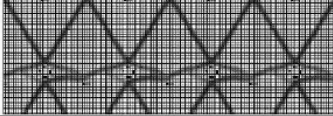
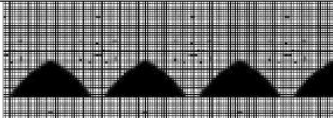
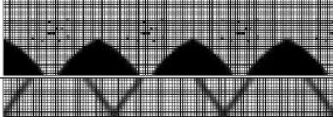
$slThk$ [mm]	G_{23}^U [MPa]	V	Material
5	13.40	0.407	
6	11.70	0.117	
7	9.57	0.102	
8	8.37	0.303	
9	7.44	0.137	
10	6.70	0.212	
11	6.09	0.147	
12	5.58	0.054	

Figure 7.11: Non-simply connected meta-materials generated from initial point A.

$slThk$ [mm]	G_{23}^U [MPa]	V	Material
5	13.40	0.080	
6	11.02	0.141	
7	9.57	0.121	
8	8.43	0.064	
9	7.44	0.111	
10	6.70	0.060	
Optimization was not successful in obtaining a solution.			
12	5.58	0.101	

Figure 7.12: Non-simply connected meta-materials generated from initial point B.

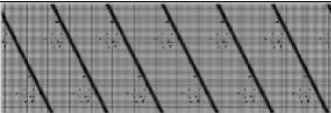
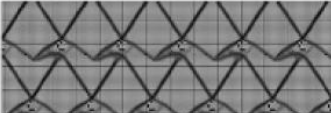
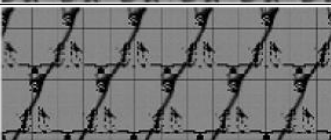
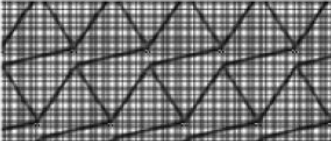
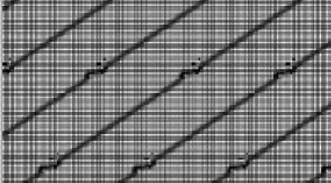
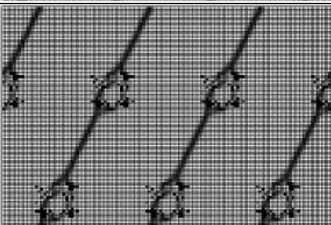
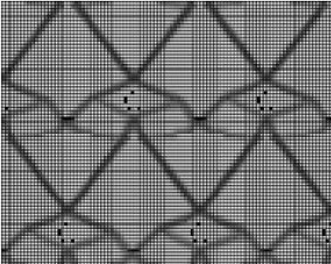
$slThk$ [mm]	G_{23}^U [MPa]	V	Material
5	13.40	0.072	
6	11.70	0.144	
7	9.52	0.148	
8	8.38	0.115	
Optimization was not successful in obtaining a solution.			
10	6.70	0.077	
11	6.09	0.093	
12	5.58	0.131	

Figure 7.13: Non-simply connected meta-materials generated from initial point C.

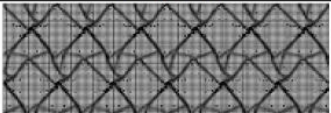
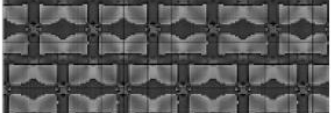


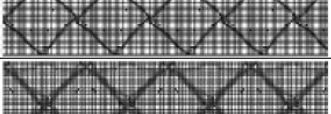



$sThk$ [mm]	G_{23}^U [MPa]	V	Material
5	13.40	0.169	
6	11.70	0.411	
7	9.57	0.128	
8	8.37	0.105	
9	7.44	0.163	
10	6.70	0.117	
11	6.09	0.133	
12	5.58	0.110	

Figure 7.14: Non-simply connected meta-materials generated from initial point D.

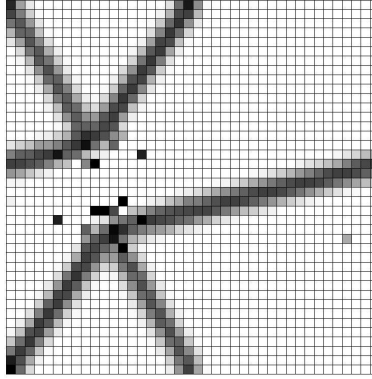


Figure 7.15: Unit cell from the auxetic honeycomb structure with $G_{23}^U = 9.57$ MPa.

these optimizations. First, a bristle-like structure (at varying angles with respect to vertical) that are displayed in the 5.58 MPa result from initial point A, the 13.40 MPa, 8.43 MPa and 6.70 MPa results from initial point B, and the 13.40 MPa and 6.70 MPa results from initial point C. Geometries of this type were previously investigated by Lowe et al. [12], as was discussed in the motivation for this research of Chapter 1. This class of geometry was shown to be a bit too simplistic, displaying buckling as the bristles passed from one side of the contact patch through to the other during cyclic loading of the wheel. This buckling was associated with failure of the geometry.

The other class that emerged was an auxetic honeycomb structure, best displayed in the 9.57 MPa result from initial point A, the 9.57 MPa and 5.58 MPa result from initial point B, and the 8.38 MPa result from initial point C. The UC of the 9.57 MPa geometry from initial point B is shown in Figure 7.15. The UC displays one very interesting characteristic: the top of the UC is not connected to the bottom of the UC with a structural member; instead, there are two independent, three-member structures in two corners of the UC. Interestingly, the periodicity and connectivity of the global structure permits this to be the case. The auxetic honeycomb has been studied extensively as a potential geometry for use in the shear layer of the wheel.

The feasible results using the high-resolution mesh for the study presented using

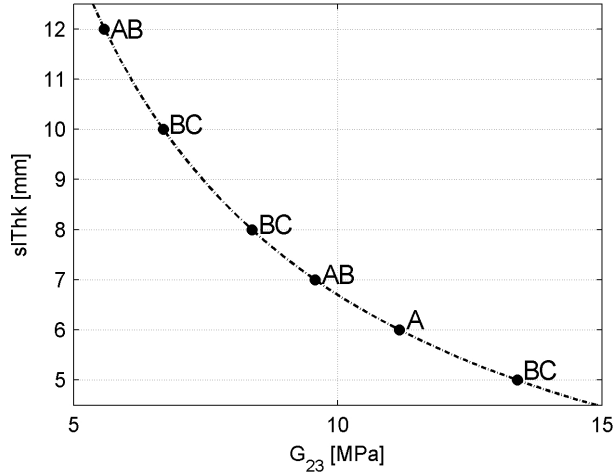


Figure 7.16: Feasible design results from high-resolution optimization study using non-simple connectivity. The dashed line indicates the optimal results, Eq. 7.2, from the top-level optimization of the wheel, and the letters on the plot indicate which initial point(s) was used to generate a meta-material design at that point.

two-layers of UCs are summarized in Figure 7.16.

7.3 Discussion

While an argument could be made that simultaneous optimization of the shear layer microstructure and the shear band itself within the global finite element model of the wheel, two complications would arise when attempting this all-at-once approach. First, implementing a topology optimization routine directly into the global optimization problem is computationally costly. The large computational cost of the system analysis of the wheel using a homogeneous orthotropic material necessitated using an approximation with neural networks to generate a meta-model. If a topology optimization routine were to be directly integrated, a much finer mesh than the one used for the shear layer material in the global model would have to be included. Second, a genetic algorithm was used to determine the set of optimal solutions when using the meta-model, while topology optimization methods that utilize continuous material interpolation methods are typically better suited for use with deterministic algorithms, especially when closed-form design sensitivities are given. This is

the case here. (While a genetic algorithm was employed, a gradient based algorithm could have been used for the global optimization problem.) Both of these issues are alleviated by decoupling the design process as presented, allowing for the use of an optimization algorithm on each level. This placed the burden of meta-material design on the more appropriate platform of topology optimization without confounding factors from the global model.

From these numerical and visual results given here, it can be seen that the method used for topology optimization that utilizes the volume averaging analysis for single or few-layered materials is capable of generating materials with prescribed linear elastic properties. A number of feasible designs were produced with the target shear moduli and shear layer thickness required by the top-level optimization of the shear layer. The next steps of the design process are selection of a meta-material geometry and implementation into the finite element model of the non-pneumatic wheel to investigate global convergence of the meta-material design process (as depicted in Figure 7.4) and failure properties of the meta-material via the von Mises or other failure criteria. Additionally, experimental validation of elastic and failure properties of those geometries selected for the shear layer should be completed.

These geometries were designed to be optimal in a shear loading, subject to no constraints on other material properties (e.g., the meta-material Young's modulus). As the design sensitivities needed for the topology optimization are functions of the compliance of the structure (see Chapter 5), by optimizing on the structure in shear, a geometry was produced such that the compliance of the structure in shear was also considered. Though the compliance was not necessarily at a minimum at optimality, the structures produced, especially those with an 'x'-like geometry, are certain to have better compliance properties in shear than other structures. The repeated appearance of these 'x'-like geometries as local minima of the optimization problems suggests this true. Additionally, these 'x' geometries are already known to be an optimal structure for materials deformed in shear when using simple connectivity [19].

The optimizations that resulted in a bristle design lend some credibility to the idea

that a simple design is preferable. The use of single-members to connect the top of the design domain to the bottom is simple to manufacture, while providing the desired shear moduli for the design domain. However, these members were found to demonstrate buckling in the contact patch, eliminating them from the set of feasible designs for the shear layer.

The auxetic honeycomb geometries obtained purely as a result of optimization of a material in shear by seeking minimum volume subject to a linear constraint on the meta-material shear modulus are remarkable. These geometries have been studied extensively, known for their negative Poisson's ratio and relatively low shear moduli when compared to that of the base material [18]. Further, Ju et al. [18] investigated the geometry for use in high-shear flexure, achieving approximately 15% effective shear strain prior to material failure when using the PC base material. The contact pressure of the wheel when using honeycomb geometries, including the auxetic structure, in the shear was investigated by Ju et al. [101]; the wheel with the auxetic honeycomb shear layers were shown to have lower maximum contact pressures when compared to the non-auxetic honeycomb shear bands.

7.4 Summary

The two-level design process described in the former chapters of this work was used for the meta-material design of the shear layer for the wheel. In the work by Thyagaraja et al. [11], the shear layer thickness and shear modulus were identified as the most sensitive parameters to the global design; the optimal set of designs was identified in the top-level optimization to lie on a hyperbolic curve that is a function of these two parameters. In this chapter, the bottom-level optimization consisted of designing meta-material geometries which lie on this curve using topology optimization. Because the thickness of the shear layer was very small, design using asymptotic homogenization analysis was not feasible, as realistic manufacturing constraints required inclusion of only one or a couple layers of unit cells in the shear layer. With more unit cells in this thickness, the internal microstructure of the unit cell would almost certainly not be manufacturable in a cost-effective manner

with current technology. Instead, the topology optimization method utilizing the volume averaging analysis was implemented.

A two-step process was used in the topology design of the meta-material microstructures. First, a low-resolution mesh was used to select feasible base materials, as well to identify optimization parameters (i.e., number of layers, meta-material tolerance, volume fraction tolerance, SIMP penalization, and other topology optimization parameters) that could be better tuned to produce convergent and usable results. In this process, a shear layer thickness was chosen, and the target shear layer modulus was identified using the optimal relationship curve produced in the top-level optimization. Then, a high-resolution mesh was used with different initial points to design a number of different structures, from which nine were identified as potential design candidates for use in the non-pneumatic wheel when using simply-connected UC structures. Additionally, the non-simply connected UC structures were used to generate a set of meta-materials, including the auxetic honeycomb. The final step of this process, which is outside the scope of this work, is to complete further modeling with these candidate geometries in the global model of the wheel for validation of the models, as well as numerical testing for mechanical elastic and failure properties.

Chapter 8

Concluding Remarks

The research questions posed at the beginning of this work were

1. Are there applications in which homogenization theory is not capable of predicting accurate meta-material moduli? If so, can the volume averaging method be used?
2. Can a well-posed meta-material topology optimization problem be constructed to target meta-material properties?
3. Is it possible to topology optimize with respect to the parameters of the volume averaging model?
 - Can a single unit cell be optimized in tension and in shear?
 - Can multiple unit cells be optimized in tension and in shear?
4. How does unit cell connectivity affect the physical modeling methods (asymptotic homogenization and volume averaging) presented?
5. Can the non-pneumatic wheel assembly design problem be solved using the volume averaging method with topology optimization?

Each of these questions is addressed below.

Item 1

Homogenization theory and volume averaging are known to predict similar values for meta-material properties in many cases. Homogenization theory, being based off a small parameter expansion, was shown to be accurate for the prediction of meta-material properties as long as that unit cell is small enough, relative to the global length scaling of the material, to justify its use. However, when this scaling assumption is not met, which is true of single and few-layered materials in particular, the two theories diverge. To demonstrate which theory, if either, is accurate, a simple design problem was posed to demonstrate accuracy or inaccuracy of these methods to predict meta-material properties within the two-level process. These conclusions of this analysis are listed below.

- Below the representative volume limit, neither homogenization nor volume averaging are accurate for representing meta-material properties within the context of material design.
- Beyond the representative volume limit, for materials in which the small-parameter scaling assumption of homogenization is met, both analysis methods predict similar meta-material properties and are accurate for material design.
- Beyond the representative volume limit, for those problems in which the small-parameter assumption of homogenization is not met in one or more dimensions (e.g., materials with only one or a few layers of unit cells, or materials with UCs that have a poorly scaled aspect ratio), volume averaging is accurate for material design, while homogenization is not.

Item 2

In Chapter 4, the Karush-Kuhn-Tucker and Fritz-John optimality conditions were derived for three different meta-material topology optimization problems using continuous material interpolation schemes. The problem seeking a minimum volume subject to a set of linear constraints on the material requirements was demonstrated to be mathematically well-posed

in every case, while other commonly used methods reported in the literature demonstrated mathematical and numerical issues at optimality.

Item 3

The results from the optimization of a materials in tension and in shear, as well as the results from the optimization of the wheel demonstrate that it is possible to optimize on the volume averaging model. This conclusion required addressing several issues.

- In Chapter 5, design sensitivities for a single unit cell were derived for design problems in tension and in shear. Topology optimization using the single unit cell model was not done due to the inaccuracy of the volume averaging model in the meta-material design process when using a single unit cell, as the RVE limit is not achieved in the single unit cell case. (This derivation was intended as a path to the derivation of design sensitivities for multiple unit cells.)
- The design sensitivities derived for a single unit cell were simply extended to the design of multiple unit cells using volume averaging, and optimization of materials in both tension and in shear was demonstrated in Chapter 5.

Item 4

The analysis and optimization of materials using non-simply connected unit cell structures was shown to be an accurate and feasible method for meta-material design in Chapter 6. Using such a connectivity requires no changes in the volume averaging analysis, and it requires only a small change in the periodic boundary conditions of the homogenization analysis. Additionally, in Chapter 7, the method was shown to increase the feasible design space by admitting a larger class of geometries, most remarkable of which is the auxetic honeycomb, as a result of minimizing the volume fraction of the material subject to linear constraints on the shear modulus.

Item 5

The methods presented in this work were used to design meta-materials for the shear layer of the non-pneumatic wheel. Notable geometries include the ‘x’ geometry, the bristle geometry

and the auxetic honeycomb geometry.

8.1 Contributions

The list of contributions to the engineering community in this work includes

- A clarification of the accuracies and inaccuracies of the components used in the meta-material design process.
- A clarification of the tie between the system-level optimization and meta-material topology optimization (consistency of the two-level meta-material design approach).
- The first in-depth derivation of optimality conditions for common meta-material optimization problems described in the literature.
- The first justification of the use of the volume averaging analysis in meta-material optimization, including first-order design sensitivities and numerical examples.
- A potentially simpler alternative to using non-rectangular unit cells with simple connectivity for meta-materials design by instead using non-simply connected, rectangular unit cells to represent the design domain.
- A number of feasible geometries suitable for use in the shear layer of the non-pneumatic wheel, subject to further validation of the model geometries for failure and fatigue properties.
- The first description of an auxetic honeycomb structure as being a minimal volume or weight structure optimal in shear deformation.

8.2 Discussion

The models and methods presented in this work were designed to be as general as possible while satisfying the needs of the design of the shear layer for the non-pneumatic

wheel. The meta-material analysis methods used have had no limiting assumptions placed on them in terms of physical applicability other than those expressed, and the optimization methods employed, namely topology optimization using continuously interpolated materials with SIMP penalization, are known to offer a more general class of solutions than those offered by non-continuous interpolation methods. These methods are among the simplest methods found in the literature used to analyze and solve meta-material design problems while maintaining wide applicability due to the general nature of the methods employed.

The models used to analyze materials can require the use of large amounts of computational resources to solve a single problem. This is primarily due to the need to solve large finite element problems at every iteration of the optimization. In this research, Clemson University's high performance computing (HPC) cluster, the Palmetto Cluster, was utilized to solve these large FEA problems, as well as the subsequent optimization problems. However, the system level models for which the meta-materials are designed for use in often require large computational resources to solve. (This is the case in this research, where the the global wheel model was also solved using the Palmetto Cluster.) Thus, these resources are typically already available to the designer.

The state of the art in meta-material design had previously left several open questions in both the analysis and design optimization of meta-materials in the context of a larger assembly. As such, this work has aimed at clarifying some of these issues, as well as providing a description of an example in which this process was used to design a meta-material for use in a larger assembly.

8.3 Future Work

Though the methods employed were general in nature, there are several areas in which this research could be furthered to benefit the material design optimization field.

8.3.1 Analysis and Optimization of Geometrically and Physically Non-Linear Materials

Homogenization theories are generally derived using a small parameter expansion to simplify the analysis domains of materials to a single unit cell. This includes the analysis of both geometrically non-linear (large displacement) and physically non-linear materials. Expanding the ideas presented here to materials other than linear elastic materials includes verifying the inaccuracy of homogenization and accuracy of another analysis method in these cases, as well as updating of the optimization methods used for design.

8.3.2 Multicriteria Design of Meta-Materials

In Chapter 4, the optimization problems posed were all multicriteria problems, requiring multiple material requirements be met at optimality. This chapter demonstrated the feasibility, or lack thereof, of each formulation to achieve a well-resolved (i.e., SIMP convergent) result at optimality while achieving multiple material requirements. However, the examples presented only demonstrated the single criteria, single objective cases of the formulations posed. The targeted design of multiple material properties simultaneously, for example both E_{22}^M and G_{23}^M , requires both material properties to be simultaneously feasible. The Hashin-Shtrikman bounds provide limits on the ranges of achievable meta-material moduli as a function of volume fraction of the material (see, for example, [102]). As such, they limit the ranges of simultaneously obtainable moduli. Questions remain as to the utility of different optimization formulations to target one material property while constraining another within a range, simultaneously.

8.3.3 Inclusion of Failure Properties

In all of the materials designed as a result of this work, failure properties were never considered directly in topology optimization. Instead, they are left for validation in the global model as a post-processing effort. The optimization methods presented directly address the stresses introduced as a result of particular mode of deformation, and optimiza-

tion should, in theory, provide a locally minimum strain energy design while meeting the design criteria. However, as von Mises stresses, buckling stresses or other criteria are never directly considered, these geometries could suffer failure from large strains placed on the meta-material geometries. Addressing these failure criteria on a unit cell level in the context of the meta-material design process remain an open question. Solving these seemingly obvious issues are at the forefront of meta-material design and are sure to revolutionize the field of material design, in general.

Appendices

Appendix A Comparison of Homogenization and Volume Averaging Analysis Methods

Below are numerical results for the analyses described and plotted in Chapter 3.

Comparison of Homogenized and Averaged Moduli for 8x8 Unit Cells for the ‘x’ Geometry

Bar Thickness (fraction of L)	$\frac{E_{22}^U}{E_{22}^H}$	$\frac{E_{33}^U}{E_{33}^H}$	$\frac{G_{23}^U}{G_{23}^H}$	Volume Fraction
0.05	1.171	1.171	1.002	0.281
0.10	1.105	1.105	1.003	0.441
0.15	1.041	1.041	1.004	0.700
0.20	1.024	1.024	1.005	0.800
0.25	1.005	1.005	1.004	0.940
0.30	1.002	1.002	1.002	0.980
0.35	1.000	1.000	1.000	1.000

Comparison of Homogenized and Averaged Moduli for 8x8 Unit Cells for the ‘+’ Geometry

Bar Thickness (fraction of L)	$\frac{E_{22}^U}{E_{22}^H}$	$\frac{E_{33}^U}{E_{33}^H}$	$\frac{G_{23}^U}{G_{23}^H}$	Volume Fraction
0.05	1.004	1.004	1.412	0.191
0.10	1.006	1.006	1.421	0.361
0.15	1.008	1.008	1.307	0.510
0.20	1.012	1.012	1.212	0.640
0.25	1.014	1.014	1.136	0.750
0.30	1.014	1.014	1.078	0.840
0.35	1.011	1.011	1.038	0.910
0.40	1.006	1.006	1.015	0.960
0.45	1.001	1.001	1.003	0.990
0.50	1.000	1.000	1.000	1.000

Comparison of Homogenized and Averaged Moduli With Increasing Finite Element Discretization for the 'x' Geometry

Discretization (num. elements by num. elements)	$\frac{E_{22}^U}{E_{22}^H}$	$\frac{E_{33}^U}{E_{33}^H}$	$\frac{G_{23}^U}{G_{23}^H}$
10	1.113	1.113	3.057
15	1.080	1.080	3.222
20	1.093	1.093	3.165
25	1.101	1.101	2.726
30	1.088	1.088	3.202
35	1.079	1.079	3.593
40	1.086	1.086	3.221
Maximum Fluctuation	0.035	0.035	0.867

Comparison of Homogenized and Averaged Moduli With Increasing Finite Element Discretization for the ‘+’ Geometry

Discretization (num. elements by num. elements)	$\frac{E_{22}^U}{E_{22}^H}$	$\frac{E_{33}^U}{E_{33}^H}$	$\frac{G_{23}^U}{G_{23}^H}$
10	1.237	1.237	1.070
15	1.170	1.170	1.054
20	1.189	1.189	1.042
25	1.162	1.162	1.038
30	1.177	1.177	1.034
35	1.223	1.223	1.030
40	1.172	1.172	1.029
Maximum Fluctuation	0.075	0.075	0.411

Comparison of Homogenized and Averaged Moduli for Single, Rectangular Unit Cells for the 'x' Geometry

$W/L = 1$				
Bar Thickness (fraction of L)	$\frac{E_{22}^U}{E_{22}^H}$	$\frac{E_{33}^U}{E_{33}^H}$	$\frac{G_{23}^U}{G_{23}^H}$	Volume Fraction
0.05	2.366	2.366	1.029	0.281
0.10	1.840	1.840	1.032	0.441
0.15	1.329	1.329	1.038	0.700
0.20	1.189	1.189	1.042	0.800
0.25	1.044	1.044	1.037	0.940
0.30	1.014	1.014	1.023	0.980
0.35	1.000	1.000	1.000	1.000
$W/L = 2$				
Bar Thickness (fraction of L)	$\frac{E_{22}^U}{E_{22}^H}$	$\frac{E_{33}^U}{E_{33}^H}$	$\frac{G_{23}^U}{G_{23}^H}$	Volume Fraction
0.05	2.164	1.175	1.068	0.191
0.10	1.933	1.137	1.071	0.361
0.15	1.487	1.098	1.102	0.580
0.20	1.283	1.027	1.108	0.700
0.25	1.180	1.010	1.110	0.800
0.30	1.120	1.013	1.100	0.880
0.35	1.041	1.013	1.040	0.960
$W/L = 3$				
Bar Thickness (fraction of L)	$\frac{E_{22}^U}{E_{22}^H}$	$\frac{E_{33}^U}{E_{33}^H}$	$\frac{G_{23}^U}{G_{23}^H}$	Volume Fraction
0.05	1.803	0.803	1.092	0.221
0.10	1.909	0.968	1.131	0.387
0.15	1.494	0.936	1.163	0.534
0.20	1.217	0.930	1.188	0.660
0.25	1.109	0.957	1.212	0.767
0.30	1.086	0.985	1.202	0.853
0.35	1.067	1.005	1.108	0.940

Comparison of Homogenized and Averaged Moduli for Single, Rectangular Unit Cells for the '+' Geometry

$W/L = 1$				
Bar Thickness (fraction of L)	$\frac{E_{22}^U}{E_{22}^H}$	$\frac{E_{33}^U}{E_{33}^H}$	$\frac{G_{23}^U}{G_{23}^H}$	Volume Fraction
0.05	1.037	1.037	5.360	0.191
0.10	1.051	1.051	6.219	0.361
0.15	1.067	1.067	4.652	0.510
0.20	1.093	1.093	3.165	0.640
0.25	1.115	1.115	2.167	0.750
0.30	1.113	1.113	1.584	0.840
0.35	1.085	1.085	1.265	0.910
0.40	1.046	1.046	1.099	0.960
0.45	1.013	1.013	1.020	0.990
0.50	1.000	1.000	1.000	1.000
$W/L = 2$				
Bar Thickness (fraction of L)	$\frac{E_{22}^U}{E_{22}^H}$	$\frac{E_{33}^U}{E_{33}^H}$	$\frac{G_{23}^U}{G_{23}^H}$	Volume Fraction
0.05	1.037	1.019	3.571	0.146
0.10	1.053	1.029	6.373	0.281
0.15	1.072	1.041	6.128	0.406
0.20	1.093	1.060	5.028	0.520
0.25	1.116	1.079	3.914	0.625
0.30	1.143	1.087	3.009	0.720
0.35	1.176	1.083	2.333	0.805
0.40	1.210	1.070	1.846	0.880
0.45	1.237	1.053	1.495	0.945
0.50	1.000	1.000	1.000	1.000
$W/L = 3$				
Bar Thickness (fraction of L)	$\frac{E_{22}^U}{E_{22}^H}$	$\frac{E_{33}^U}{E_{33}^H}$	$\frac{G_{23}^U}{G_{23}^H}$	Volume Fraction
0.05	1.037	1.014	2.696	0.131
0.10	1.054	1.021	5.810	0.254
0.15	1.074	1.032	6.533	0.371
0.20	1.097	1.048	5.930	0.481
0.25	1.122	1.065	5.008	0.584
0.30	1.149	1.076	4.124	0.680
0.35	1.176	1.079	3.371	0.770
0.40	1.201	1.075	2.750	0.853
0.45	1.223	1.067	2.223	0.930
0.50	1.000	1.000	1.000	1.000

Design Example Results For 8x8 Unit Cells With 'x' Geometry

d^G [cm]	d^U [cm]	d^H [cm]	Rel. Error Using E_{ij}^U	Rel. Error Using E_{ij}^H
0.227	0.228	0.231	-0.005	-0.018

Design Example Results For 8x8 Unit Cells With '+' Geometry

d^G [cm]	d^U [cm]	d^H [cm]	Rel. Error Using E_{ij}^U	Rel. Error Using E_{ij}^H
1.383	1.149	1.467	0.169	-0.061

Design Example Results For 15x1 Unit Cell Layer With 'x' Geometry

W/L	d^G [cm]	d^U [cm]	d^H [cm]	Rel. Error Using E_{ij}^U	Rel. Error Using E_{ij}^H
1	0.067	0.068	0.069	-0.018	-0.036
5	1.934	1.942	2.295	-0.004	-0.187

Design Example Results For 15x1 Unit Cell Layer With '+' Geometry

W/L	d^G [cm]	d^U [cm]	d^H [cm]	Rel. Error Using E_{ij}^U	Rel. Error Using E_{ij}^H
1	0.250	0.235	0.670	0.058	-1.720
5	15.304	14.200	42.162	0.072	-1.755

Appendix B Single Layer Optimization Results

Below are complete numerical and visual results for the optimization problems presented in Section 5.2.2 of Chapter 5.

Numerical Results For Optimization of E_{22} in a Single Layer Material using Homogenization and Volume Averaging of a 12x1 UC layer

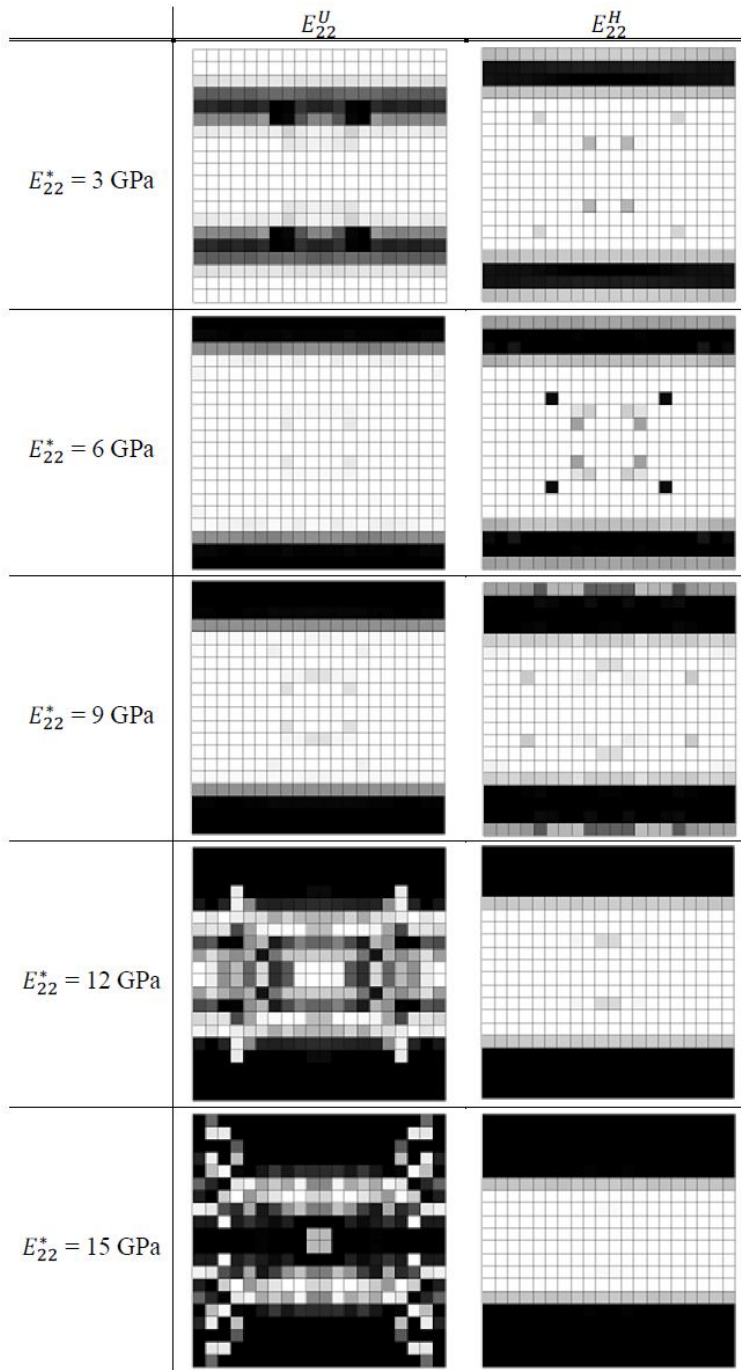
Model	E_{22}^* [GPa]	E_{22}^U [GPa]	V	Comp. Time [s]	Iter.	Func. Eval.
Vol. Aver.	3	3.001	0.229	1547.9	98	318
Homog.	3	3.000	0.201	343.0	130	869
Vol. Aver.	6	6.040	0.250	4135.4	188	1001
Homog.	6	6.000	0.278	333.0	174	785
Vol. Aver.	9	9.001	0.347	1329.1	101	318
Homog.	9	9.001	0.364	309.8	194	680
Vol. Aver.	12	11.800	0.636	4164.7	215	1001
Homog.	12	11.990	0.423	408.0	154	1001
Vol. Aver.	15	14.908	0.722	4362.3	112	1001
Homog.	15	14.999	0.523	139.4	92	281
Vol. Aver.	18	18.000	0.727	11731.9	70	225
Homog.	18	0.000	0.041	33.5	13	76
Vol. Aver.	21	21.001	0.726	1078.9	58	257
Homog.	21	21.000	0.721	72.3	53	158
Vol. Aver.	24	0.000	0.003	28.9	3	5
Homog.	24	0.000	0.004	3.89	3	5
Vol. Aver.	27	26.999	0.963	224.6	10	53
Homog.	27	27.001	0.929	360.4	109	1001
Vol. Aver.	30	30.000	1.000	188.3	15	43
Homog.	30	30.000	1.000	14.4	12	23

Numerical Results For Optimization of E_{33} in a Single Layer Material using Homogenization and Volume Averaging of a 12x1 UC layer

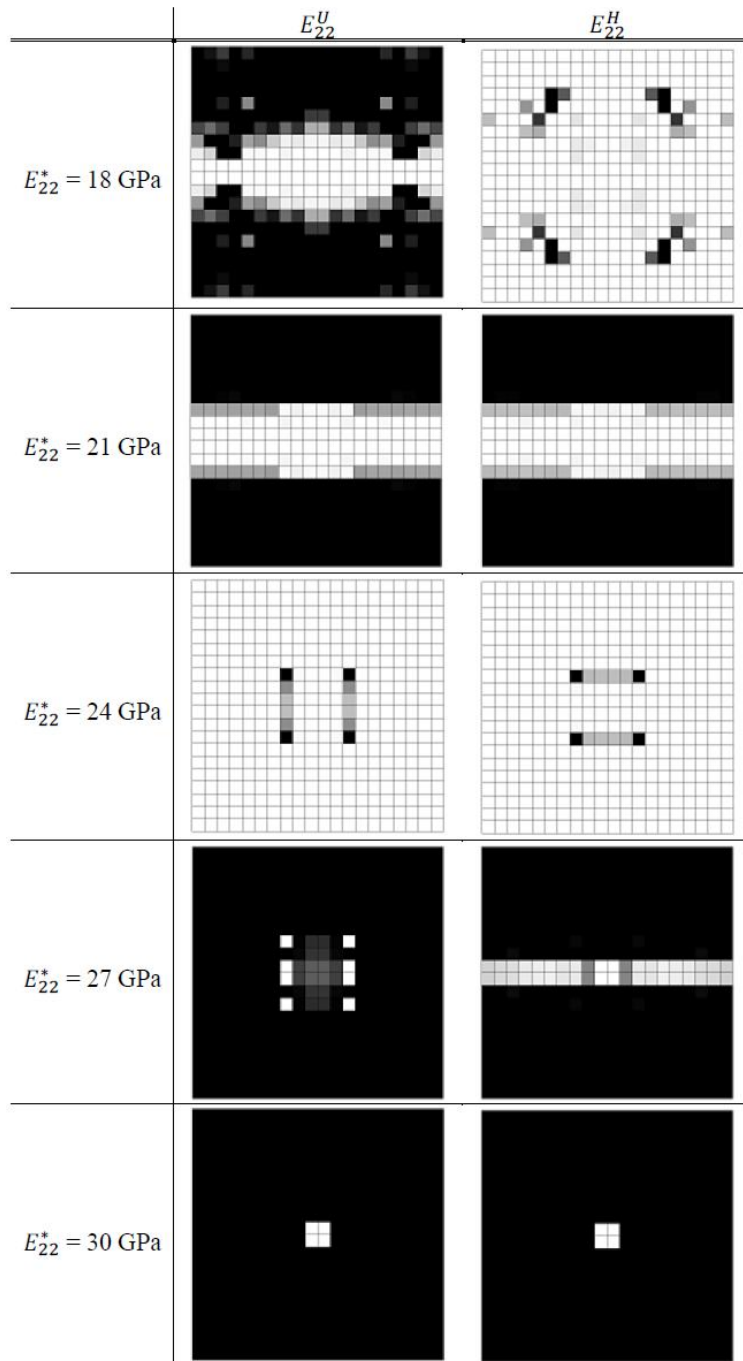
Model	E_{33}^* [GPa]	E_{33}^U [GPa]	V	Comp. Time [s]	Iter.	Func. Eval.
Vol. Aver.	3	3.001	0.151	1225.9	98	293
Homog.	3	3.001	0.231	110.2	72	253
Vol. Aver.	6	6.000	0.241	1702.8	142	404
Homog.	6	6.003	0.262	424.8	164	1001
Vol. Aver.	9	9.000	0.343	2352.1	158	563
Homog.	9	9.003	0.362	386.2	155	1001
Vol. Aver.	12	11.951	0.435	3966.1	134	1001
Homog.	12	12.002	0.441	414.5	183	1001
Vol. Aver.	15	14.999	0.723	603.8	19	148
Homog.	15	0.000	0.035	30.0	11	69
Vol. Aver.	18	18.001	0.803	3006.4	91	736
Homog.	18	0.000	0.073	42.2	15	96
Vol. Aver.	21	20.999	0.738	561.2	41	137
Homog.	21	21.000	0.737	11.3	64	261
Vol. Aver.	24	0.000	0.003	27.9	3	5
Homog.	24	0.000	0.004	3.9	3	5
Vol. Aver.	27	26.999	0.963	222.8	10	53
Homog.	27	27.002	0.929	360.0	109	1001
Vol. Aver.	30	30.000	1.000	187.1	15	43
Homog.	30	30.000	1.000	14.6	12	23

Numerical Results For Optimization of G_{23} in a Single Layer Material using Homogenization and Volume Averaging of a 12x1 UC layer

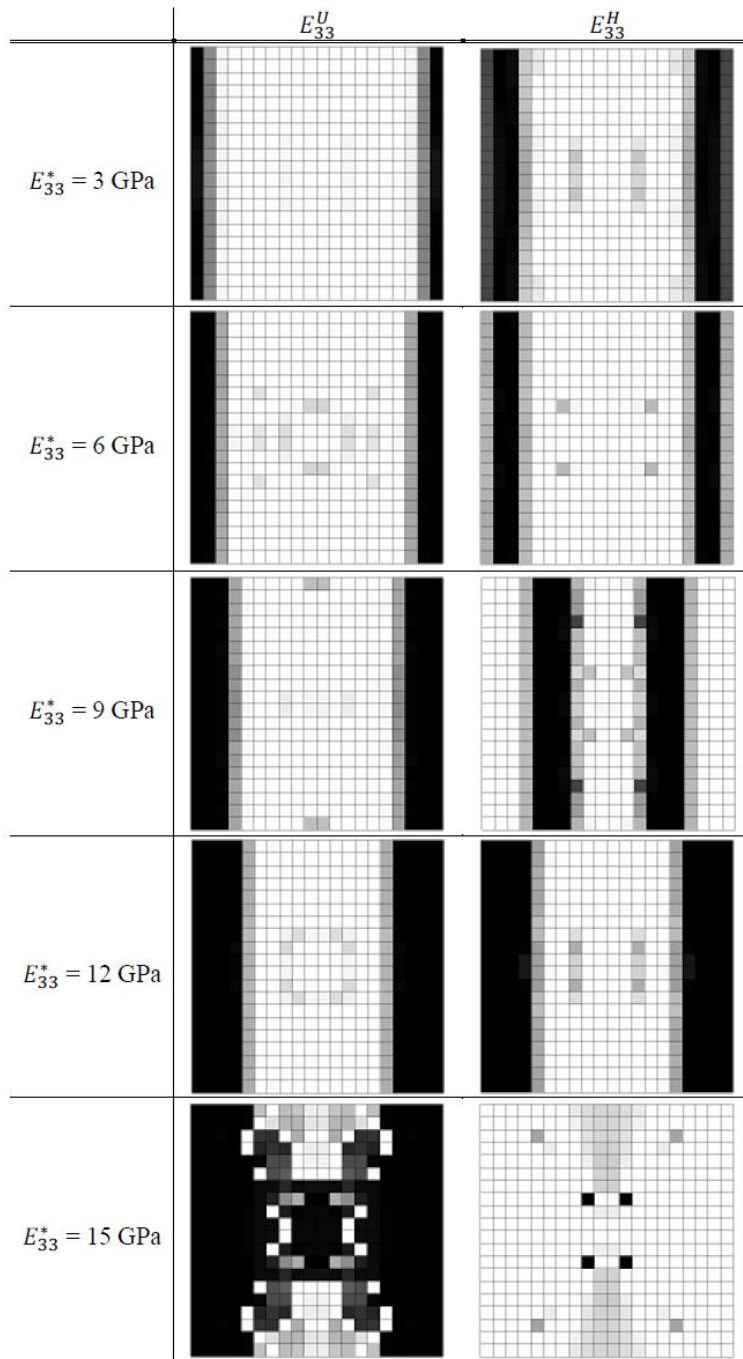
Model	G_{23}^* [GPa]	G_{23}^U [GPa]	V	Comp. Time [s]	Iter.	Func. Eval.
Vol. Aver.	1	1.003	0.328	3696.8	101	1001
Homog.	1	0.999	0.427	24.7	15	51
Vol. Aver.	2	2.001	0.416	719.5	61	188
Homog.	2	2.002	0.485	368.1	133	1001
Vol. Aver.	3	2.999	0.700	177.2	5	45
Homog.	3	3.001	0.641	35.2	14	89
Vol. Aver.	4	3.996	0.562	3853.6	126	1001
Homog.	4	4.001	0.551	145.9	107	319
Vol. Aver.	5	5.001	0.664	666.1	55	174
Homog.	5	54.994	0.717	359.7	85	1001
Vol. Aver.	6	6.003	0.727	3763.9	118	1001
Homog.	6	6.001	0.769	51.1	36	114
Vol. Aver.	7	6.999	0.870	158.1	4	40
Homog.	7	6.999	0.811	152.8	70	382
Vol. Aver.	8	8.003	0.871	3763.6	116	1001
Homog.	8	0.000	0.003	3.9	3	5
Vol. Aver.	9	8.345	0.937	3686.4	73	1001
Homog.	9	9.000	0.920	31.2	24	61
Vol. Aver.	10	10.000	0.954	411.9	29	108
Homog.	10	9.999	0.953	66.4	36	156



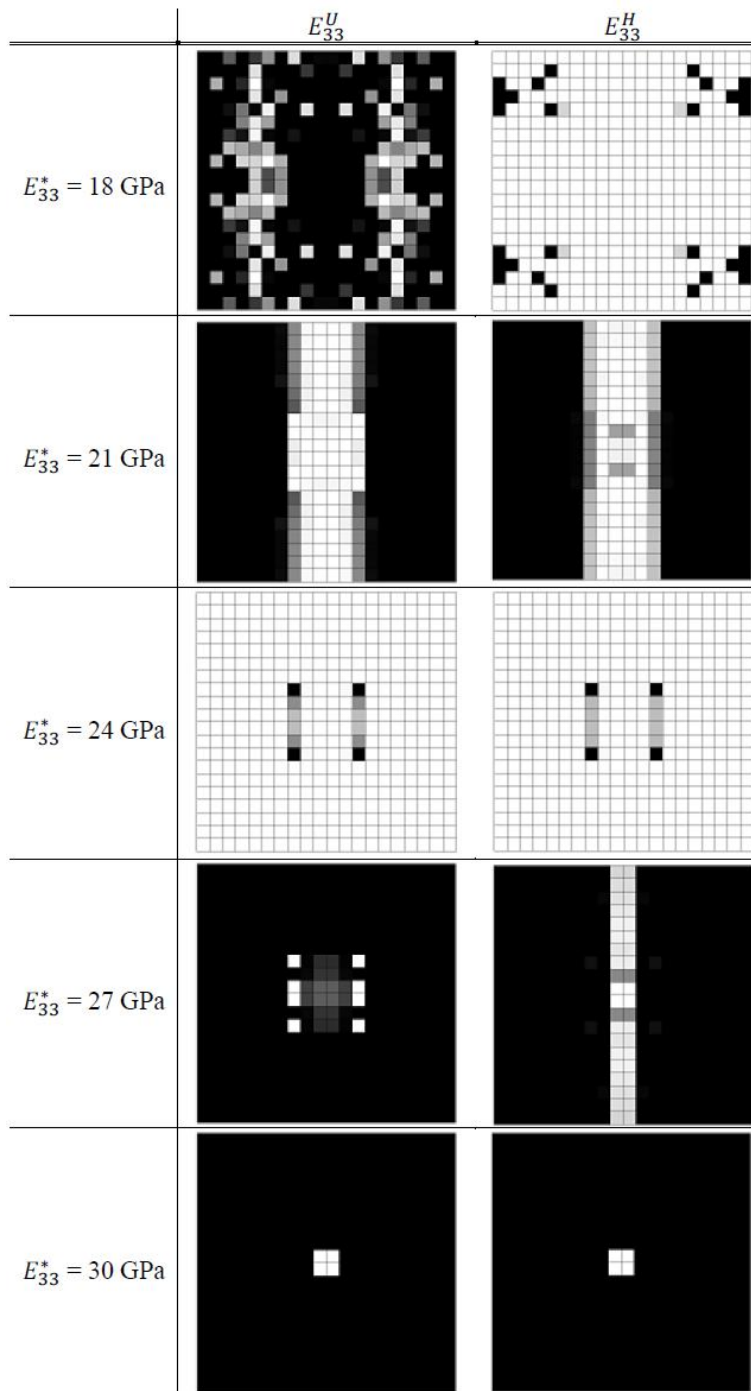
Visual Results Comparing Homogenization and Volume Averaging For Optimization of E_{22} in a Single Layer Material



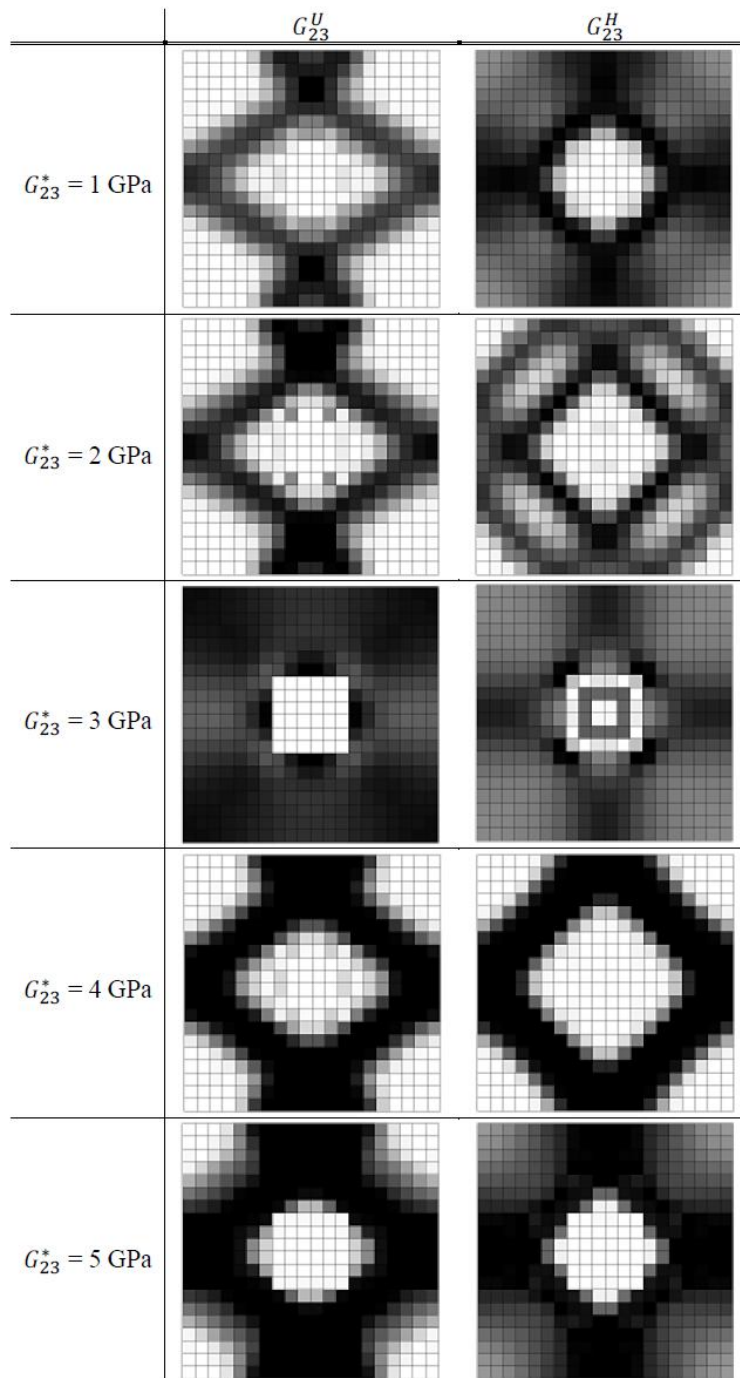
Visual Results Comparing Homogenization and Volume Averaging For Optimization of E_{22} in a Single Layer Material



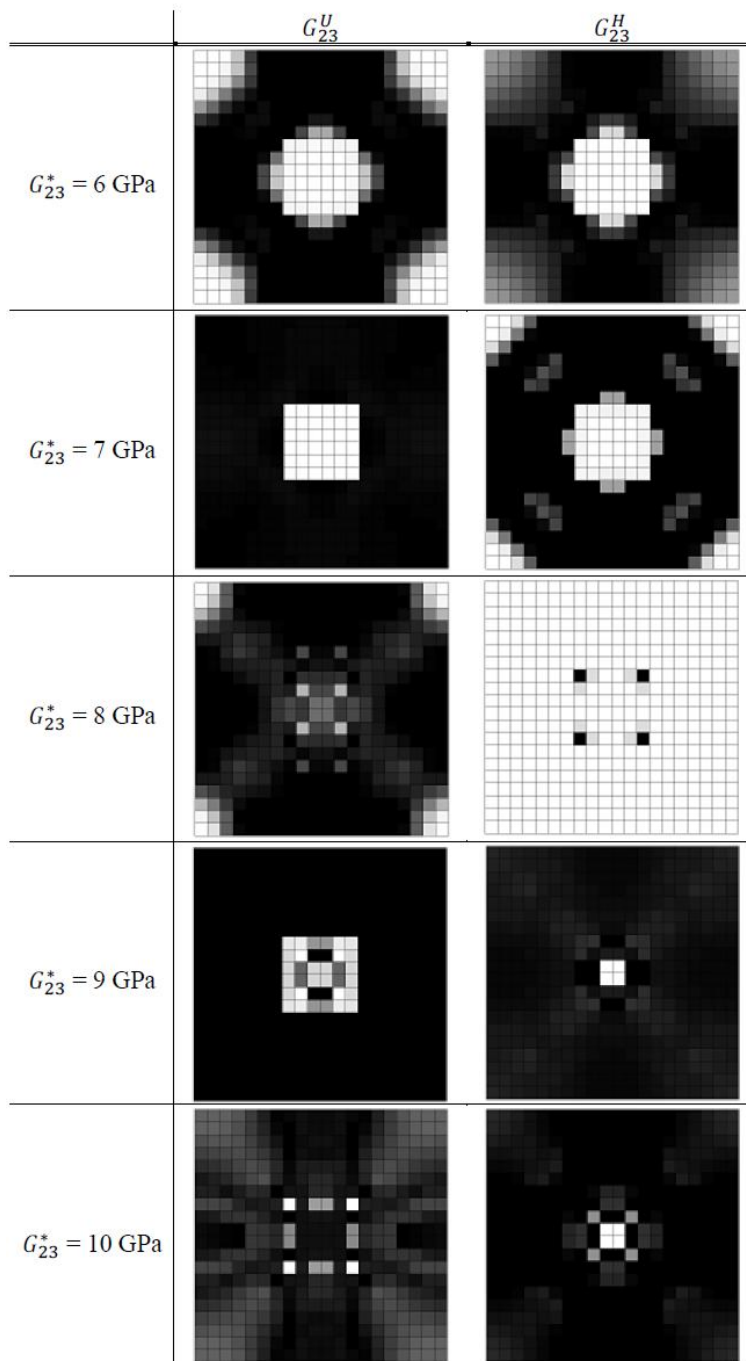
Visual Results Comparing Homogenization and Volume Averaging For Optimization of E_{33} in a Single Layer Material



Visual Results Comparing Homogenization and Volume Averaging For Optimization of E_{33} in a Single Layer Material



Visual Results Comparing Homogenization and Volume Averaging For Optimization of G_{23} in a Single Layer Material



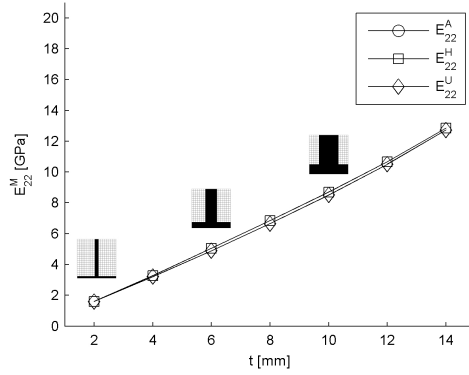
Visual Results Comparing Homogenization and Volume Averaging For Optimization of G_{23} in a Single Layer Material

Appendix C Non-Simple Connectivity Analysis Comparisons

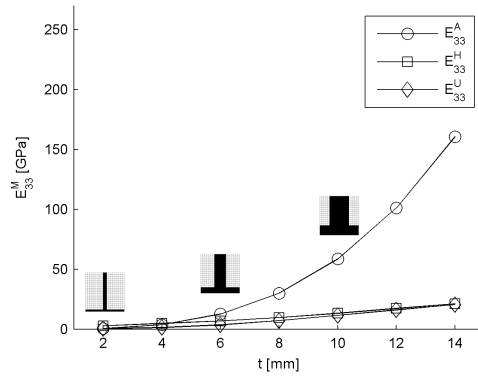
Below are complete visual results for the comparison of numerical analysis methods (homogenization and volume averaging) to analytical equations predicting meta-material properties of honeycomb geometries; a subset of these results are presented in Section 6.3 of 6.

Parameters Used For the Analytical Comparison of Honeycombs in the Equations Given by Gibson et. al [95]

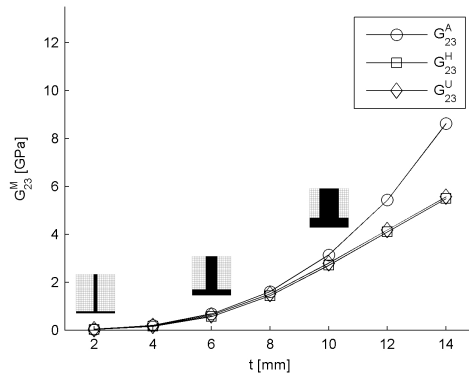
Structure	θ [rad]	l [mm]	h [mm]	Range of thickness t [mm]
1	0	10.00	19.5	2.00-14.00
2	0.3367	10.59	16.50	2.00-14.00
3	0.6107	12.21	13.00	2.00-14.00
4	0.8330	14.87	9.00	2.00-14.00
5	0.9505	17.20	6.00	2.00-14.00
6	1.107	22.36	0.00	2.00-14.00



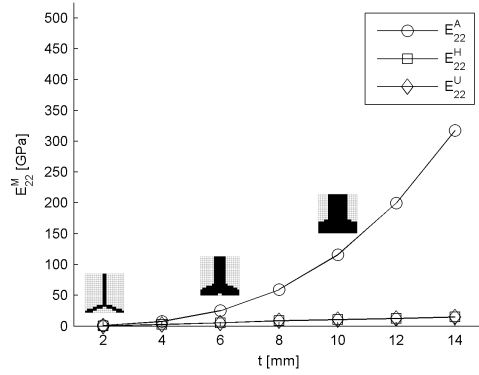
Plot of analytical and numerical E_{22}^M moduli as a function of member thickness in honeycombs for structure 1.



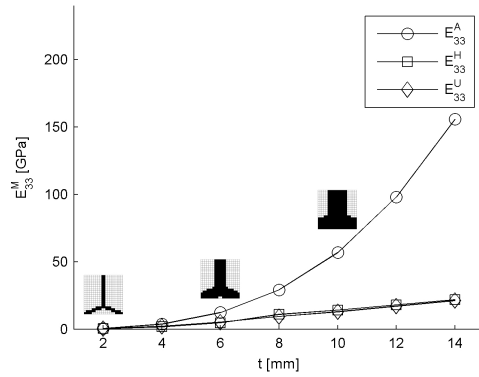
Plot of analytical and numerical E_{33}^M moduli as a function of member thickness in honeycombs for structure 1.



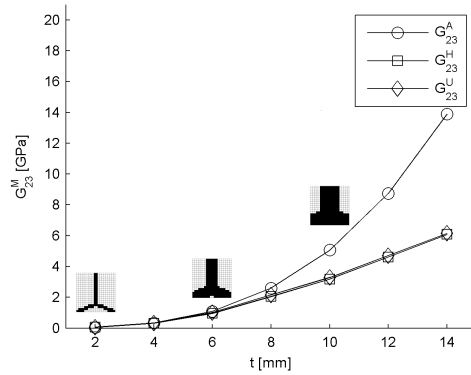
Plot of analytical and numerical G_{23}^M moduli as a function of member thickness in honeycombs for structure 1.



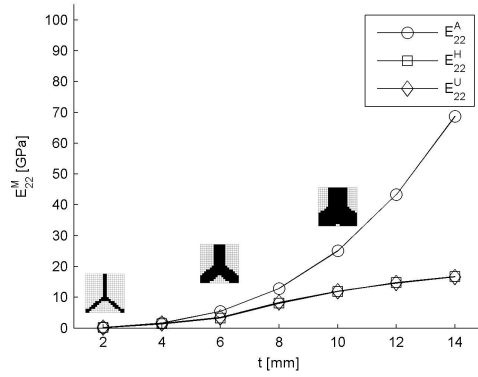
Plot of analytical and numerical E_{22}^M moduli as a function of member thickness in honeycombs for structure 2.



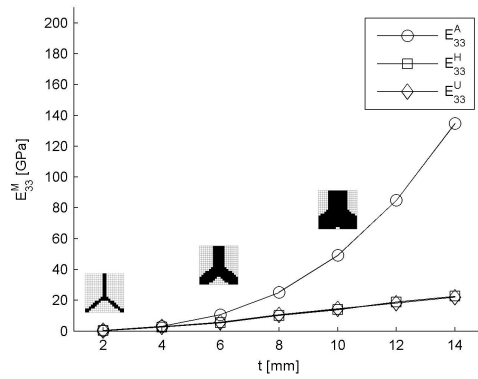
Plot of analytical and numerical E_{33}^M moduli as a function of member thickness in honeycombs for structure 2.



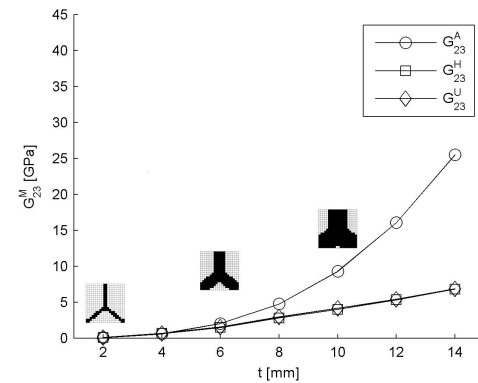
Plot of analytical and numerical G_{23}^M moduli as a function of member thickness in honeycombs for structure 2.



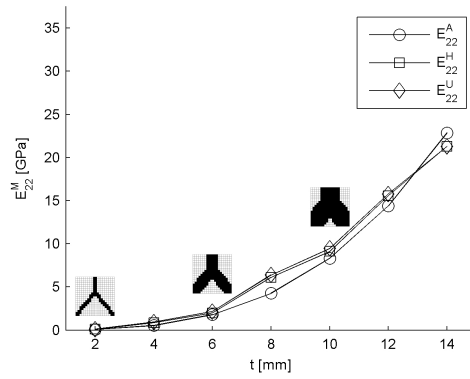
Plot of analytical and numerical E_{22}^M moduli as a function of member thickness in honeycombs for structure 3.



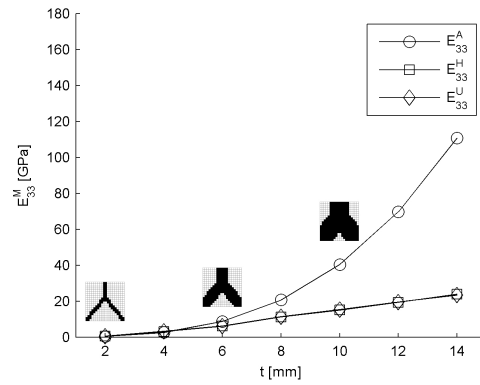
Plot of analytical and numerical E_{33}^M moduli as a function of member thickness in honeycombs for structure 3.



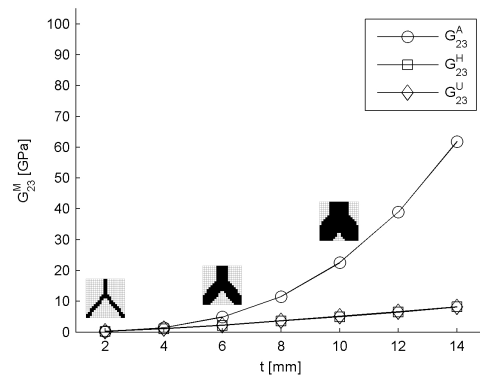
Plot of analytical and numerical G_{23}^M moduli as a function of member thickness in honeycombs for structure 3.



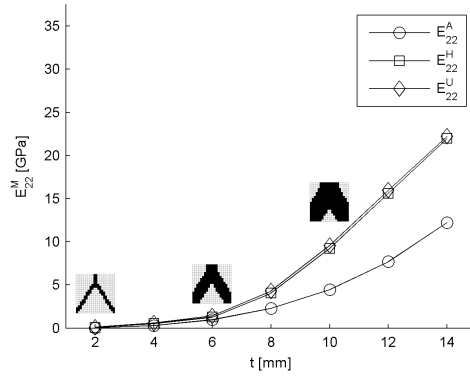
Plot of analytical and numerical E_{22}^M moduli as a function of member thickness in honeycombs for structure 4.



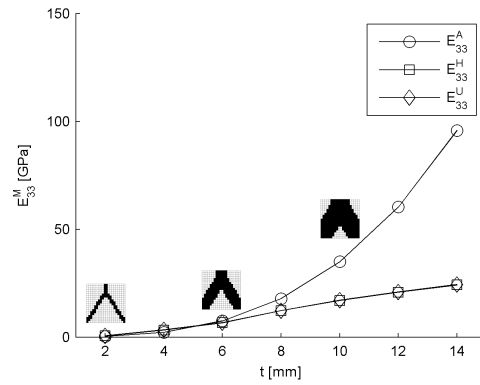
Plot of analytical and numerical E_{33}^M moduli as a function of member thickness in honeycombs for structure 4.



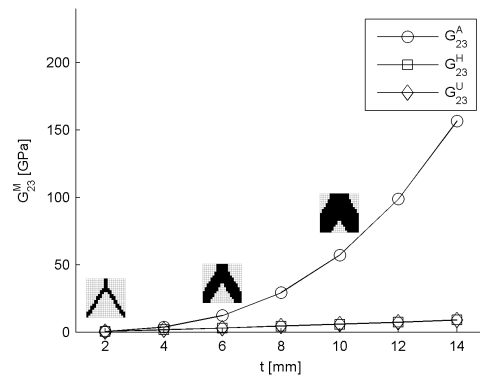
Plot of analytical and numerical G_{23}^M moduli as a function of member thickness in honeycombs for structure 4.



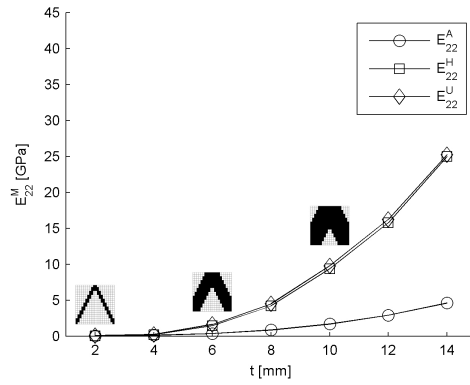
Plot of analytical and numerical E_{22}^M moduli as a function of member thickness in honeycombs for structure 5.



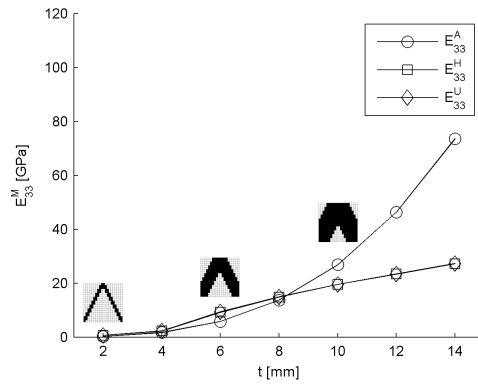
Plot of analytical and numerical E_{33}^M moduli as a function of member thickness in honeycombs for structure 5.



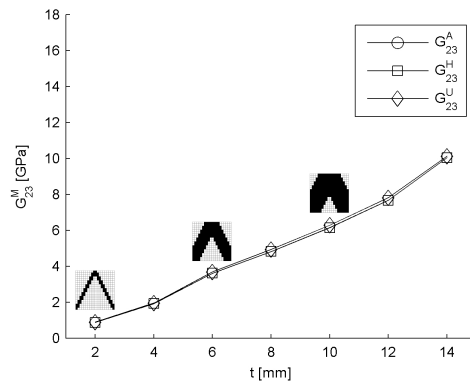
Plot of analytical and numerical G_{23}^M moduli as a function of member thickness in honeycombs for structure 5.



Plot of analytical and numerical E_{22}^M moduli as a function of member thickness in honeycombs for structure 6.



Plot of analytical and numerical E_{33}^M moduli as a function of member thickness in honeycombs for structure 6.



Plot of analytical and numerical G_{23}^M moduli as a function of member thickness in honeycombs for structure 6.

Appendix D Non-Simple Connectivity Optimization Results

Below are complete numerical and visual results for the optimization problems presented in Section 6.4 of Chapter 6.

Numerical Results For Optimization of E_{22} in a Two-Layer Material using Homogenization and Volume Averaging of a 12x2 UC layer

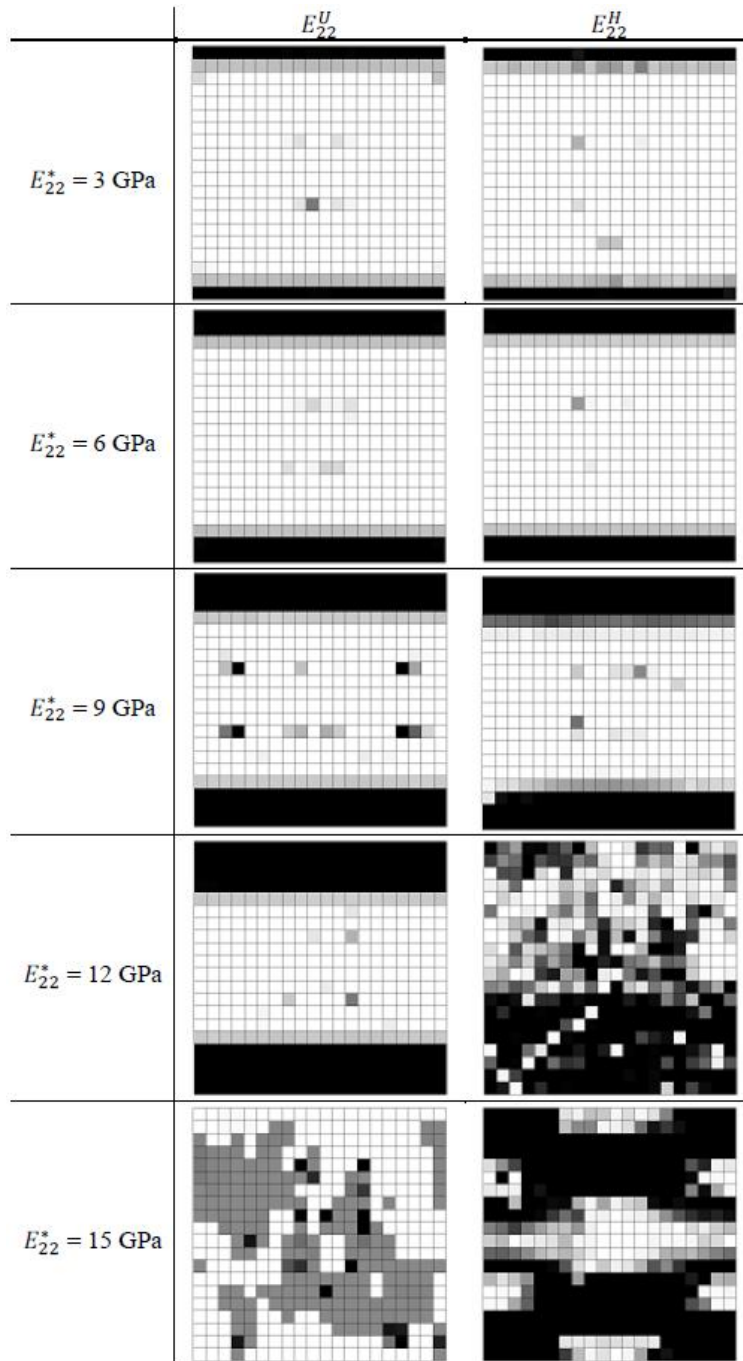
Model	E_{22}^* [GPa]	E_{22}^U [GPa]	V	Comp. Time [s]	Iter.	Func. Eval.
Vol. Aver.	3	3.001	0.130	13162.8	166	1001
Homog.	3	3.000	0.130	806.2	231	935
Vol. Aver.	6	6.001	0.227	5153.6	144	432
Homog.	6	5.999	0.223	392.4	102	259
Vol. Aver.	9	8.993	0.340	13337.0	194	1001
Homog.	9	9.000	0.350	310.0	124	418
Vol. Aver.	12	11.992	0.425	13182.5	181	1001
Homog.	12	9.249	0.554	1119.1	102	1001
Vol. Aver.	15	0.000	0.021	3668.6	21	205
Homog.	15	14.968	0.686	1111.6	160	1001
Vol. Aver.	18	17.999	0.627	4022.4	92	327
Homog.	18	2.844	0.452	2643.3	95	1001
Vol. Aver.	21	20.994	0.736	15188.8	133	1001
Homog.	21	20.977	0.776	692.7	133	1001
Vol. Aver.	24	24.001	0.884	10714.4	138	673
Homog.	24	4.582	0.566	2445.9	82	1001
Vol. Aver.	27	27.001	0.961	515.1	15	29
Homog.	27	27.002	0.942	438.3	139	1001
Vol. Aver.	30	30.000	1.000	453.8	12	23
Homog.	30	30.000	1.000	58.1	12	23

Numerical Results For Optimization of E_{33} in a Two-Layer Material using Homogenization and Volume Averaging of a 12x2 UC layer

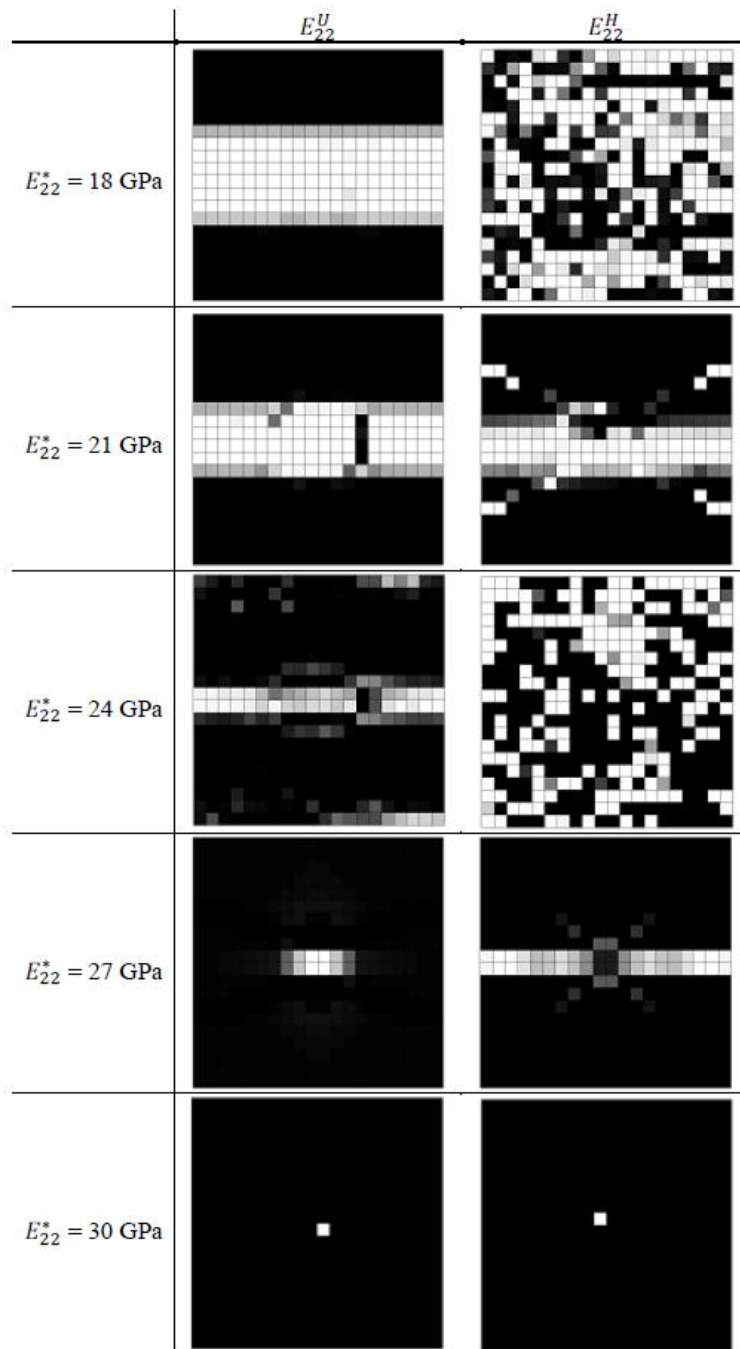
Model	E_{33}^* [GPa]	E_{33}^U [GPa]	V	Comp. Time [s]	Iter.	Func. Eval.
Vol. Aver.	3	3.005	0.203	12679.4	128	1001
Homog.	3	3.005	0.167	912.8	264	1001
Vol. Aver.	6	5.999	0.243	5428.6	130	398
Homog.	6	6.000	0.246	475.1	127	375
Vol. Aver.	9	8.999	0.349	7569.7	175	635
Homog.	9	9.000	0.374	668.0	201	563
Vol. Aver.	12	11.997	0.531	16026.7	203	1001
Homog.	12	11.984	0.534	636.5	265	1001
Vol. Aver.	15	14.874	0.773	15549.1	127	1001
Homog.	15	15.000	0.646	426.6	150	723
Vol. Aver.	18	8.534	0.716	6971.3	46	277
Homog.	18	17.979	0.715	500.9	148	1001
Vol. Aver.	21	17.415	0.797	18561.7	155	1001
Homog.	21	20.921	0.781	726.2	133	1001
Vol. Aver.	24	8.701	0.672	20357.2	87	1001
Homog.	24	2.0497	0.429	1559.4	108	1001
Vol. Aver.	27	26.999	0.950	2946.2	63	181
Homog.	27	27.001	0.966	48.0	8	19
Vol. Aver.	30	30.000	1.000	992.5	24	61
Homog.	30	30.000	1.000	74.0	12	23

Numerical Results For Optimization of G_{23} in a Two-Layer Material using Homogenization and Volume Averaging of a 12x2 UC layer

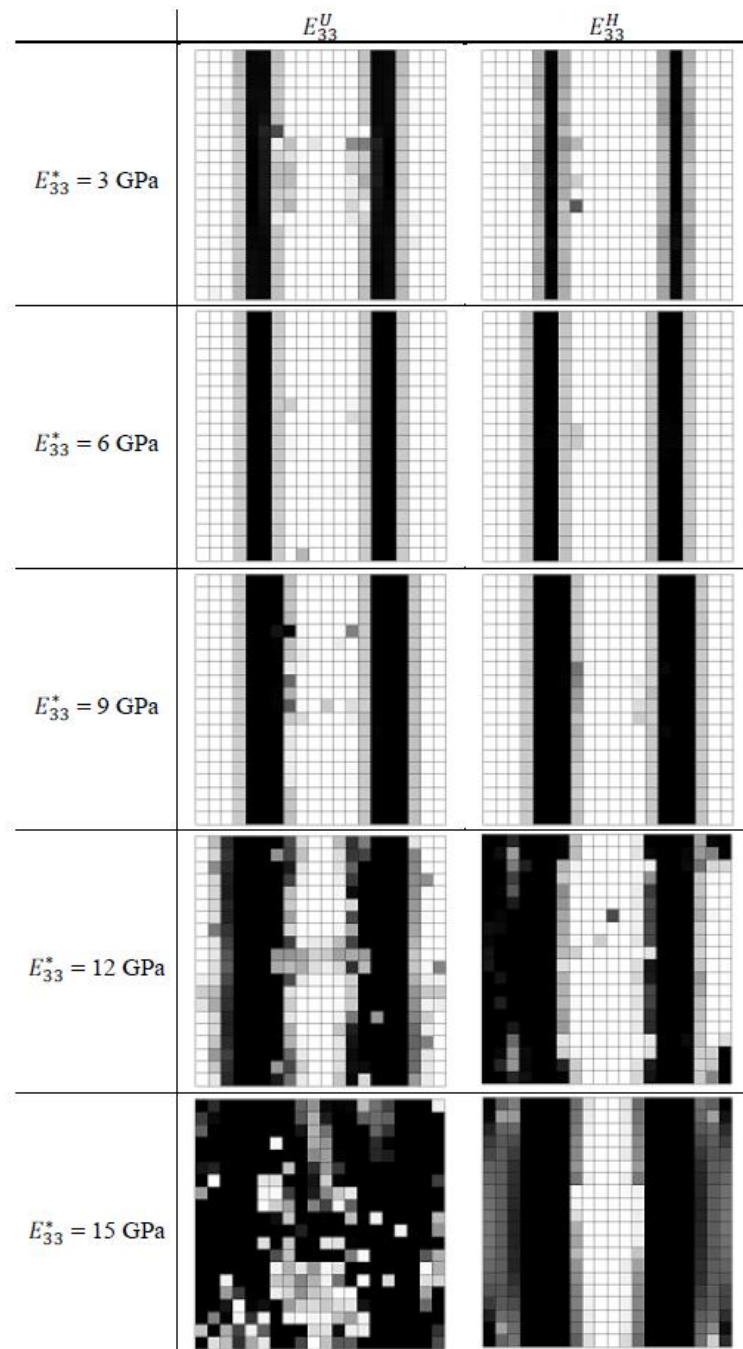
Model	G_{23}^* [GPa]	G_{23}^U [GPa]	V	Comp. Time [s]	Iter.	Func. Eval.
Vol. Aver.	1	1.001	0.320	2418.5	73	203
Homog.	1	0.999	0.332	201.8	82	227
Vol. Aver.	2	2.000	0.455	7842.2	154	627
Homog.	2	2.001	0.411	196.7	79	199
Vol. Aver.	3	2.992	0.589	11104.4	153	1001
Homog.	3	2.999	0.572	94.1	59	191
Vol. Aver.	4	0.000	0.053	1908.0	16	156
Homog.	4	4.001	0.585	232.2	102	367
Vol. Aver.	5	2.632	0.613	12299.3	103	1001
Homog.	5	4.999	0.716	125.5	64	229
Vol. Aver.	6	5.999	0.830	2788.1	48	247
Homog.	6	5.993	0.777	554.2	107	1001
Vol. Aver.	7	6.990	0.893	10507.2	122	1001
Homog.	7	6.999	0.873	7.6	2	15
Vol. Aver.	8	8.000	0.926	2331.7	45	194
Homog.	8	7.904	0.866	695.5	95	1001
Vol. Aver.	9	8.996	0.964	10668.1	88	1001
Homog.	9	8.999	0.918	102.6	46	189
Vol. Aver.	10	10.000	1.000	300.2	11	21
Homog.	10	9.999	0.965	42.3	8	17



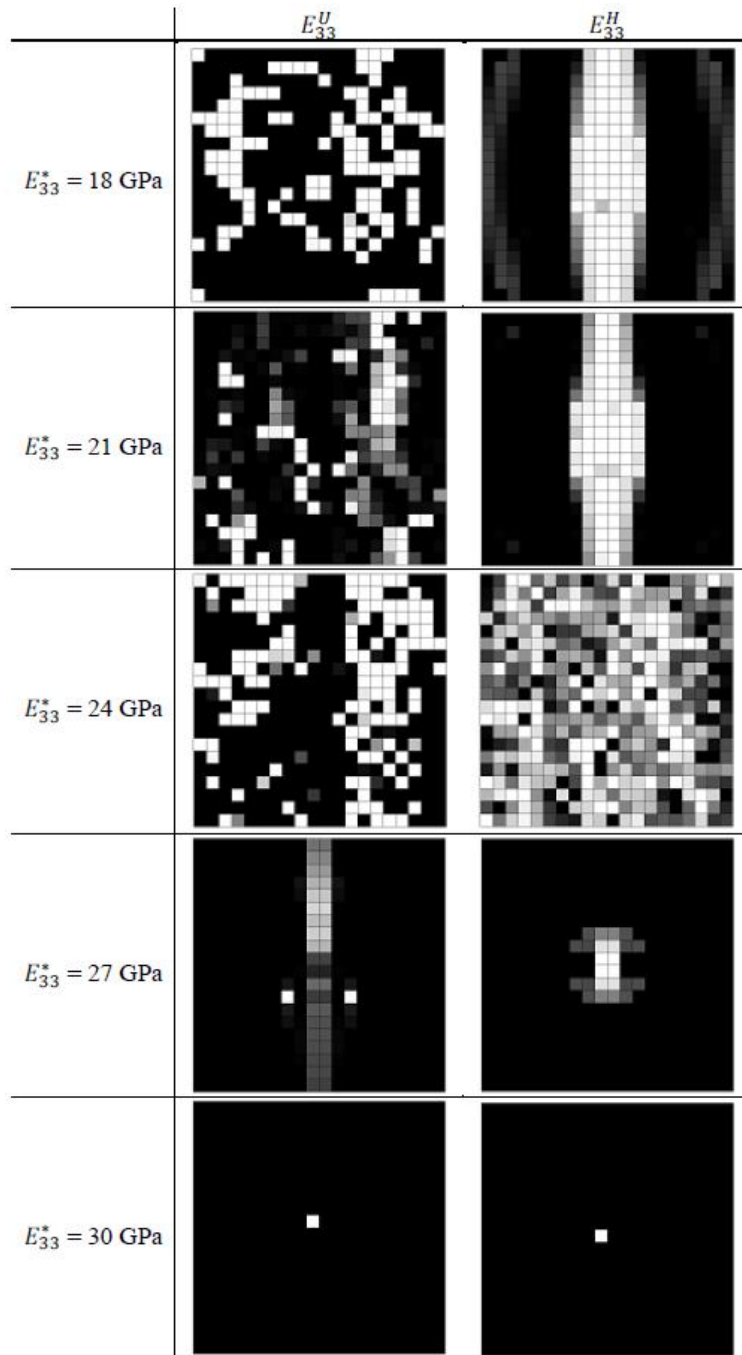
Visual Results Comparing Homogenization and Volume Averaging For Optimization of E_{22} in a Material With Non-Simple Periodicity



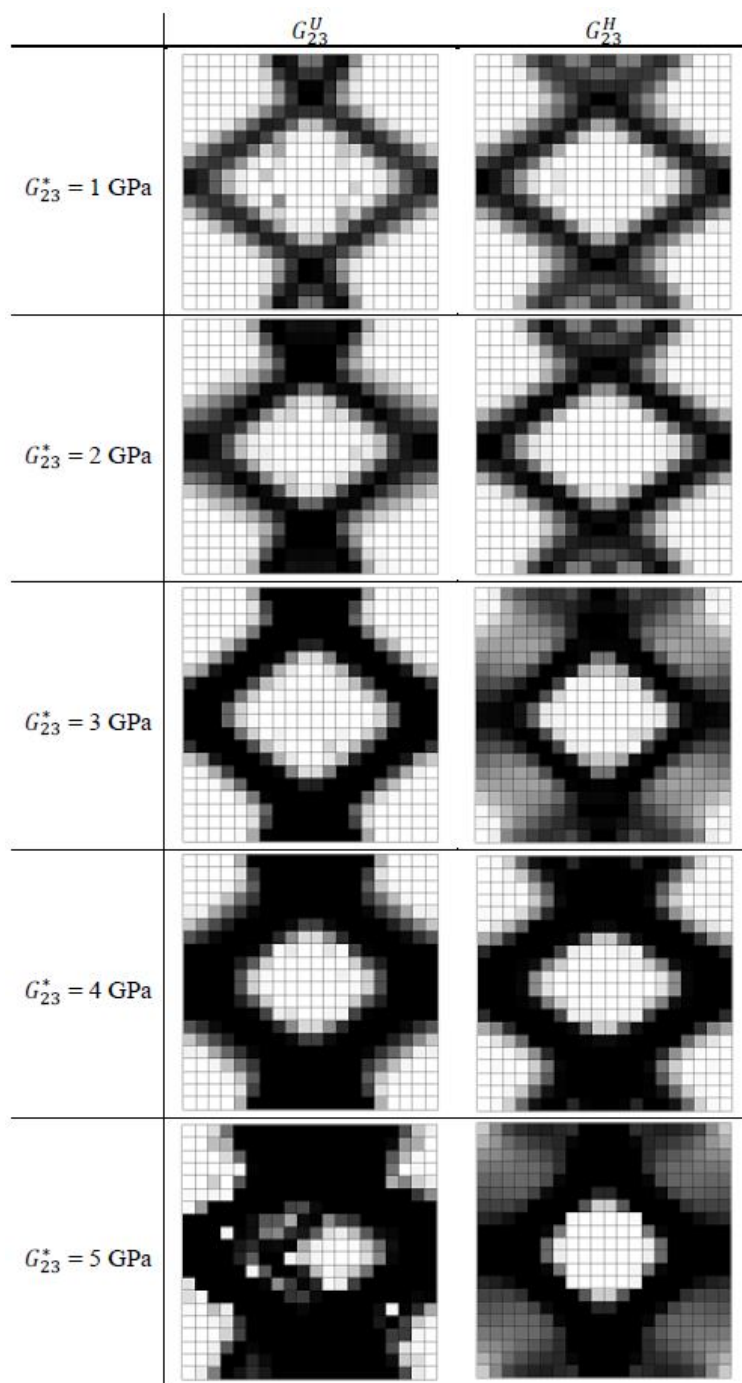
Visual Results Comparing Homogenization and Volume Averaging For Optimization of E_{22} in a Material With Non-Simple Periodicity



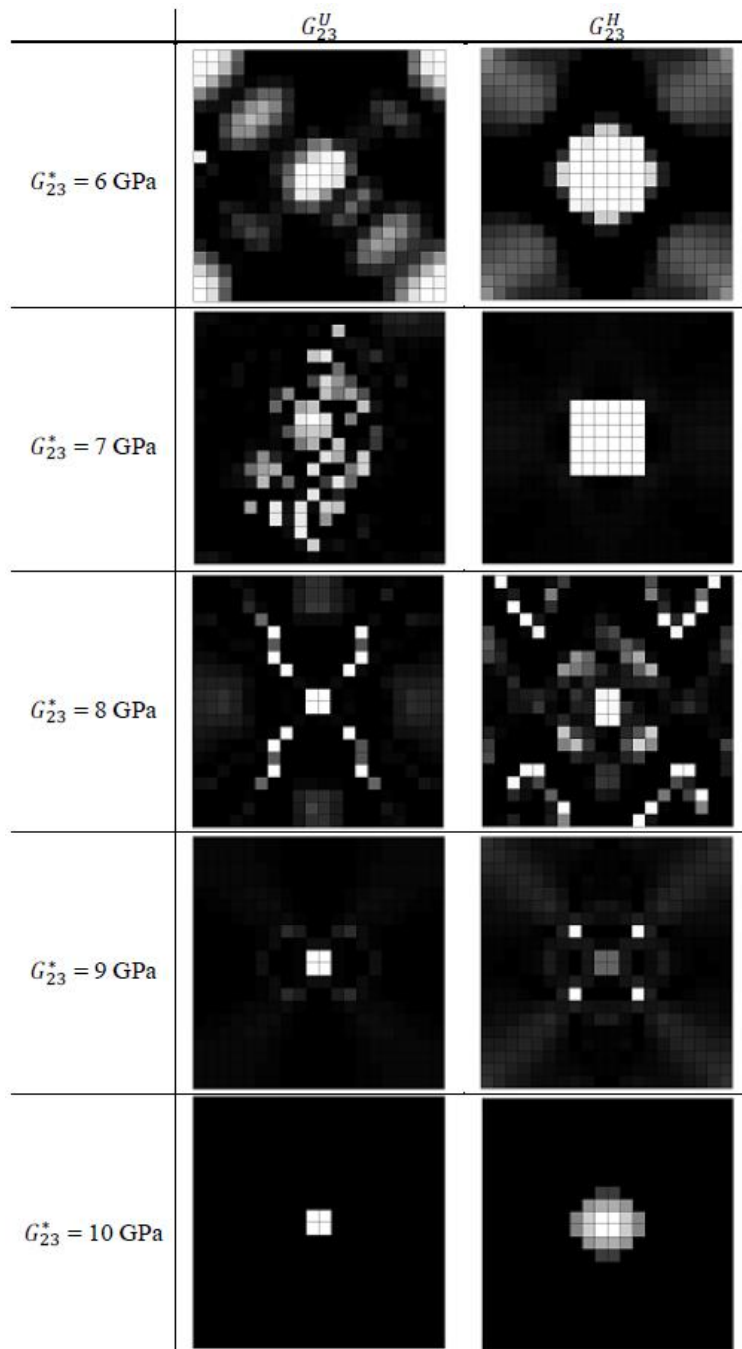
Visual Results Comparing Homogenization and Volume Averaging For Optimization of E_{33} in a Material With Non-Simple Periodicity



Visual Results Comparing Homogenization and Volume Averaging For Optimization of E_{33} in a Material With Non-Simple Periodicity



Visual Results Comparing Homogenization and Volume Averaging For Optimization of G_{23} in a Material With Non-Simple Periodicity



Visual Results Comparing Homogenization and Volume Averaging For Optimization of G_{23} in a Material With Non-Simple Periodicity

Bibliography

- [1] Altair Engineering, Inc. *Optistruct Tutorials, Version 3.5*.
- [2] S. Nishiwaki, M.I. Frecker, S. Min, and N. Kikuchi. Topology optimization of compliant mechanisms using the homogenization method. *International Journal of Numerical Methods in Engineering*, 42:535–559, 1998.
- [3] C. Czech, P. Guarneri, J. Gibert, and G. Fadel. On the accurate analysis of linear elastic meta-material properties for use in design optimization problems. *Composites Science and Technology*, 72:580–586, 2012.
- [4] B. Hassani. A direct method to derive the boundary conditions of the homogenization equation for symmetric cells. *Communications in Numerical Methods in Engineering*, 12(3):185–196, 1996.
- [5] H. Hassani and E. Hinton. A review of homogenization and topology optimization I—homogenization theory for media with periodic structure. *Computers and Structures*, 69:707–717, 1998.
- [6] D.L. McDowell, J.H. Panchal, H.-J. Choi, C.C. and Allen J.K. Seepersad, and F. Mistree. *Integrated Design of Multiscale, Multifunctional Materials and Products*. El Sevier: Butterworth-Heinemann, New York, 2010.
- [7] T.B. Rhyne and S.M. Cron. Development of a non-pneumatic wheel. *Tire Science and Technology*, 34(3):150–169, 2006.
- [8] T.B. Rhyne. Rolling resistance thoughts. Technical report, 2007.
- [9] T.B. Rhyne. Tweel rolling resistance coefficients. Technical report, 2008.
- [10] M.F. Ashby. *Materials Selection in Mechanical Design*. El Sevier, third edition, 2005.
- [11] N.B. Thyagaraja. Requirements determination of a novel non-pneumatic wheel shear beam for low rolling resistance. Master’s thesis, Clemson Univeristy, May 2011.
- [12] E. Lowe, J. Ziegert, and P. Joseph. Energy loss in a non-continuous shear layer. Technical report, 2008.
- [13] N. Thyagaraja, P. Shankar, G. Fadel, and P. Guarneri. Optimizing the shear beam of a non-pneumatic wheel for low rolling resistance. *Proceedings of the ASME IDETC/CIE 2011 Conference*, DETC2011-48532:1–10, 2011.

- [14] R.M. Christensen. *Mechanics of Composite Materials*. John Wiley and Sons, 1979.
- [15] R.M. Jones. *Mechanics of Composite Materials*. McGraw-Hill, 1975.
- [16] A. Diaz and A. Bénard. Designing materials with prescribed elastic properties using polygonal cells. *International Journal for Numerical Methods in Engineering*, 57:301–314, 2003.
- [17] F. Lipperman, M. Fuchs, and M. Ryvkin. Stress localization and strength optimization of frame material with periodic microstructure. *Computer Methods in Applied Mechanics and Engineering*, 197:4016–4026, 2008.
- [18] J. Ju, J.D. Summers, J. Ziegert, and G. Fadel. Design of honeycomb meta-materials for high shear flexure. *Proceedings of the ASME IDETC/CIE 2009 Conference*, IDETC/DAC-87730, 2009.
- [19] W. Zhang, G. Dai, F. Wang, S. Sun, and H. Bassir. Using strain-energy based prediction of effective elastic properties in topology optimization of material microstructures. *Acta Mechanica Sina*, 23:77–89, 2007.
- [20] O. Sigmund. Materials with prescribed constitutive parameters: An inverse homogenization problem. *International Journal of Solids and Structures*, 31(17):2313–2329, 1994.
- [21] O. Sigmund. Tailoring materials with prescribed elastic properties. *Mechanics of Materials*, 20:351–368, 1995.
- [22] A. Bénard and A. Diaz. On the discretization of problems involving periodic planar tilings. *Communications in Numerical Methods in Engineering*, 17:543–549, 2001.
- [23] G. Paulino, E. Silva, and C. Le. Optimal design of periodic functionally graded composites with prescribed properties. *Structural and Multidisciplinary Optimization*, 38:469–489, 2009.
- [24] U. Larsen, O. Sigmund, and S. Bouwstra. Design and fabrication of compliant mechanisms and structures with negative poisson’s ratio. *IEEE Journal of Microelectromechanical Systems*, 6(2):99–106, 1997.
- [25] O. Sigmund. A new class of extremal composites. *Journal of the Mechanics and Physics of Solids*, 48(2):397–428, 2000.
- [26] L. Gibiansky and O. Sigmund. Multiphase elastic compliances with extremal bulk modulus. *Journal of the Mechanics and Physics of Solids*, 48(3):461–498, 2000.
- [27] O. Sigmund and S. Torquato. Composites with extremal thermal expansion coefficients. *Applied Physics Letters*, 69(21):3203–3205, 1996.
- [28] O. Sigmund and S. Torquato. Design of materials with extreme thermal expansion using a three-phase topology optimization method. *Journal of the Mechanics and Physics of Solids*, 45(6):1037–1067, 1997.

- [29] O. Sigmund, S. Torquato, and I. Askay. On the design of 1-3 piezocomposites using topology optimization. *Journal of Materials Research*, 13(4):1038–1048, 1998.
- [30] E. Silva, J. Fonseca, and N. Kikuchi. Optimal design of periodic piezoelectric microstructures. *Computational Mechanics*, 19(5):397–410, 1997.
- [31] E. Silva, J. Fonseca, and N. Kikuchi. Optimal design of periodic piezocomposites. *Computer Methods in Applied Mechanics and Engineering*, 159(2):49–77, 1998.
- [32] Z. Fang, W. Sun, and J. Tzeng. Asymptotic homogenization and numerical implementation to predict effective mechanical properties for electromagnetic composite conductor. *Journal of Composite Materials*, 38(16):1371–1385, 2003.
- [33] J. Guest and J. Prevost. Design of maximum permeability structures. *Computer Methods in Applied Mechanics and Engineering*, 196(4-6):1006–1017, 2007.
- [34] J.K. Guest and J.H. Prvost. Optimizing multifunctional materials: Design of microstructures for maximized stiffness and fluid permeability. *International Journal of Solids and Structures*, 43(22-23):7028–7047, 2006.
- [35] S. Torquato and S. Hyun. Optimal design of manufacturable three-dimensional composites with multifunctional characteristics. *Journal of Applied Physics*, 94(9):5748–5755, 2003.
- [36] J. Guedes, H. Rodrigues, and M. Bendsøe. A material optimization model to approximate energy bounds for cellular materials under multiload conditions. *Structural and Multidisciplinary Optimization*, 25:446–452, 2003.
- [37] C. Seepersad, J. Allen, D. McDowell, and F. Mistree. Robust design of cellular materials with topological and dimensional imperfections. *ASME Conference*, 4739X:807–821, 2005.
- [38] C.C. Seepersad, J.K. Allen, D.L. McDowell, and F. Mistree. Robust design of cellular materials with topological and dimensional imperfections. *ASME Journal of Mechanical Design*, 128(6):1285–1297, 2006.
- [39] B. Hassani and E. Hinton. A review of homogenization and topology optimization II—analytical and numerical solution of homogenization equations. *Computers and Structures*, 69:719–738, 1998.
- [40] B. Hassani and E. Hinton. A review of homogenization and topology optimization III—topology optimization using optimality criteria. *Computers and Structures*, 69:739–756, 1998.
- [41] M.P. Bendsøe and N. Kikuchi. Generating optimal topologies in structural design using a homogenization method. *Computer Methods in Applied Mechanics and Engineering*, 71:197–224, 1988.
- [42] S. Hollister and N. Kikuchi. A comparison of homogenization and standard mechanics analyses for periodic porous composites. *Computational Mechanics*, 10:73–95, 1992.

- [43] S. Pecullan, L. Gibiansky, and S. Torquato. Scale effects on the elastic behavior of periodic and hierarchical two-dimensional composites. *Journal of the Mechanics and Physics of Solids*, 47:1509–1542, 1999.
- [44] S. Hazanov and C. Huet. Order relationships for boundary conditions effect in heterogeneous bodies smaller than the representative volume. *Journal of the Mechanics and Physics of Solids*, 42:1995–2011, 1994.
- [45] S. Hazanov and M. Amieur. On overall properties of elastic heterogeneous bodies smaller than the representative volume. *International Journal of Engineering Science*, 33:1289–1301, 1995.
- [46] M.-J. Pindera, H. Khatam, A. Drago, and Y. Bansal. Micromechanics of spatially uniform heterogeneous media: A critical review and emerging approaches. *Composites: Part B*, 10:349–378, 2009.
- [47] A. Drago and M.-J. Pindera. Micro-macromechanical analysis of heterogeneous materials: Macroscopically homogeneous vs. periodic microstructures. *Composites Science and Technology*, 67:1243–1263, 2007.
- [48] L. Yin and G.K. Ananthasuresh. Topology optimization of compliant mechanisms with multiple materials using a peak function material interpolation scheme. *Structural and Multidisciplinary Optimization*, 23:49–62, 2001.
- [49] R.C. Hibbeler. *Mechanics of Materials*. Pearson Prentice Hall, sixth edition, 2005.
- [50] M.P. Bendsøe and O. Sigmund. *Topology Optimization: Theory, Methods and Applications*. Springer, second edition, 2003.
- [51] H. Eschenauer and N. Olhoff. Topology optimization of continuum structures: A review. *Applied Mechanics Review*, 54(4):331–390, 2001.
- [52] M.P. Bendsøe and O. Sigmund. Material interpolation schemes in topology optimization. *Archive of Applied Mechanics*, 69:635–654, 1999.
- [53] M.P. Bendsøe. *Optimization of Structural Topology, Shape and Material*. Springer, first edition, 1995.
- [54] M.P. Bendsøe. Optimal shape design as a material distribution problem. *Structural Optimization*, 1:193–202, 1989.
- [55] G.I.N. Rozvany, M. Zhou, and T. Birker. Generalized shape optimization without homogenization. *Structural Optimization*, 4:250–254, 1992.
- [56] A. Rietz. Sufficiency of a finite exponent in SIMP (power law) methods. *Structural and Multidisciplinary Optimization*, 21:159–163, 2001.
- [57] J.M. Martinez. A note on the theoretical convergence properties of the SIMP method. *Structural and Multidisciplinary Optimization*, 29:319–323, 2005.

- [58] C.B.W. Pedersen. Topology synthesis of large-displacement compliant mechanisms. *International Journal of Numerical Methods in Engineering*, 50:2683–2705, 2001.
- [59] T.E. Bruns. A reevaluation of the SIMP method with filtering and an alternative formulation for solid-void topology optimization. *Structural and Multidisciplinary Optimization*, 30:428–436, 2005.
- [60] M. Stolpe and K. Svanberg. An alternative interpolation scheme for minimum compliance topology optimization. *Structural and Multidisciplinary Optimization*, 22:116–124, 2001.
- [61] M. Frecker, N. Kikuchi, and S. Kota. Topology optimization of compliant mechanisms with multiple outputs. *Structural Optimization*, 17:269–278, 1999.
- [62] T.A. Poulsen. A simple scheme to prevent checkerboard patterns and one-node connected hinges in topology optimization. *Structural and Multidisciplinary Optimization*, 24:396–399, 2002.
- [63] C.S. Jog and R.B. Haber. Stability of finite element models for distributed-parameter optimization and topology design. *Computer Methods in Applied Mechanical Engineering*, 130(3-4):203–226, 1996.
- [64] A. Diaz and O. Sigmund. Checkerboard patterns in layout optimization. *Structural and Multidisciplinary Optimization*, 24:40–45, 1995.
- [65] R.B. Haber, C.S. Jog, and M.P. Bendsøe. A new approach to variable-topology shape design using a constraint on perimeter. *Structural and Multidisciplinary Optimization*, 11:1–12, 1996.
- [66] O. Sigmund and J. Petersson. Numerical instabilities in topology optimization: A survey on procedures dealing with checkerboards, mesh-dependencies and local minima. *Structural and Multidisciplinary Optimization*, 16:68–75, 1998.
- [67] O. Sigmund. *Design of material structures using topology optimization*. PhD thesis, Technical University of Denmark, 1994.
- [68] J.M. Gibert and G.M. Fadel. Numerical experiments in using voronoi cell finite elements for topology optimization. *Proceedings of the ASME IDETC/CIE 2009 Conference*, DETC2009-87460, 2009.
- [69] C. Talischi, G.H. Paulino, and Chau. H. Le. Honeycomb wachspress finite elements for structural topology optimization. *Structural and Multidisciplinary Optimization*, 37:569–583, 2009.
- [70] R. Saxena and A. Saxena. On honeycomb representation and sigmoid material assignment in optimal topology synthesis of compliant mechanisms. *Finite Elements In Analysis and Design*, 43:1082–1098, 2007.
- [71] G.I.N. Rozvany. A critical review of established methods of structural topology optimization. *Structural and Multidisciplinary Optimization*, 37:217–237, 2009.

- [72] K. Svanberg. The method of moving asymptotes—a new method for structural optimization. *International Journal for Numerical Methods in Engineering*, 24:359–373, 1987.
- [73] Z. Luo, L. Chen, J. Yang, Y. Zhang, and K. Abdel-Malek. Compliant mechanism design using multiobjective topology optimization scheme of continuum structures. *Structural and Multidisciplinary Optimization*, 30:142–154, 2005.
- [74] O. Sigmund. *Systematic design of metamaterials by topology optimization*, volume 13 of *IUTAM Bookseries*, pages 151–159. Springer, September 2009. IUTAM Symposium on Modeling Nanomaterials and Nanosystems.
- [75] A. Saxena. Topology design of large displacement compliant mechanisms with multiple materials and multiple output ports. *Structural and Multidisciplinary Optimization*, 30:477–490, 2005.
- [76] M. Sauter, G. Kress, M. Giger, and P. Ermanni. Complex-shaped beam element and graph-based optimization of compliant mechanisms. *Structural and Multidisciplinary Optimization*, 36:429–442, 2008.
- [77] R.D. Cook, D.S. Malkus, and M.E. Plesha. *Concepts and Applications of Finite Element Analysis*. John Wiley and Sons, third edition, 1989.
- [78] L. Yin and W. Yang. Optimality criteria for topology optimization under multiple constraints. *Computers and Structures*, 79:1839–1850, 2001.
- [79] M.M. Neves, H. Rodrigues, and J.M. Guedes. Optimal design of periodic linear elastic microstructures. *Computers and Structures*, 76:421–429, 2000.
- [80] H.C. Rodrigues. Topology optimization of structures: Applications in the simulations and design of cellular materials. *Computational Methods in Engineering and Science*, pages 101–112, 2006.
- [81] Y. Chen, S. Zhou, and Q. Li. Multiobjective topology optimization for finite periodic structures. *Computers and Structures*, 88:806–811, 2010.
- [82] Q.Q. Ling and G.P. Steven. A performance-based optimization method for topology design of continuum structures with mean compliance constraint. *Computational Methods in Applied Mechanics and Engineering*, 191:1471–1489, 2002.
- [83] C.S. Edwards, H.A. Kim, and C.J. Budd. An evaluative study of ESO and SIMP for optimising a cantilever tie-beam. *Structural and Multidisciplinary Optimization*, 34:403–414, 2007.
- [84] D.P. Bertsekas. *Constrained Optimization and Lagrange Multipliers Method*. Academic Press, first edition, 1982.
- [85] R. Horst, P.M. Pardalos, and N.V. Thoai. *Introduction to Global Optimization*. Kluwer Academic Publishers, second edition, 2000.

- [86] M.S. Bazaraa, H.D. Sherali, and C.M. Shetty. *Nonlinear Programming: Theory and Algorithms*. John Wiley and Sons, Inc., third edition, 2006.
- [87] N.M. Alexandrov and R.M. Lewis. Analytical and computational aspects of collaborative optimization. Technical Report NASA TM-2000-210104, Langley Research Center, Hampton, VA, April 2000.
- [88] The Mathworks, Inc. *fmincon, MATLAB documentation manual, Version 7.9.0.529 (R2009b)*.
- [89] P.T. Boggs and J.W. Tolle. Sequential quadratic programming. *Acta Numerica*, 4:1–51, 1995.
- [90] A. Saxena and G.K. Ananthasuresh. On an optimal property of compliant topologies. *Structural and Multidisciplinary Optimization*, 19:36–49, 2000.
- [91] J. Petersson and O. Sigmund. Slope constrained topology optimization. *International Journal for Numerical Methods in Engineering*, 41:1417–1434, 1998.
- [92] M. Werme. Using the sequential linear programming method as a post-processor for stress-constrained topology optimization problems. *International Journal for Numerical Methods in Engineering*, 76:1544–1567, 2008.
- [93] K. Qiu, W. Zhang, M. Domaszewski, and D. Chamoret. Topology optimization of periodic cellular solids based on a superelement method. *Engineering Optimization*, 41(3):225–239, 2009.
- [94] S. Li. General unit cells for micromechanical analyses of unidirectional composites. *Composites: Part A*, 32:815–826, 2000.
- [95] L.J. Gibson, F.R.S. Ashby M. F., G.S. Schajer, and C.I. Robertson. The mechanics of two-dimensional cellular materials. *Proceedings of the Royal Society of London A*, 382:25–45, 1982.
- [96] L.J. Gibson and M.F. Ashby. *Cellular solids: structures and properties*. Cambridge University Press, second edition, 1997.
- [97] I.G. Masters and K.E. Evans. Models for the elastic deformation of honeycombs. *Composite Structures*, 35:403–422, 1996.
- [98] S. Balawi and J.L. Abot. A refined model for the effective in-plane elastic moduli of hexagonal honeycombs. *Composite Structures*, 84:147–158, 2008.
- [99] A. Bezazi, Scarpa F., and C. Remillat. A novel centric symmetric honeycomb composite structure. *Composite Structures*, 71:536–564, 2005.
- [100] S. Gonella and M. Ruzzene. Homogenization and equivalent in-plane properties of two-dimensional periodic lattices. *International Journal of Solids and Structures*, 45:2897–2915, 2008.

- [101] J. Ju, B. Ananthasayanam, J.D. Summers, and P. Josesph. Design of cellular shear bands of a non-pneumatic tire—investigation of contact pressure. *SAE International*, 3:598–606, 2010.
- [102] Z. Hashin and S. Shtrikman. A variational approach to the theory of the elastic behaviour of multiphase materials. *Journal of the Mechanics and Physics of Solids*, 11:127–140, 1963.